EPFL

Real space and reciprocal space investigations of the spin dynamics in skyrmion-hosting materials

Le YU

Acknowledgements

Lausanne, 14th October 2022.

Abstract (English)

Magnetic skyrmions are whirl-like spin configurations with particle-like properties protected by non-trivial topology. Due to their unique spin structures and dynamical properties, they have attracted tremendous interests over the past decade, from fundamental science to technical applications. However, experimental methods to study skyrmion dynamics in real space are limited until present. The goal of this thesis is to both apply and develop novel methodologies to firstly discover new skyrmion lattice hosting systems through neutron scattering experiments, and then directly observe the dynamics in these materials in real space by time-resolved imaging. The main content of this thesis is divided into two parts: firstly, I will demonstrate by means of inelastic neutron scattering how the magnon spectrum was measured in $VOSe_2O_5$, one of the few known systems hosting Néel-type skyrmion lattice. By comparing the measured spectrum with SpinW simulations, the exchange interactions and magnetic anisotropy were extracted so that the spin Hamiltonian in this system could be constructed. The results provide positive feedback to the recently developed quantum chemistry calculations. Further, the reasonable consistency among experiments, simulations and calculations may enable the community to use quantum chemistry as a novel tool to predict new skyrmion hosting materials and understand their formation.

The second part of this thesis will introduce my work in integrating a microwave system into a time-resolved transmission electron microscope (TEM). In this project, a pump-probe technique using microwave to coherently excite spin wave dynamics in skyrmion lattice hosting materials in the GHz frequency range was developed and implemented. The time-resolved TEM will enable the direct observation of excited spin waves and skyrmion dynamics in real space. This instrumental development will also allow the study of the spatial homogeneity of resonant modes, and their behavior around individual impurities or grain boundaries. The insights gained from these experiments will help the community to understand microscopic aspects of skyrmion dynamics and tailor spintronic devices using skyrmions in the future.

The chapter layout will be presented as follows: in Chapter One, I will introduce fundamental concepts about skyrmions, and then discuss their general magnon spectrum and how they can be measured. Chapter Two will describe methodologies adopted during this thesis work, including experimental techniques and modelling methods. The scattering experiment details and results obtained at various beamlines will be presented in Chapter Three. The progress concerning the development of the new technique in time-resolved real space imaging starts from Chapter Four. Here, the implementation of a microwave system in ultrafast TEM will be demonstrated systematically. The last chapter contains the conclusion and outlook.

Keywords: skyrmion lattice, magnon spectrum, inelastic neutron scattering, quantum chemistry calculation, SpinW simulation, ultrafast transmission electron microscopy, pump-probe, microwave.

Résumé (Français)

Les skyrmions magnétiques sont des configurations de spins tourbillonnant ayant des propriétés topologiquement non trivial. Dû à leur structure et propriété de dynamique uniques, ils ont attiré un grand intérêt lors de ces dernières décennies, autant dans les sciences fondamentales que dans les applications technologiques. Néanmoins, à ce jour, le nombre de méthodes expérimentales pour étudier la dynamique des skyrmions dans l'espace réel reste limité. Le but de cette thèse est double : appliquer et développer de nouvelles méthodologies pour découvrir de nouveaux matériaux possédant un réseau de skyrmions via des expériences de diffusion de neutrons, pour dans un second temps observer leur dynamique dans l'espace réel par imagerie en temps résolu. Le contenu de cette thèse est divisé en deux sections : premièrement, je vais démontrer comment le spectre magnonique a été mesuré dans $VOSe_2O_5$ un des rares composés connus possédant un réseau de skyrmion de type Néel, à partir de la technique utilisant la diffusion de neutrons inélastiques. En comparant, le spectre mesuré à celui simulé par SpinW, les valeurs des interactions d'échanges et des anisotropies magnétiques en sont extraites de manière à construire l'Hamiltonien de spins de ce système. Les résultats apportent un feedback positif sur les calculs de chimie quantique développé récemment. La consistance raisonnable trouvé entre l'expérience, les simulations et les calculs va permettre à la communauté d'utiliser la chimie quantique comme nouvel outil pour prédire de nouveaux matériaux-hôtes et de comprendre leur formation.

La deuxième partie de cette thèse présentera mon travail sur l'intégration d'un système micro-onde dans un microscope électronique à transmission (MET) à résolution temporelle. Dans ce projet une technique pompe-sonde utilisant les micro-ondes dans la gamme des GHz pour exciter de manière cohérente des ondes de spin dans un matériau possédant une phase skyrmionique a été développée et implémentée. Le MET à résolution temporelle permettra l'observation directe d'ondes de spins excitées et de la dynamique des skyrmions dans l'espace réel. De plus, cette avancée majeure permettra d'étudier l'homogénéité spatial des modes résonnants et leurs comportements autour d'impuretés ou de limites de grains. Les renseignements obtenus de ces expériences pourront aider la communauté à mieux comprendre les aspects microscopiques de la dynamique des skyrmions et par conséquent adapter les appareils spintroniques utilisant des skyrmions dans le futur.

La disposition des chapitres se présente comme suit : dans le premier chapitre, je vais introduire les concepts fondamentaux à propos des skyrmions et ensuite discuter leur spectre magnonique générale et comment il peut être mesurer. Le chapitre deux décrira les méthodologies adoptées pendant ce travail de thèse, incluant les techniques expérimentales ainsi que les méthodes de modélisation. Les résultats des expériences de diffusions obtenus à différentes lignes de faisceaux seront présentés au chapitre trois. Les progrès concernant le développement de la nouvelle technique de l'imagerie dans l'espace réel en temps résolu commenceront à partir du chapitre quatre. Ici, l'implémentation du système micro-onde dans un MET ultrarapide sera décrit méthodiquement. Le dernier chapitre contiendra la conclusion et les perspectives.

Mot clefs : réseau de skyrmion, spectre magnonique, diffusion de neutrons inélastiques, calculs de chimie quantique, simulation SpinW, microscopie électronique à transmission ultrarapide, pompe-sonde, micro-onde.

List of Figures

List of Tables

List of content

Chapter One: Introduction

1.1 Fundamental properties of magnetic skyrmions

Skyrmion is named after T. H. R. Skyrme who firstly introduced this term in 1962 to describe the stability of mesons and baryons in particle physics [1]. It represents a stable field configuration with particle-like properties, and it is a topological soliton solution to the non-linear Sigma model [1]. After this term was coined, its analog has been applied extensively in condensed matter physics, when field configurations with similar topological properties are discovered, for example a unique type of excitation in quantum Hall systems [2]. In the definition of a magnetic skyrmion (hereafter referred as skyrmion), the field configuration is represented by magnetic spin configurations shown in Fig. 1.1 (a). There are two types of topologically equivalent magnetic skyrmions: Bloch-type and Néel-type.

Depending on the material, skyrmion sizes range from 10 nm to a few µm (large skyrmions are also called magnetic bubbles [3]). They can exist individually or condense into a lattice. Individual skyrmions are usually found in synthesized thin-film materials, and they generate unique transport properties such as the topological Hall effect [4]. Further, the electric current density needed to drive skyrmions is only a few micro-ampere per square meter, which is three orders of magnitude smaller than driving conventional domain walls in ferromagnetic materials [5]. For these reasons, individual skyrmions are widely considered to be promising candidates for next-generation spintronic devices offering data storage with ultra-low loss. Skyrmions in lattice form can exist in crystals when the crystal structure has broken inversion symmetry, forming either Bloch-type or Néel-type skyrmion lattice. Such a lattice is an intrinsic magnonic crystal which provides a platform to investigate spin wave generation and propagation properties. The frequencies of magnon excitations in skyrmion lattice fall into the GHz range [6]. This allows for the integration of spin wave devices into modern telecommunication technology [7].
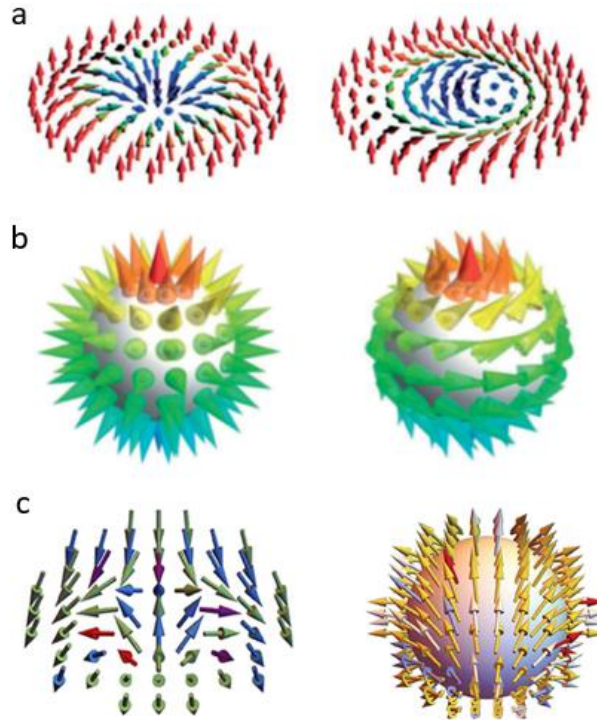
Fig. 1.1: (a) Spin configurations of Néel-type (left) and Bloch-type (right) skyrmions. Image reproduced from Ref. [8]; (b) the spin configurations of skyrmions mapped onto a unit sphere by stereographic projection, where the sphere is wrapped once – winding number 1. Image reproduced from Ref. [9]; (c) spin configuration and projection on a unit sphere of an anti-skyrmion. Image reproduced from Ref. [10].

The topological properties of skyrmions are characterized by a topological charge:

$$Q = \frac{1}{4\pi} \int \boldsymbol{n} \cdot (\frac{\partial \boldsymbol{n}}{\partial x} \times \frac{\partial \boldsymbol{n}}{\partial y}) dx dy \qquad (1.1)$$

where (x, y) is the spin coordinate in the plane perpendicular to the external magnetic field usually needed to stabilize skyrmions, and $\boldsymbol{n}$(x, y) is the unit magnetization vector. The topological charge can be viewed as how many times the spins wrap a 3D unit sphere – called winding number or topological order, as illustrated in Fig. 1.1 (b). The spin at the center of a skyrmion is projected to the north pole, and all spins at the periphery are projected to the south pole. The 3D unit sphere coordinate (X, Y, Z) is connected to the 2D plane (x, y) by stereographic projection:

$$(x, \; y) \rightarrow (\frac{X}{1-Z}, \; \frac{Y}{1-Z}) \qquad . \qquad (1.2)$$

Skyrmions are also described by helicity and polarity. Helicity is defined as the angle of global spin rotation around the z-axis. It is equal to zero for Néel-type skyrmions and ±1 for Bloch-type skyrmions. Polarity p is determined by the spin orientation at the skyrmion core: p = +1 when it points along the positive z-axis direction and p = -1 when it points along the negative z-axis direction. For both Bloch-type and Néel-type skyrmions, the polarity and topological charge are equal Q = p.

Anti-skyrmions have opposite topological charge and polarity Q = -p. The topological charge is equal to +1 for skyrmions and -1 for anti-skyrmions for the same polarity. The spin configuration of an anti-skyrmion and its projection onto a unit sphere are schematically shown in Fig. 1.1 (c). Anti-skyrmions are found in Heusler compounds with even lower symmetry [11] as well as in ultrathin magnetic films.

By "topological", one means that a skyrmion cannot be generated, annihilated or transformed to a different topological order by continuously varying the spin configuration, because there is a finite energy barrier that needs to be overcome to change the topology. Mathematically speaking, an operation represented by a continuous function applied on a skyrmion preserves the topological order. Thus, magnetic skyrmions are rather stable objects thanks to this topological protection.
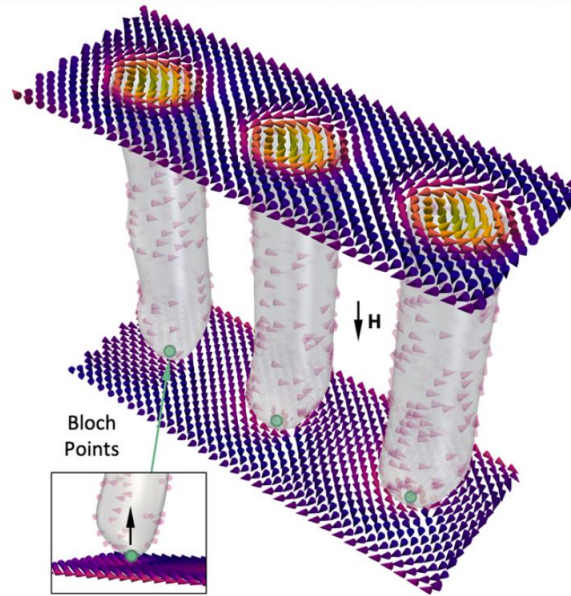
Fig. 1.2: A 3D visualization of three parallel skyrmion tubes produced by micromagnetic simulations. The inset displays the magnetic Bloch point at the end of each tube. Image reproduced from Ref. [12].

Despite the fact that skyrmions are usually presented as a 2D object existing on a plane, in reality they extend through the thickness of the material as an elongated tube-like structure. The 3D structure of skyrmions is demonstrated by magnetic x-ray holography and microscopy techniques in 2020 using a 120 nm thin FeGe lamella [12]. A schematic visualization is shown in Fig. 1.2. Furthermore, skyrmions are found to unwind by the motion of magnetic singularities, called Bloch-points, existing at the end of each skyrmion tube. This is crucial for understanding processes governing the writing and erasing skyrmions in spintronic applications.

The topological charge of a skyrmion can couple to external stimuli, allowing them to be manipulated by an external electric current [5]. The non-trivial topological spin texture generates an emergent magnetic field $\boldsymbol{B}^i_{eff}$ which can deflect the electrons traveling through a skyrmion [13]:

$$\boldsymbol{B}^i_{eff} = \frac{\phi_0}{8\pi} \epsilon_{ijk} \boldsymbol{n} \cdot (\partial_j \mathbf{n} \times \partial_k \mathbf{n}) \tag{1.3}$$

where ϕ_0 is the flux quantum, ϵ_{ijk} is the Levi-Civita symbol. Equation (1.3) implies the strength of this effective magnetic field depends on skyrmion density. In a different picture, a magnetic vector potential is produced because electrons gain Berry phase in the skyrmion texture, illustrated in Fig. 1.3 (a). The emergent magnetic field leads to an additional component in the Hall effect [4]:

$$\rho_{yx} = \rho^N_{yx} + \rho^A_{yx} + \rho^T_{yx} \tag{1.4}$$

$$\rho^T_{yx} = \mathrm{P} R_{H_0} \boldsymbol{B}^z_{eff} \tag{1.5}$$

where ρ^N_{yx} and ρ^A_{yx} in Equation (1.4) represent the contributions from the conventional Hall effect and anomalous Hall effect, respectively. The third term is the topological Hall resistance expressed in Equation (1.5), which is proportional to the effective magnetic field $\boldsymbol{B}^z_{eff}$. Also, P is a factor proportional to the spin polarization of charge carriers, and R_{H0} is the Hall coefficient.

A further consequence of the emergent magnetic field is spin-transfer torque [14]. It originates from the extra spin current resulting from electric current when electrons travel through the skyrmion spin texture. The spin polarization on opposite sides of a skyrmion produces a net torque. It leads to unique transport properties and thus a wide range of potential applications which are under active research. The effects due to the emergent magnetic field in a skyrmion are schematically illustrated in Fig. 1.3 (b).

(a)   **(b)**
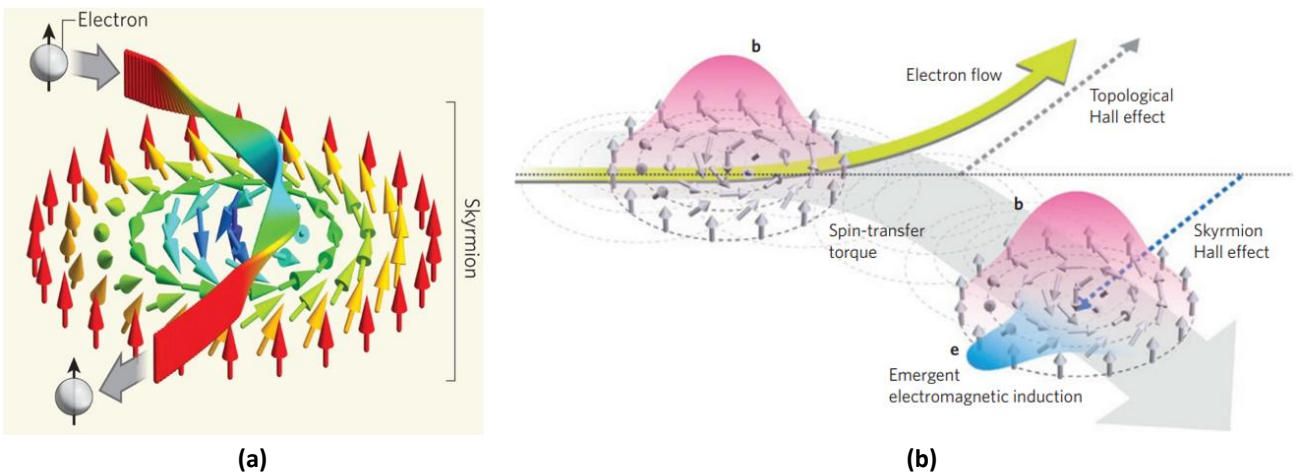
*Fig. 1.3: (a) Electron traveling through a skyrmion, undergoing the Berry phase variation. Image reproduced from Ref. [15]; (b) schematic illustration of spin transfer torque. The emergent magnetic field and electric field are labelled as "**b**" and "**e**", respectively. The skyrmion is deflected in the opposite direction, called skyrmion Hall effect. Image reproduced from Ref. [16].*

1.2 Magnetic interactions and symmetry aspects

Until today, several mechanisms to stabilize skyrmions have been proposed [16], while the most common one has the competition between the symmetric exchange interaction and the anti-symmetric Dzyaloshinskii -Moriya interaction (DMI) [17-18] as the key ingredient. Exchange interaction, also known as Heisenberg interaction, favors parallel alignment between neighboring spins, and it has the form:

$$H_{exchange} = J_{12}(\boldsymbol{S_1} \cdot \boldsymbol{S_2}) \tag{1.6}$$

where the scalar factor J_{12} represents the magnitude of the exchange interaction. The DMI however, favors perpendicular alignment between neighboring spins. It is characterized by a vector and the form varies from Néel-type to Bloch-type skyrmions:

$$H_{DMI} = \boldsymbol{D_{12}} \cdot (\boldsymbol{S_1} \times \boldsymbol{S_2}) \tag{1.7}$$

$$\boldsymbol{D_{12-Bloch}} = D_{12}\boldsymbol{S_{12}} \quad ; \quad \boldsymbol{D_{12-Néel}} = D_{12}\boldsymbol{S_{12}} \times \boldsymbol{k_c} \tag{1.8}$$

where $\boldsymbol{D_{12}}$ is the DMI vector, $\boldsymbol{S_{12}}$ is a vector connecting the atomic positions of two neighboring spins, and $\boldsymbol{k_c}$ is a unit vector in the plane spanned by $\boldsymbol{S_1}$ and $\boldsymbol{S_2}$. According to the definition in Equation (1.8), the DMI vector points from one spin to its neighboring spin in Bloch-type skyrmions, and points perpendicularly to the plane spanned by $\boldsymbol{S_1}$ and $\boldsymbol{S_2}$ in Néel-type skyrmions. The different orientations of the DMI vector are defined by the underlying crystal structure. They lead to different ways of canting between neighboring spins and result in different internal magnetization structures of the two types of skyrmions introduced in Fig. 1.1. A graphic explanation of DMI and spin canting can be found in the bottom panel of Fig. 1.4.

In the continuum limit where the magnetization vector varies smoothly on the length scale of a unit cell, averaged exchange interaction (*J*) and DMI (*D*) over the unit cell are usually taken. This is also known as micromagnetic limit, and the details are described in section 2.4.2. In this case, the periodicity of the pattern found in the spin configuration of skyrmion lattice (pitch length) can be roughly estimated by the ratio between exchange interaction and the magnitude of DMI vector [16]:

$$\lambda = \frac{J}{D} \ . \tag{1.9}$$

The pitch length is also commonly adopted to define the skyrmion size, because skyrmions are closely packed in a lattice. It is worth noting that both exchange interaction and DMI have the same origin: they result from the repulsive Coulomb interaction between neighboring magnetic atoms, in addition to Pauli exclusion principle. Exchange interaction accounts for the symmetric distribution of electron orbitals, and DMI accounts for the anti-symmetric distribution, which is usually a consequence of spin-orbit interaction [19]. There are further types of magnetic interactions which play a role in the stabilization of skyrmions, such as magnetic anisotropic energy, dipolar interaction and Zeeman interaction.

While the symmetric exchange interaction is universal in magnetic materials, the anti-symmetric DMI can only exist when certain symmetry conditions in the crystal lattice are met [17-18]. For skyrmions, DMI emerges when the underlying crystal structure has no inversion center, that is, it has a non-centrosymmetric point group. In crystallography, a centrosymmetric point group can map every point (*x, y, z*) in space to an indistinguishable point (*-x, -y, -z*). Point groups lacking an inversion center include chiral and polar structures [20], leading to the two different DMI textures and the formation of Bloch-type and Néel-type skyrmions, respectively. The crystal structures of each example hosting material are provided in Fig. 1.4: (a) chiral magnet Cu_2OSeO_3 has rotation symmetries but no mirror symmetry; (b) polar magnet $VOSe_2O_5$ has no inversion symmetry perpendicular to the a-b plane, while it has rotation and mirror symmetry around the c-

axis (also called the polar axis). Polar crystal structures hosting Néel-type skyrmion lattice are scarce so they are less explored compared with chiral magnets. The broken inversion symmetry can also be realized by fabrication, for example, in ferromagnet-heavy metal multi-layer systems. The strong spin-orbit coupling at their interface induces DMI and leads to the formation of individual Néel-type skyrmions as a metastable state [21].

$$D_{ij} = \mathrm{D}S_{ij}$$

$$S_i \uparrow \quad \xrightarrow{D_{ii}} \quad \odot S_j$$

$$D_{ij} = \mathrm{D}k_c \times S_{ij}$$

$$S_i \uparrow \quad \odot D_{ij} \quad \longrightarrow S_j$$

(a) (b)
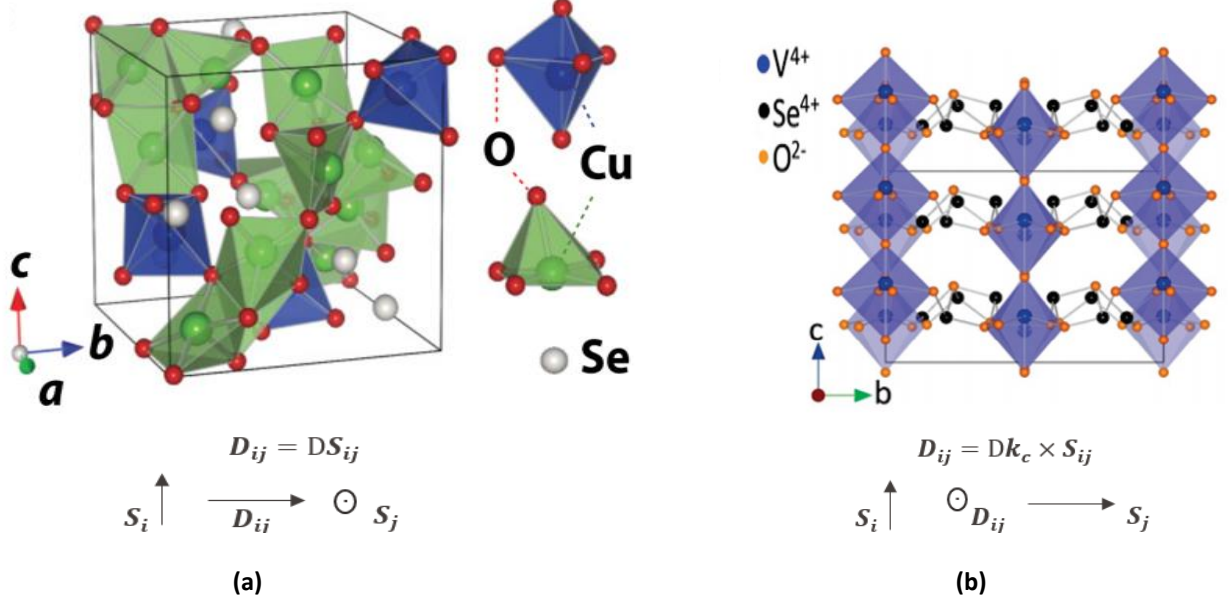
Fig. 1.4: The crystal lattice structure of (a) chiral magnet Cu_2OSeO_3 [22] and (b) polar magnet $VOSe_2O_5$ [23], hosting Bloch-type and Néel-type skyrmion lattice, respectively. The bottom panel illustrates the orientations of DMI vectors and canted neighboring spins.

Despite distinct symmetry aspects in Bloch-type and Néel-type skyrmions and their hosting materials, their magnetic phase diagrams share various common features. As shown in Fig. 1.5, at zero magnetic field below the Curie temperature, the magnetic ground state is a multi-domain spiral state: a helical state (denoted as multi-q) in chiral magnets and a cycloidal state (denoted as IC-1) in polar magnets. The relevant skyrmion phase exists in a small pocket at finite magnetic field slightly below the Curie temperature. The thermal fluctuations are argued to play an important role in stabilizing skyrmions in chiral magnets [24]. These features in the phase diagram of chiral magnets have been theoretically proven to be universal in all bulk materials hosting Bloch-type skyrmions in lattice form [25].

Next to the skyrmion phase at finite magnetic field, the magnetic phase is a single-q conical state in chiral magnets, where the propagation vector is aligned with the external magnetic field. The rest of the phase diagram is more complicated for polar magnets: in $VOSe_2O_5$ it is an incommensurate state with double propagation vectors (denoted as IC-2) next to the Néel-type skyrmion phase. In the original paper [26], this phase was proposed to be a square skyrmion lattice state. However, later neutron scattering studies suggested it to be a topologically trivial double-q state [27]. Below 4 K, the ground state was presumed to be an easy-plane ferrimagnetic state (denoted as FM) in the a-b plane with 3-up 1-down configuration [26]. However, neutron diffraction experiments performed as part of this thesis work, in addition to theoretical calculations, suggest this phase should have the 3-up 1-down configuration along the c-axis. Between the FM ground state and the IC-1 phase, there is a so-called B phase, the nature of which remains unknown.
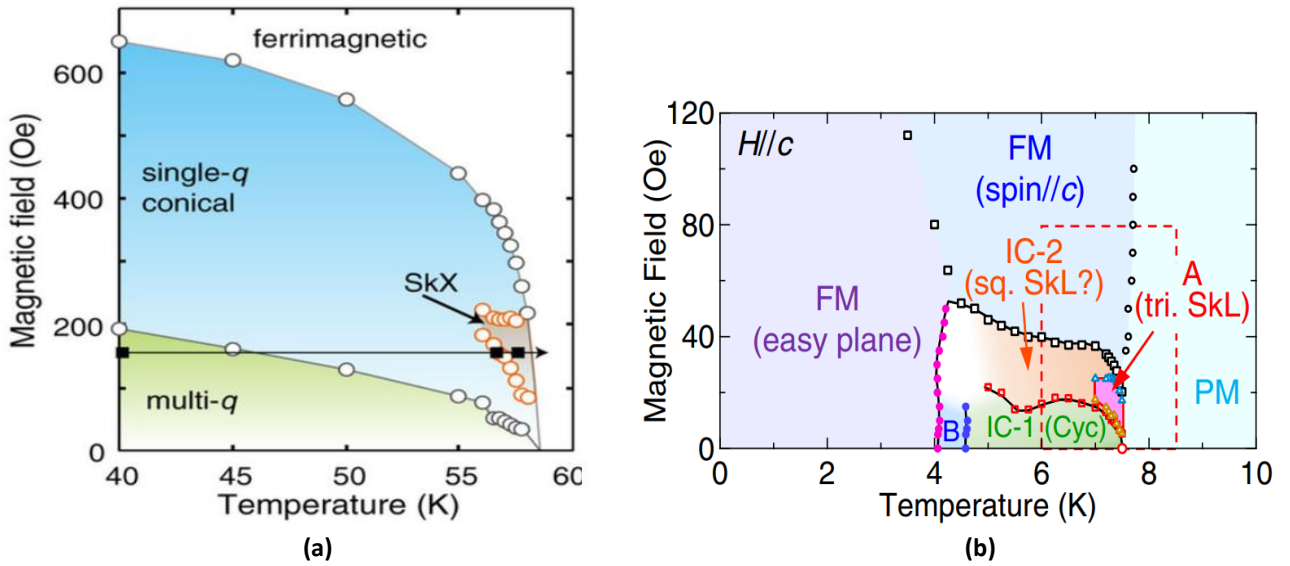
Fig. 1.5: The magnetic phase diagrams of (a) chiral magnet Cu$_2$OSeO$_3$ [28] and (b) polar magnet VOSe$_2$O$_5$ [26], hosting Bloch-type and Néel-type skyrmion lattice, respectively.

1.3 Skyrmion hosting materials and techniques to study skyrmions

The first experimental discovery of skyrmion lattice in bulk magnets was achieved in 2009. By using small-angle neutron scattering (SANS), a diffraction pattern with six-fold symmetry was observed, which is characteristic for a hexagonal close-packed skyrmion lattice [29]. The material used in this experiment was bulk MnSi, a $B20$ compound with chiral cubic space group $P2_13$. One such pattern is shown in Fig. 1.6 (a), measured at temperature 26.77 K and an external magnetic field 16.4 mT [29]. Soon after, skyrmion lattice was observed in real space by Lorentz Transmission Electron Microscope (LTEM) in another $B20$ compound Fe$_{0.5}$Co$_{0.5}$Si [30]. Fig. 1.6 (b) presents one image measured at 25 K and an external magnetic field 50 mT perpendicular to the thin TEM sample. The data are processed by Transport of Intensities Equation analysis, by which in-plane spin components are encoded in white arrows and a color wheel. In 2012, skyrmion lattice was found in the oxide Cu$_2$OSeO$_3$, also with space group $P2_13$, expanding the family of hosting materials to insulators. Recently, another group of Bloch-type skyrmion lattice hosting materials called β-Mn-type Co-Zn-Mn alloys attracted enormous interests [31]. It has a different chiral cubic space group $P4_132$, and can host skyrmion lattice at or even above room temperature. This group of systems contains numerous members depending on the relative weight between Co, Mn and Zn atoms, hence it provides a novel, chemically tunable platform to study fundamental aspects of skyrmion lattice.
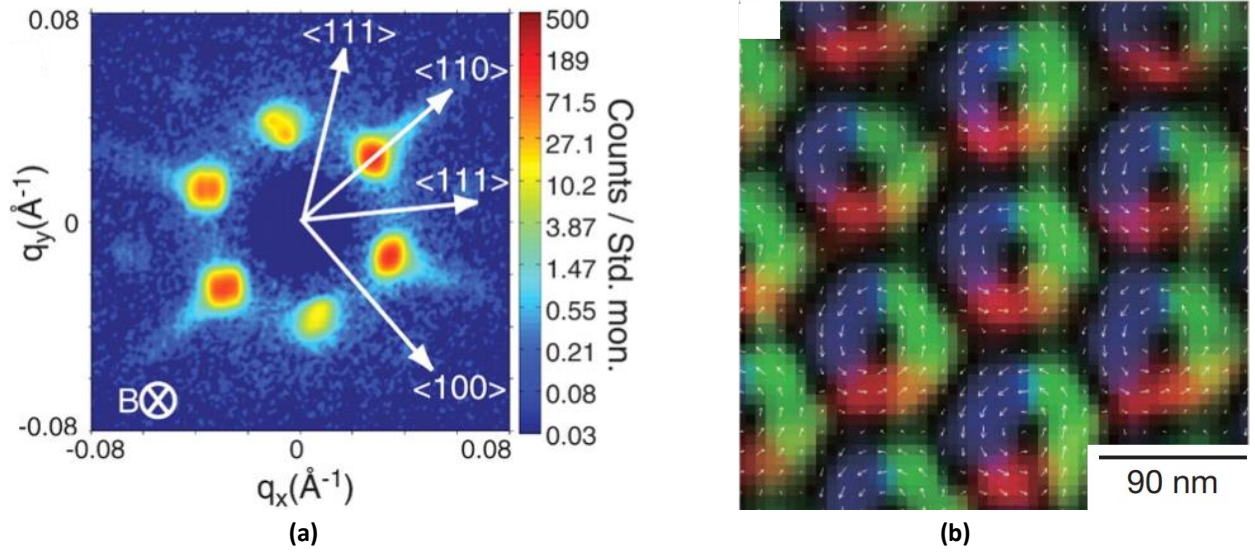
Fig. 1.6: (a) SANS pattern of the skyrmion lattice in MnSi (26.77 K, 16.4 mT) [29]; (b) LTEM image of the skyrmion lattice in $Fe_{0.5}Co_{0.5}Si$ (25 K, 50 mT) [30].

In contrast to various chiral magnets found to host Bloch-type skyrmion lattice, the bulk materials known to host Néel-type skyrmions in lattice form are much rarer. One of them is the semiconductor GaV_4S_8. The real space image obtained by Magnetic Force Microscope (MFM) is shown in Fig. 1.7 (a), where the temperature was 11.6 K with an external magnetic field 50 mT [8]. The insulating tetragonal polar magnet $VOSe_2O_5$ was found to host Néel-type skyrmion lattice in 2017 by SANS [26]. One of SANS patterns is reproduced in Fig. 1.7 (b) measured at 7.45 K and an external magnetic field 25 Oe applied along the polar-axis of this compound. Here, the 12-fold symmetry pattern implies the coexistence of two hexagonal skyrmion lattice domains. Compared with Bloch-type skyrmions and hosting systems, the Néel-type counterpart is less-studied due to the lack of known materials. There remain many open questions in the phase diagram and spin Hamiltonian which motivated the scattering project in this thesis. For example, the magnetic interactions present in the hosting systems and their magnitude; the competition among these magnetic interactions. Chapter Three will address these fundamental questions through neutron scattering experiments, theoretical calculations and simulations.
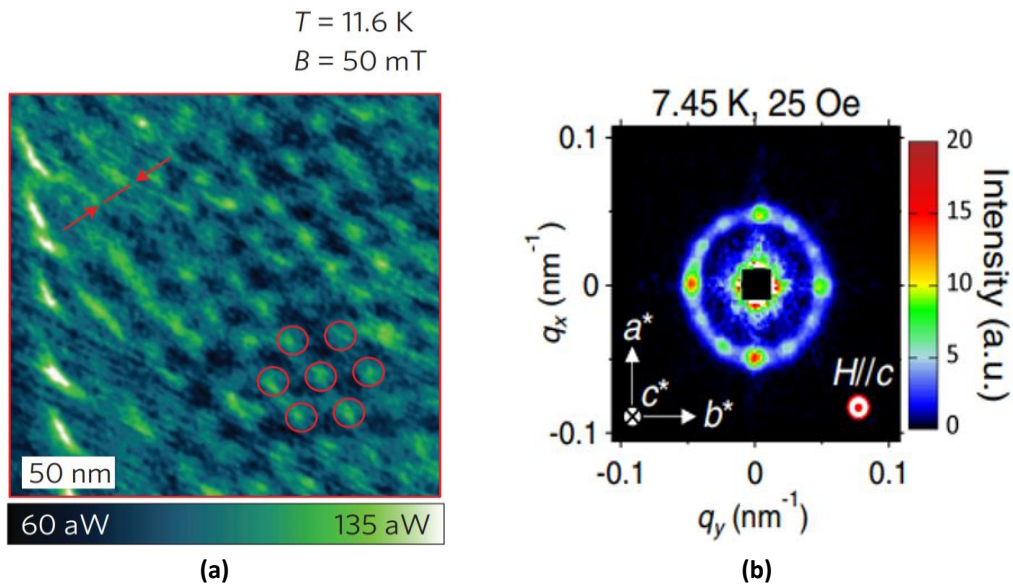
Fig. 1.7: (a) MFM image of the skyrmion lattice in GaV_4S_8 [8]; (b) SANS pattern of $VOSe_2O_5$ in the skyrmion phase [26]. The temperature and magnetic field are indicated.

1.4 Skyrmion excitation and magnon spectrum

In recent years, the research community has shifted its attention towards a deeper understanding in the dynamics of skyrmions. Understanding the dynamical properties of skyrmions themselves and their hosting materials is not only significant fundamentally, but also useful in practical applications. The second half of this thesis work focuses on the resonant collective excitations, also called spin wave modes, in the lattice form of skyrmions. The research on spin wave excitations in skyrmions was pioneered by M. Mochizuki in 2012 [32], who numerically calculated the spin dynamics in response to an external AC magnetic field and evaluated the microwave absorption spectrum (imaginary part of the dynamical susceptibility). Three magnon modes were predicted: clockwise and anti-clockwise modes driven by an in-plane AC magnetic field, where out-of-plane spin components circulate around skyrmion cores; and a breathing mode driven by an out-of-plane AC magnetic field, where skyrmion cores expand and contract periodically. The numerical simulations that demonstrate the temporal evolution of these three modes are shown in Fig. 1.8 [32].

Soon after this work, various experiments were performed to search for these modes. Also in 2012, Y. Onose et al. firstly detected them by broadband microwave transmission spectroscopy using a vector network analyzer. The sample was Cu_2OSeO_3 mounted on a microstrip line [33]. The resonant frequencies of these three modes were reported to be between 1 GHz and 2 GHz, depending on the external magnetic field within the skyrmion phase. A similar experiment run by Y. Okamura et al. also found these modes in Cu_2OSeO_3, while this experiment employed a coplanar waveguide (CPW) setup. In addition, a non-reciprocal directional dichroism phenomenon was reported, that is, oppositely propagating microwaves exhibit different absorptions, determined by the relative orientation among the microwave propagation, electric polarization and magnetization in Cu_2OSeO_3 which has a strong magneto-electric coupling [34].
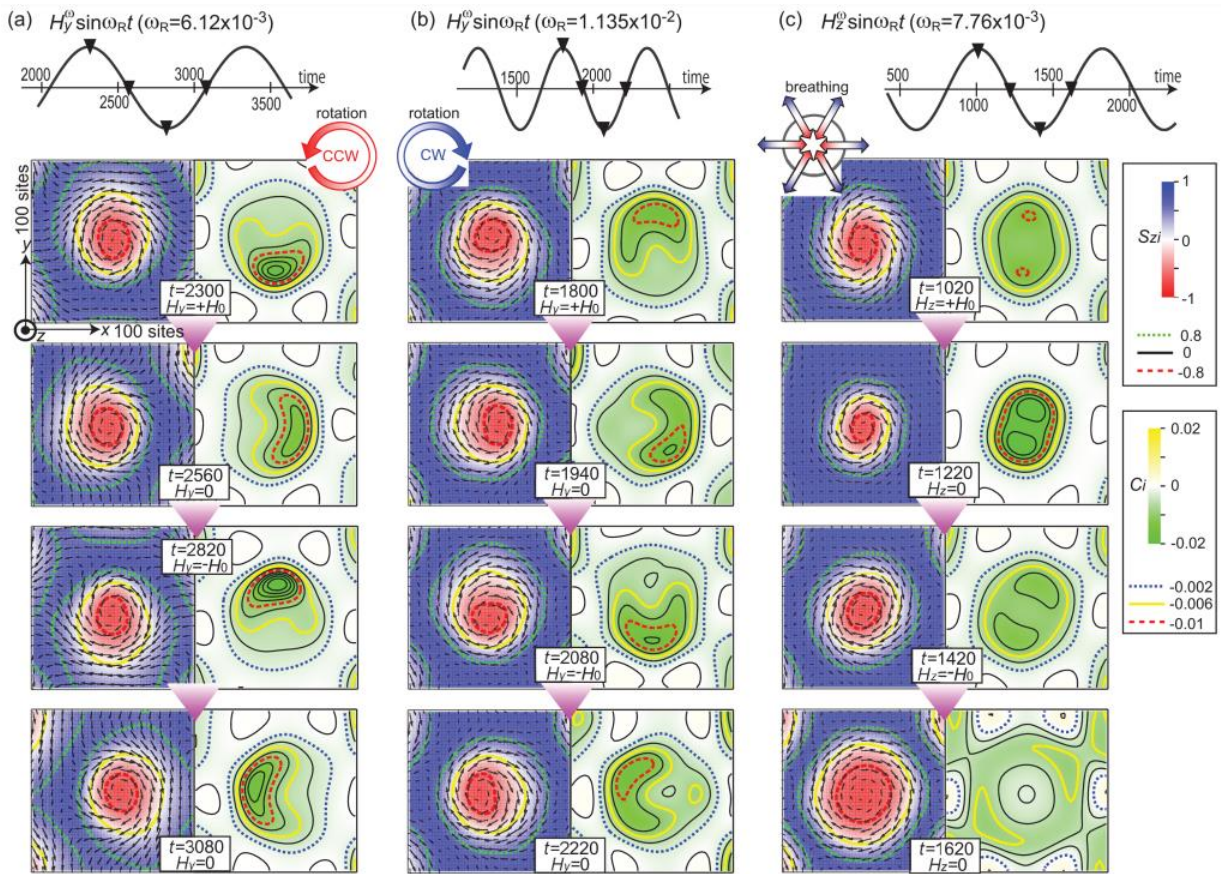
Fig. 1.8: Demonstrations of skyrmion temporal evolution in (a) counter-clockwise mode; (b) clockwise mode; (c) breathing mode. Image reproduced from Ref. [28].

In 2015 T. Schwarze et al. used a CPW setup and demonstrated a universal behavior of spin wave modes in metallic (MnSi), semiconducting ($Fe_{1-x}Co_xSi$) and insulating (Cu_2OSeO_3) chiral magnets in the skyrmion phase [35]. The CPW setup allows the generation of sinusoidal AC magnetic field either in-plane or out-of-plane depending on the position of the sample relative to the signal line (S) and the ground line (G), as shown in Fig. 1.9. The three modes have identical energy hierarchy, however the resonant frequencies vary from 1 GHz up to 20 GHz from one material to another. The methodologies, especially the CPW setup used in these experiments inspired the idea for the technical development of this thesis described in Chapter Four.
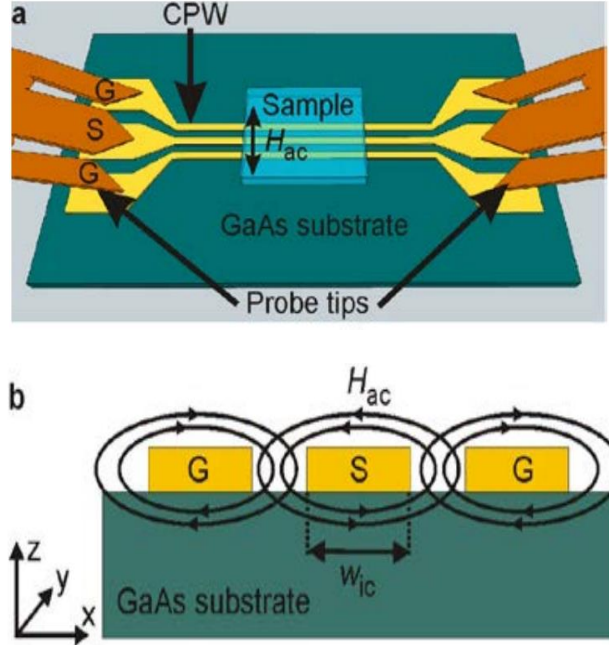
Fig. 1.9: (a) Broadband microwave transmission spectroscopy setup, where the Cu_2OSeO_3 sample is placed on a CPW; (b) magnetic field distribution near signal line (S) and ground lines (G) on the CPW. Images reproduced from Ref. [35].

The spin wave modes of the skyrmion lattice in Cu_2OSeO_3 were detected in 2015 by an optical pump-probe experiment [28]. Fig. 1.10 shows the principle of the experiment which exploits the inverse Faraday Effect, where an ultrafast circularly polarized laser pulse generates an effective magnetic field pulse, and this transient field can be as strong as 5 T [36]. In the experiment, this pulse acted as an impulsive pump which triggered spin-precessional motions. After the pump pulse, a linearly polarized probe light detected the change in the time-dependent out-of-plane magnetization through Faraday rotation. By shifting the time delay and observing beating features in the Faraday rotation of the probe light [Fig. 1.10 (b)], spin wave modes were identified. Recently, an optical pump-probe experiment in LTEM implied that the pulsed excitation of the breathing mode can induce a skyrmion lattice rotation [37].
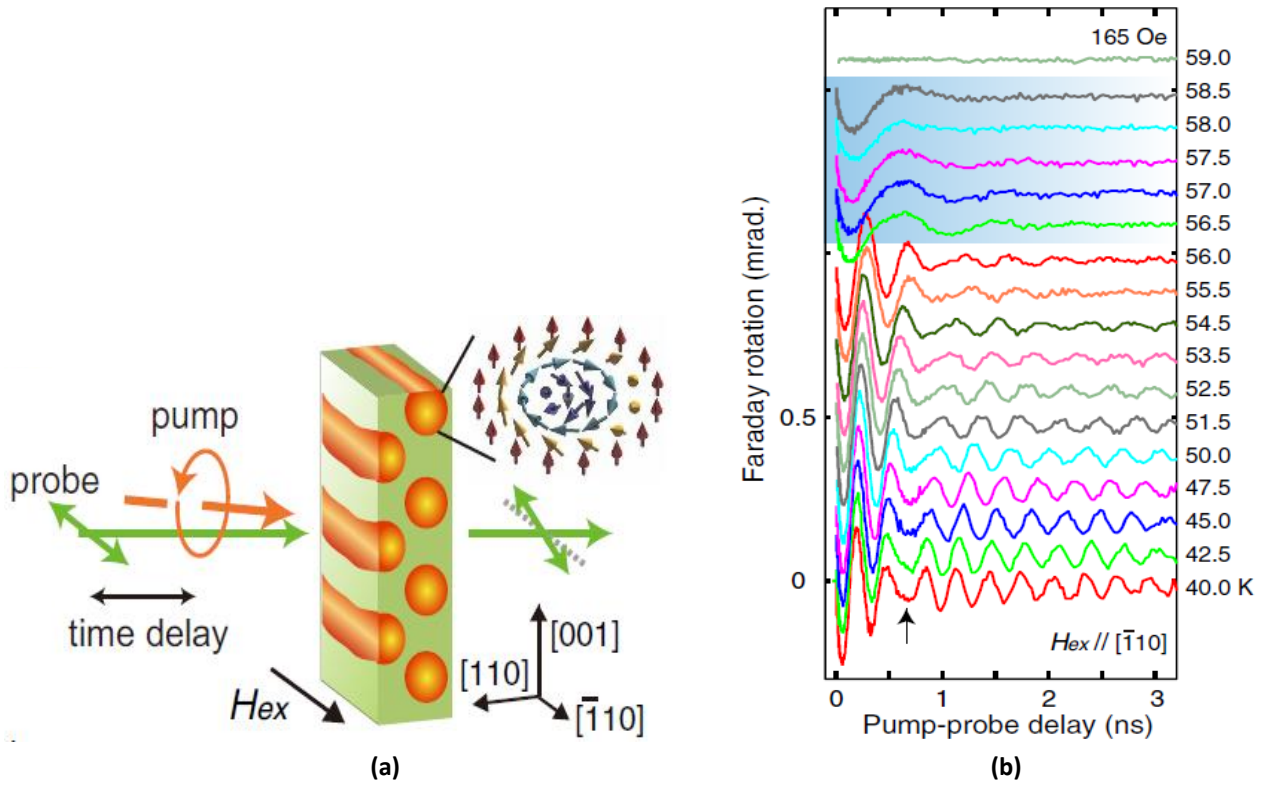
Fig. 1.10: (a) Schematics of optical pump-probe experiment performed on Cu$_2$OSeO$_3$; (b) beating features in the Faraday rotation angle as a function of time delay at various temperatures. The blue region indicates the temperature range of the skyrmion phase. Image reproduced from Ref. [28].

The resonant spin wave modes of the skyrmion lattice have never been directly observed in real space, leaving a number of interesting questions regarding spin wave propagation to be explored. The development of a microwave pump-probe technique in LTEM enables us to precisely trigger certain modes with reduced parasitic modes. Combined with time-resolved imaging, we are allowed to observe long-range behaviors of collective modes and their properties around disorders or impurities, which can only be observed in real space. The realization of these experiments will further deepen our understanding in dynamical properties of skyrmion lattice, and help the community to develop tailored skyrmion-based spintronic devices.

To summarize, the goal of this thesis is to apply and develop novel techniques to study the magnetic dynamics in skyrmion lattice hosting materials, in both real space and reciprocal space, and to address various fundamental questions that are inaccessible to earlier established techniques. The development of the real space imaging technique aims to integrate microwave excitations with LTEM and allow a direct study of skyrmion dynamics in real space. The reciprocal space studies combine state-of-the-art neutron scattering techniques and novel quantum chemistry calculations, with the broad aim to identify the microscopic conditions for Néel-type skyrmion lattice formation. By understanding how to use quantum chemistry calculations to predict the existence of skyrmions in new materials, it may eventually become possible to use the theory to further expand the family of skyrmion hosting materials and provide a fundamental understanding in skyrmion lattice formation at a microscopic level.

Chapter Two: Methodologies

In this chapter, the main techniques applied to study skyrmion lattice and their hosting materials during this thesis work are presented. Firstly, reciprocal space studies by means of neutron (and x-ray) scattering, and real space studies by means of Lorentz Transmission Electron microscopy (LTEM) are introduced. Then, the fundamental formalisms are discussed to understand why these techniques can reveal the magnetic properties of skyrmion lattice and why they were selected. The working principles of instruments realizing the experiments are also discussed briefly. In the last section of this chapter, an overview of essential simulation tools is given, along with explanations as to how they assist in understanding the results obtained from the mentioned techniques.

2.1 Fundamentals of neutron scattering

Neutron scattering is a powerful experimental technique for investigating the structure and dynamics of materials at the atomic scale. It is utilized in diverse fields beyond solid state physics, such as life science, engineering and earth science [38]. As a long-established technique, the main methods include neutron diffraction and neutron spectroscopy. However, the scope of instrument performance and analysis methods is continuously improving. Compared to other scattering probes such as x-rays, neutron scattering possesses unique characteristics and provides pivotal insights into magnetic properties in solids which remain either impossible or difficult to achieve with other probes.

Neutrons are massive particles that reside in an atom's nucleus together with protons. The mass of a neutron is close to the mass of a proton, but a neutron has no electric charge. Due to charge neutrality, neutrons only interact weakly with the nuclei in the target matter via nuclear forces, making them an ideal probe at the surface and in the bulk of materials. Further, neutrons can be produced in large quantities with wavelengths (0.6 Å – 20 Å) on the order of inter-atomic distances and energies (1 meV – 200 meV) on the order of many elementary excitations in solids. One can therefore obtain information on the atomic structure by performing neutron diffraction and measure the dispersion relation of excitations by performing neutron spectroscopy.

The neutron itself has a spin thus a magnetic moment. According to particle physics, neutrons are fermions and have spin ½. The spin is oriented antiparallel to the magnetic moment $\boldsymbol{\mu}$. A dimensionless constant g-factor connects these two quantities:

$$\mu = \frac{g\mu_N}{\hbar}\boldsymbol{I} \tag{2.1}$$

where $\boldsymbol{I}$ is the spin angular momentum, μ_N is the nuclear Bohr magneton.

The magnetic moment possessed by neutrons allows them to scatter from unpaired electrons constituting magnetic order in solids via electromagnetic forces. Similarly, the collective excitations from magnetically ordered structures, so-called magnons, can also be probed. In addition, spin-polarized neutron scattering can provide deeper interrogations of the magnetization distribution inside solids, and provide more detailed information on the orientations of magnetic moments and magnetic fluctuations at the atomic scale [39].

2.1.1 Scattering cross-section

The interaction between neutrons and a material is quantified by the cross-section σ, defined as the number of neutrons (N) scattered by the material normalized to the neutron beam flux Ψ:

$$\sigma = \frac{N}{\Psi} \qquad . \tag{2.2}$$

It can be visualized as the effective area of a nucleus in the target material seen by the incoming neutron beam. However, in real experiments the differential scattering cross-section $d\sigma$, is more commonly used:

$$\frac{d\sigma}{d\Omega} = \frac{1}{\Psi}\frac{N}{d\Omega} \qquad . \tag{2.3}$$

This quantity describes the number of neutrons scattered into a particular solid angle $d\Omega$, which is illustrated in Fig. 2.1.
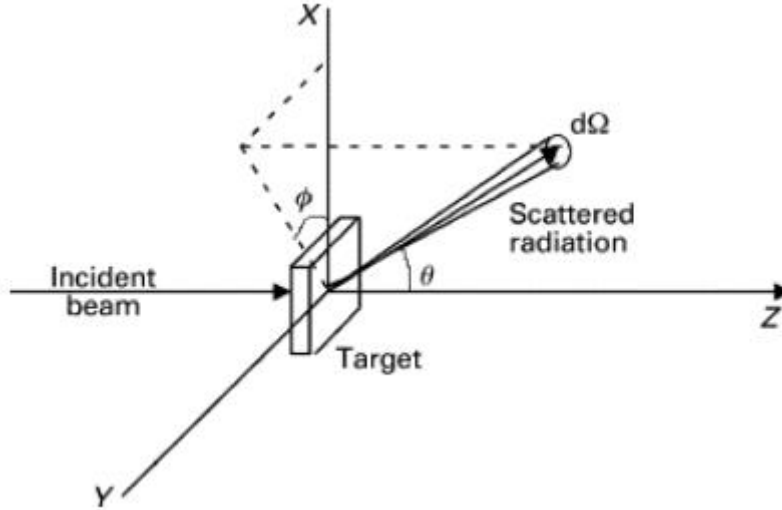
Fig. 2.1: Sketch to illustrate the differential cross-section. Neutrons are scattered to a solid angle dΩ with scattering angle 2Θ and azimuthal angle Φ. The incident and scattered neutron wavevectors are labelled by k_i and k_f, respectively. Image reproduced from Ref. [40].

The total scattering cross-section is therefore the integral of differential cross-section over the surface of a sphere:

$$\sigma = \int_0^{4\pi}\frac{d\sigma}{d\Omega}d\Omega \qquad . \tag{2.4}$$

In inelastic neutron scattering processes, where neutrons give away or absorb energy from the material, one needs to take into account the energy dependence of scattered neutrons. This gives rise to another quantity called the partial differential scattering cross-section:

$$\frac{d^2\sigma}{d\Omega dE_f} = \frac{1}{\Psi}\frac{N}{d\Omega dE_f} \tag{2.5}$$

where N is the number of neutrons within energy interval $[E_f, E_f + dE_f]$ scattered into solid angle $d\Omega$ per second. One needs to further integrate over the whole energy range to obtain the total scattering cross-section:

$$\sigma = \int_0^{4\pi}\int_{-\infty}^{\infty}\frac{d^2\sigma}{d\Omega dE_f}dE_f d\Omega \qquad . \tag{2.6}$$

In contrast to inelastic scattering, in elastic scattering processes where neutrons do not gain or lose energy, the magnitude of their wavevector remains unchanged $|k_i| = |k_f|$.

Given the cross-section definition, we now consider an ideal situation where neutrons are scattered by a single nucleus at a fixed position. Neutrons are scattered in all directions with equal probability, and the differential cross-section has a simple expression:

$$\frac{d\sigma}{d\Omega} = b_l^2 \qquad (2.7)$$

where b_l is called the scattering length characteristic for a particular isotope. Equation (2.7) has no angular dependence, so the total scattering cross-section simply reads:

$$\sigma = \int \frac{d\sigma}{d\Omega} d\Omega = 4\pi b_l^2 \qquad . \qquad (2.8)$$

The neutron scattering cross-section varies significantly from one element to another, even between different isotopes of the same element. Fig. 2.2 shows in a comparative way the variation of total neutron scattering cross-section and coherent scattering length from light to heavy isotopes and the respective x-ray data. One can learn that neutrons scatter strongly and coherently from light elements over a large distance, which is generally the reverse for x-rays. In particular, the neutron scattering cross-section is notably different for hydrogen (^{1}H) and deuterium (D), while these two isotopes cannot be distinguished using x-rays. This property endows neutron an irreplaceable role in life science research.
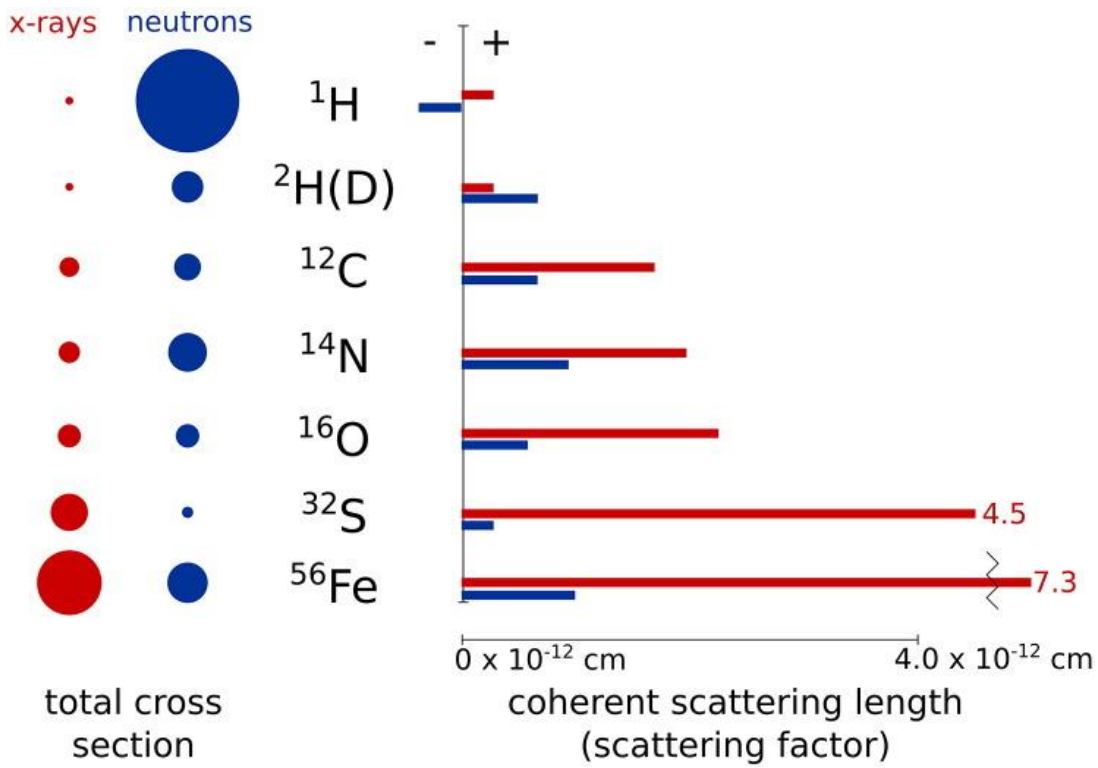
Fig. 2.2: X-ray and neutron scattering cross-sections and coherent scattering lengths for different isotopes. Circles and bars are drawn to scale. Image reproduced from Ref. [41].

2.1.2 Elastic neutron scattering cross-section

Assuming coherent neutron scattering, the cross-section of a system of multiple atoms is given by the coherent sum of the contributions from each particle:

$$\left(\frac{d\sigma}{d\Omega}\right)_{coh} = |\sum_l b_l \exp(i\boldsymbol{q} \cdot r_l)|^2 \qquad (2.9)$$

where $\boldsymbol{q}$ is called the scattering vector defined by the momentum transfer from incident neutron to the target material $\boldsymbol{k_i} - \boldsymbol{k_f}$. In the case of elastic neutron scattering, the energy transfer is zero and the magnitude of $\boldsymbol{k_i}$ and $\boldsymbol{k_f}$ are equal. This type of scattering process is shown in Fig. 2.3, and $\boldsymbol{q}$ can be expressed as:

$$\boldsymbol{q} = 2k\sin(\theta) = \frac{4\pi\sin(\theta)}{\lambda} \qquad . \qquad (2.10)$$
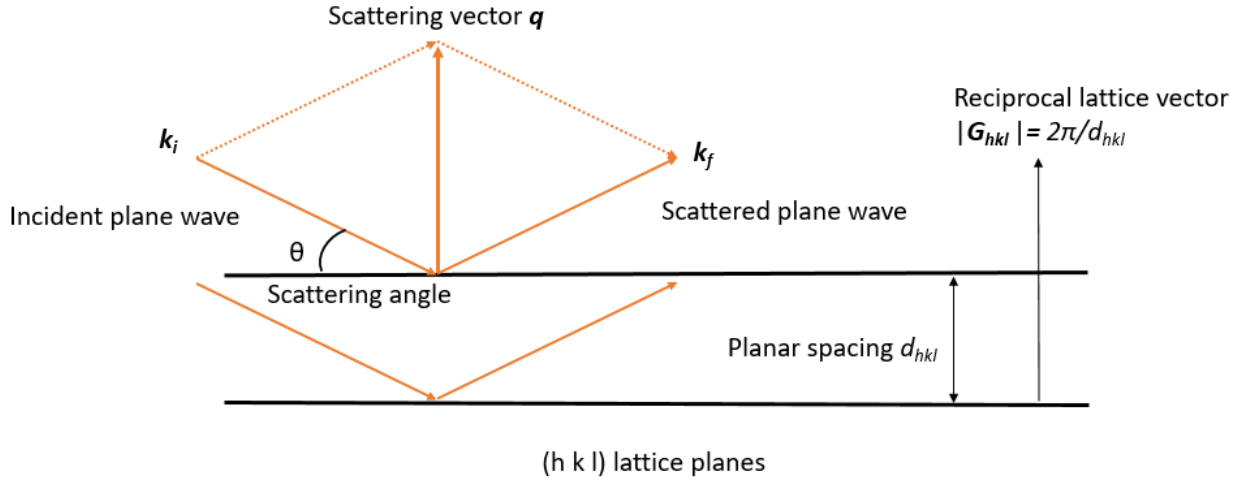
Fig. 2.3: Schematic illustration of elastic scattering for a lattice plane denoted by Miller indices (h k l).

In the following, coherently scattering neutrons are described in the wave picture. In Fig. 2.3, an incident neutron wave with wavevector k_i scatters from a particular lattice plane at an angle Θ. The scattered wave k_f changes direction while maintaining a magnitude identical to k_i. The lattice planes are labelled by Miller indices (h k l) with spacing d_{hkl}. When the path difference between lattice planes travelled by the incident wave and the scattered wave is equal to an integer multiple of the neutron wavelength, these two waves produce an interference pattern and Bragg diffraction may occur. In reciprocal space, this condition is equivalent to the scattering vector q being equal to a reciprocal lattice vector G_{hkl}:

$$q = G_{hkl} \qquad . \tag{2.11}$$

Equation (2.11) is known as the Bragg condition. The applications of this Bragg's law in experiments are discussed in Section 2.2.2. Further, the expansion in Equation (2.9) generates cross terms which lead to periodically enhanced and suppressed scattering intensity in real space. This is the interference between scattered neutron waves, the origin of several neutron scattering techniques such as neutron imaging [42]. Finally, Equation (2.10) tells that coherent scattering depends on the incoming neutron wavelength λ and scattering angle Θ.

To obtain an expression of the differential cross-section, one needs to start from considering the partial differential cross-section. In a quantum mechanical approach, the coherent partial differential cross-section can be evaluated by measuring the initial and final wavefunctions of incident and scattered neutrons. In general, the expression is given by the famous Fermi Golden rule:

$$\left(\frac{d^2\sigma}{d\Omega dE_f}\right)_{i \to f} = \frac{k_f}{k_i}\left(\frac{m}{2\pi\hbar^2}\right)^2 \left|\langle k_f, s_f, v_f | V | k_i, s_i, v_i \rangle\right|^2 \delta(\hbar\omega + E_i - E_f) \tag{2.12}$$

where the initial and final states are defined by wavevector (k_i and k_f), spin state (s_i and s_f) and neutron velocity (v_i and v_f). V represents the scattering potential. When neutrons scatter from a crystal lattice, the scattering potential can be modeled by a periodic potential:

$$V = \frac{2\pi\hbar^2}{m}\sum_l b_l \delta(r_l) \qquad . \tag{2.13}$$

Equation (2.13) indicates that the scattering potential of the lattice is given by the sum of potentials produced by each atom at position r_l. Here, the scattering potential from a single atom is determined by the scattering length b_l, which is called Fermi pseudo-potential assuming spherical symmetry. By substituting the potential, Equation (2.12) simplifies to:

24

$$\left(\frac{d^2\sigma}{d\Omega dE_f}\right)_{nuc} = \frac{k_f}{k_i}\frac{1}{2\pi\hbar}\sum_{l,l'}b_l b_{l'}\delta(\boldsymbol{r_l})\int_{-\infty}^{\infty}dt e^{-i\omega t}\langle e^{iq|\boldsymbol{r}_l(0)-\boldsymbol{r}_{l'}(t)|}\rangle \quad . \tag{2.14}$$

Integrating over energy in Equation (2.14), one can obtain the differential cross-section:

$$\left(\frac{d\sigma}{d\Omega}\right)_{nuc} = N_0\frac{(2\pi)^3}{v_0}\sum_\tau|F_N(\boldsymbol{q})|^2\,\delta(\boldsymbol{q}-\boldsymbol{\tau}), \quad F_N(\boldsymbol{q}) = \sum_l b_l\,e^{iq\cdot r_l}e^{-W_r} \tag{2.15}$$

where N_0 is the number of nuclei in the lattice, v_0 is the volume of unit cell. $F_N(\boldsymbol{q})$ is called nuclear structure factor, in which the site-dependent thermal fluctuations of atoms relative to their respective equilibrium positions are described via the Debye-Waller factor e^{-W_r}.

In reality, the scattered neutron signal measured in experiments has background noise. This is caused by incoherent scattering due to the fluctuations of atomic spin orientations or scattering lengths from one atom to another. The incoherent scattering cross-section has no interference terms in its expression, representing a constant scattering intensity in all directions.

In addition, the fact that neutrons can scatter from the magnetic structure of materials gives rise to an additional magnetic scattering cross-section. The scattering potential consists of contributions from electron spin dipole moments and electron orbital moments. In brief, the magnetic scattering length for an individual ion is expressed as:

$$\mathrm{b}_l = \Upsilon r_0 F(\boldsymbol{q})\frac{g}{2}\boldsymbol{\sigma}\cdot s_{l,\perp} \tag{2.16}$$

where Υ is a dimensionless constant called neutron gyromagnetic ratio, r_0 is the classical electron radius, g is the g-factor already seen in Equation (2.1), $\boldsymbol{\sigma}$ is the neutron spin, and s_l is the atomic spin in the material. Equation (2.16) implies that magnetic scattering is spin-dependent, and the incident neutron spin is only sensitive to the spin component $s_{l,\perp}$ which is perpendicular to the scattering vector $\boldsymbol{q}$. The $F(\boldsymbol{q})$ term is known as magnetic form factor:

$$F(\boldsymbol{q}) = \int \exp(i\boldsymbol{q}\cdot\boldsymbol{r})\rho_s(\boldsymbol{r})\,d^3r \tag{2.17}$$

where $\rho_s(\boldsymbol{r})$ is the normalized spin density distribution in space. The magnetic form factor is unity at zero momentum transfer $\boldsymbol{q}$ = 0, and falls off exponentially as the scattering vector increases. These properties of the magnetic scattering cross-section are observable in the measured magnon spectrum in the scattering project results, presented in Chapter Three. The general equation for neutron scattering by periodic magnetic structure is the following:

$$\left(\frac{d^2\sigma}{d\Omega dE_f}\right)_{mag} = \frac{k_f}{k_i}\frac{\Upsilon r_0^2}{2\pi\hbar}\sum_{\alpha,\beta}(\delta_{\alpha,\beta}-\frac{q_\alpha q_\beta}{|\boldsymbol{q}|^2})\sum_{l,l'}\frac{1}{4}g_l g_{l'}F_l(\boldsymbol{q})F_{l'}^*(\boldsymbol{q})$$

$$\times \int_{-\infty}^{\infty}dt e^{-i\omega t}\langle e^{iq|\boldsymbol{r}_l(0)-\boldsymbol{r}_{l'}(t)|}\rangle\langle S_l^\alpha(0)S_{l'}^\beta(t)\rangle \tag{2.18}$$

where S_l^α represents the α component of the spin at a magnetic atom labelled by l, $\langle S_l^\alpha(0)S_{l'}^\beta(t)\rangle$ is called pair correlation function of two magnetic moments over time t.

Similar to the atomic lattice, neutrons can scatter elastically from a periodic magnetization density formed by unpaired electrons. Bragg's law also applies in magnetic elastic scattering, while d_{hkl} becomes the spacing of (h k l) planes in the magnetic lattice structure in Fig. 2.3, and the momentum transfer is equal to a magnetic reciprocal lattice vector $\boldsymbol{k}$ (also called magnetic propagation vector) in Equation (2.11). Since the skyrmion lattice is often considered to be a magnetic lattice, elastic neutron scattering technique can probe its lattice

arrangement, symmetry, ordering and spatial frequencies. By integration over energy again, one obtains an expression for magnetic differential cross-section:

$$\left(\frac{d\sigma}{d\Omega}\right)_{mag} = N_0 \frac{(2\pi)^3}{v_0} \Sigma_k \left|F_{M,\perp}(\boldsymbol{q})\right|^2 \delta(\boldsymbol{q} - \boldsymbol{k}) \qquad ,$$

$$F_M(\boldsymbol{q}) = \Upsilon r_0 \Sigma_l \frac{1}{2} g_l F_l(\boldsymbol{q}) \, \boldsymbol{s}_l^k e^{i\boldsymbol{q}\cdot\boldsymbol{r}_l} e^{-W_r} \qquad . \tag{2.19}$$

Compared with the nuclear structure factor in Equation (2.15), the magnetic structure factor $F_M(\boldsymbol{q})$ is a vector determined by the atomic spin $\frac{1}{2} g_l \boldsymbol{s}_l^k$. Both the magnetic form factor $F(\boldsymbol{q})$ and the Debye-Waller factor e^{-W_r} are included in the expression of magnetic structure factor, while the latter is often neglected when studying magnetic orders at cryogenic temperatures.

2.1.3 Inelastic neutron scattering cross-section

In inelastic scattering, neutrons can exchange momentum and energy with the particle-like excitations in the atomic lattice (phonons) or the magnetic lattice (magnons). According to particle physics, phonons and magnons are bosons with spin zero, thus obeying Bose-Einstein statistics. The momentum transfer is given by the sum of the reciprocal lattice unit vector and the scattering vector:

$$\boldsymbol{k}_f - \boldsymbol{k}_i = \boldsymbol{\tau} + \boldsymbol{q} \tag{2.20}$$

The partial differential cross-section of one phonon scattering is given by:

$$(\frac{d^2\sigma}{d\Omega dE_f})_{phonon} = \frac{k_f}{k_i} \frac{(2\pi)^3}{2v_0} \Sigma_s \Sigma_\tau \, \delta(\boldsymbol{Q} - \boldsymbol{q} - \boldsymbol{\tau}) \, \delta(\omega - \omega_{q,s}) \frac{\langle n_{q,s}+1 \rangle}{\omega_{q,s}} |F_{ph(Q)}|^2 \tag{2.21}$$

where $\langle n_{q,s} + 1 \rangle$ is the expectation value of the phonon number with momentum $\boldsymbol{q}$ and spin $\boldsymbol{s}$ according to Bose-Einstein statistics. The expression is given by:

$$\langle n_{q,s} + 1 \rangle = \frac{e^{\hbar\omega_{q,s}/k_B T}}{e^{\hbar\omega_{q,s}/k_B T} - 1} \tag{2.22}$$

and $\omega_{q,s}$ is an eigenfrequency which is consistent with the phonon dispersion relation. The structure factor for phonon scattering is given by:

$$F_{ph(Q)} = \Sigma_l \frac{b_l}{\sqrt{M_l}} e^{i\boldsymbol{q}\cdot\boldsymbol{r}_l} e^{-W_r}(\boldsymbol{q} \cdot \boldsymbol{e}_{r,s}) \tag{2.23}$$

where M_l is the mass of the nucleus, $\boldsymbol{e}_{r,s}$ is the polarization vector of the phonon excitation. Therefore, only lattice vibrations parallel to the scattering vector $\boldsymbol{q}$ can be detected. An important observation from Equation (2.21) to Equation (2.23) is that the cross-section of phonon scattering is proportional to $|\boldsymbol{q}|^2$. Similar to phonon scattering, one also can derive the partial differential cross-section for one-magnon scattering:

$$(\frac{d^2\sigma}{d\Omega dE_f})_{magnon} = \frac{k_f}{k_i} \frac{\Upsilon r_0^2}{2\pi\hbar} \Sigma_{\alpha,\beta}(\delta_{\alpha,\beta} - \frac{q_\alpha q_\beta}{|\boldsymbol{q}|^2}) \Sigma_{l,l'} \frac{1}{4} g_l g_{l'} F_l(\boldsymbol{q}) F_{l'}^*(\boldsymbol{q}) e^{-2W_r}$$

$$\Sigma_{q,\tau} \delta(\omega - \omega_{q,s}) \delta(\boldsymbol{Q} - \boldsymbol{q} - \boldsymbol{\tau}) \langle n_{q,s} + 1 \rangle \tag{2.24}$$

where $\langle n_{q,s} + 1 \rangle$ becomes the expectation value of magnon number according to Bose-Einstein statistics. In contrast to phonon scattering, the cross-section of magnon scattering scales with the square of magnetic form factor $F(\boldsymbol{q})$ which decreases as the scattering vector $\boldsymbol{q}$ increases. Only spin fluctuations perpendicular to the scattering vector $\boldsymbol{q}$ can be detected as for the magnetic elastic scattering cross-section.

2.2 Neutron scattering instruments and techniques

As a versatile technique, a variety of scattering methods using neutrons have been developed over the past 70 years. This section focuses on three techniques that are adopted during this thesis work: small-angle neutron scattering (SANS), neutron diffraction and neutron spectroscopy. At first, a brief overview of neutron instruments is introduced, from neutron generation to neutron detection. Detailed discussions on neutron instruments and these three techniques can be found in the textbook [43].

2.2.1 Neutron instruments

Currently, there are two major types of neutron production methods in the world's neutron beamline research facilities: fission source (e.g., Institute Laue Langevin, France) and spallation source (e.g., ISIS neutron source, UK). Fission sources can produce a high, continuous flux of neutrons from a conventional fission reactor. In spallation sources, pulsed neutrons are produced by bombarding heavy elements with accelerated high energy protons, and the flux is typically lower than that in fission sources. After generation, high energy neutrons are decelerated in a moderator comprising a tank of water or heavy water to energies in the meV range. Depending on the energy, the decelerated neutrons are commonly classified into thermal neutrons (14 meV – 200 meV) and cold neutrons (0.05 meV – 14 meV).

The neutron guide is a neutron conducting channel, and its principle is similar to optical fiber utilizing total internal reflection. Neutron guides can extract neutrons from the moderator and deliver them to devices that only allow a small portion of the beam through. These devices are generally known as "velocity selectors" in many neutron beamlines. Common velocity selectors are choppers, which are spinning devices that allow neutrons to pass only at selected times. Thus, neutrons with specific velocities matching the spinning speed of the chopper can pass. Choppers are ubiquitously used at spallation sources. They may also be used at continuous fission sources, where a crystal lattice (i.e. monochromators) select neutrons of a certain velocity according to the Bragg's law. Therefore, only neutrons of certain wavelengths are incident on the sample. Typically, only the first-order scattered neutrons (n = 1) are the desired neutrons, and higher orders (n > 1) are removed by filters. To control the resolution and background noise contributions to the scattering, slits and collimator devices can be installed at various positions in the scattering path, dependent on the exact instrument used.

Many neutron detectors adopt a nuclear reaction between the neutron and ^{3}He nuclei in order to detect a neutron scattering event:

$$^3\text{He} + n \rightarrow \,^3\text{He} + \,^1\text{He} + Q \quad.$$

(2.25)

Here a neutron is captured by ^{3}He and energy Q is released in the form of heat. The proton in the product generates an electrical signal which is subsequently amplified and detected. This is commonly done by a gas filled proportional counters using ^{3}He gas. Quench gas is also added to control the ionization process. Finally, beam monitors (i.e. a low efficiency detector) are often used together with the main detector to normalize the detected intensity. The detector can be either a 1D point detector, or 2D multidetector, depending on the beamline.

In neutron scattering, the equipment to control temperature, pressure and external fields is called sample environment. For instance, at SINQ – the Swiss Spallation Neutron Source, Paul Scherrer Institute, any temperature between 100 mK and 1800 K, any magnetic field up to 15 T and any high pressure up to 100 kbar can be achieved, and often in combination with one another. Low temperature down to 4 K is created by close-cycle refrigerators, and 1.5 K can be achieved by helium cryostats which also allow precise

temperature control. Superconducting magnets are employed to apply magnetic field up to 15 T. In the scattering project of this thesis work, skyrmion hosting material $VOSe_2O_5$ was studied below Curie temperature 7.5 K down to 1.5 K, and only low magnetic fields were applied up to 10 mT. Finally, a unique high-voltage (up to 5 kV) sample stick exists at PSI which fits into the cryomagnet. This stick makes it possible to apply electric field to the sample and study the resultant effects by neutron scattering. Since $VOSe_2O_5$ has magnetoelectric coupling according to Ref. [23], an attempt was made to use electric field to control the skyrmion lattice in this system.

2.2.2 Small-angle neutron scattering

SANS is an elastic scattering technique widely used in probing periodic structures in solids where the periodicity scale varies from 10 nm up to 1000 nm. The principle of SANS is based on the Bragg law:

$$n\lambda = 2d\sin(\Theta) \tag{2.26}$$

where n is the diffraction order, λ is the neutron wavelength typically at the order of 1-10 Å, d is the periodicity of the structure being probed, and Θ is the scattering angle. By "small angle", it means that the periodicity d is much larger than the neutron wavelength λ, therefore, a small scattering angle Θ is required to observe the scattering pattern. From the perspective of coherent neutron scattering cross-section in Equation (2.9), when the small-angle condition is met, the exponent in the phase term $|\boldsymbol{q}|d \ll 2\pi$ varies slowly over the whole lattice structure. This leads to strong coherent scattering over a large distance with respect to the unit cell, producing symmetric spot-like patterns characteristic of the lattice symmetry with high intensity. The intensity distribution can be theoretically calculated according to Equation (2.15) for periodic atomic structures and Equation (2.19) for periodic magnetic structures, assuming that the kinematic condition for diffraction is met in the SANS regime.

Due to the small scattering angle (0.5 to 5 degrees), the neutron detector in a SANS instrument is positioned at a long distance from the sample chamber (typically at least 10 meters) so that the scattering from the atomic or magnetic structure can be resolved from the direct beam at the 2D detector. The overall resolution is determined by incident neutron wavelength spread, the collimation length and detector pixel resolution. Since the periodicity of skyrmion lattice ranges from 20 to 200 nm, SANS is a suitable tool to investigate its properties. For this reason, SANS was one of techniques adopted in this thesis work. A simplified SANS setup at the SANS-I beamline, PSI is provided in Fig. 2.4.
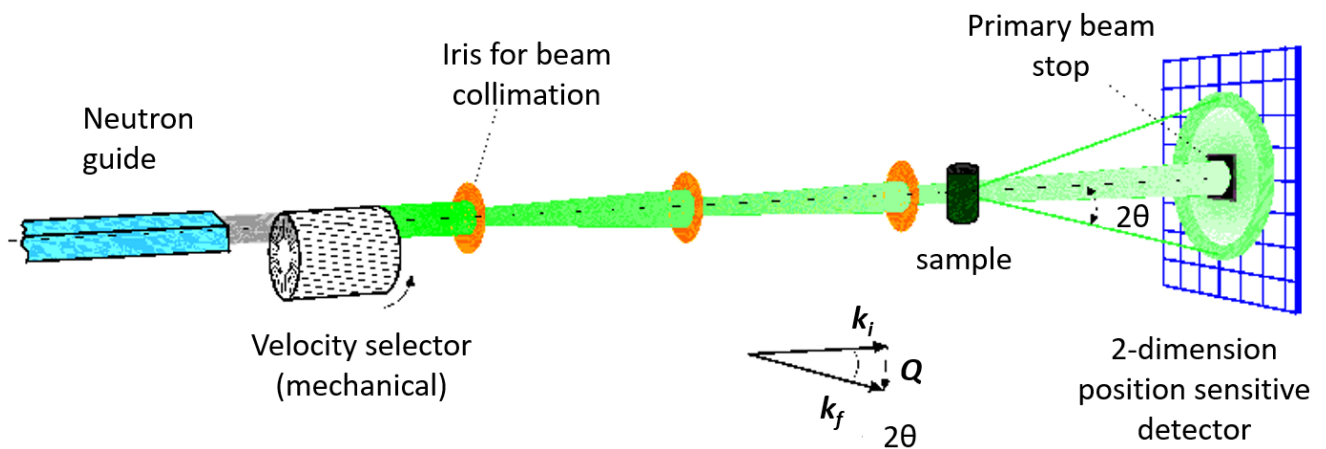
Fig. 2.4: Schematic illustration of a typical SANS setup equipped with a 2D detector. The beamstop prevents the direct beam from damaging the detector. Image copied from the official website of the SANS-I beamline, PSI [44].

2.2.3 Neutron diffractometer

A neutron diffractometer is employed to determine the symmetries and structures of both crystal lattice and magnetic orders. The sample can either be in a single crystal or in a powder form. The intensities from Bragg reflections are measured by a rotatable 1D point or 2D detector, while the angle of reflection (2θ) is recorded with high precision by a goniometer. Fig. 2.5 shows the layout of the single crystal neutron diffractometer at the Zebra beamline, PSI. The peak positions with neutron scattering selection rules give information on the lattice symmetry, and the intensities give information on the structure factor. For determining the correct model, candidate structures can be refined against datasets of integrated intensities using software such as Fullprof [45]. The expected intensities of nuclear peaks based on the presumed structure can be calculated using Equation (2.15).
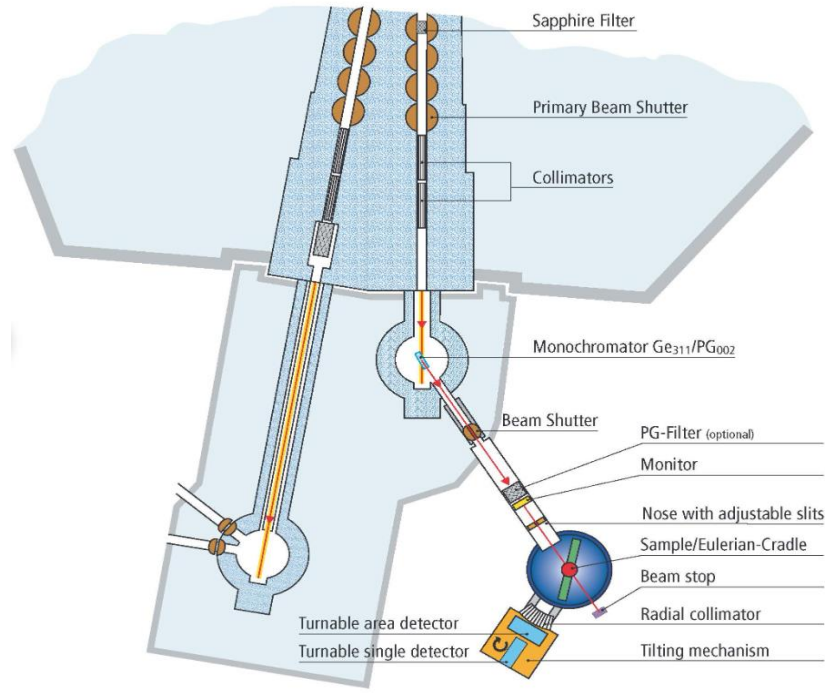
Fig. 2.5: Schematic illustration of a single crystal neutron diffractometer equipped with a 1D point detector and a 2D detector. Image copied from the official website of the Zebra beamline, PSI [46].

When a magnetic sample is studied, neutron diffractometers can also be applied to determine the spin configuration of various magnetic states. For commensurate magnetic orders, the magnetic Bragg reflection intensities may overlap with nuclear reflection intensities. Therefore, the integrated intensities at these positions are measured twice: above and below the Curie temperature, and the difference is the contribution from magnetic Bragg scattering. Similar to atomic structure, refining candidate model spin configurations (according to Equation (2.19)) against the subtracted integrated intensity data allows us to obtain the most likely spin configuration in different magnetic phases.

2.2.4 Neutron spectroscopy

For the inelastic neutron scattering technique, a spectrometer is implemented. The detector counts the number of neutrons with certain energy transfer $\hbar\omega$ and momentum transfer $\boldsymbol{q}$. Therefore, a dispersion relation $\omega(\boldsymbol{q})$ associated with the excitations in solids can be obtained. Currently, there are two main types of neutron spectrometers: triple-axis spectrometers (TAS) and time-of-flight (ToF) spectrometers. Since in this thesis work only TAS-type spectrometers were used for experiments, this section discusses only this type of spectroscopy instrument.

Fig. 2.6 shows the composition of the TAS located at the TASP beamline, Paul Scherrer Institute. The rotatable sample chamber allows users to scan the incoming neutron wavevector k_i. By using an analyzer, it is possible to measure the scattered neutron wavevector k_f and energy E_f. The scattered neutrons are calibrated at the exit position of the analyzer according to their E_f and k_f. The ^{3}He detector tube is a single-point detector that is placed after the analyzer and counts scattered neutrons at each position. Therefore, TASP allows one to focus on selected points on the dispersion $\omega(q)$, and typically one measures with point-by-point scans, by either scanning the momentum transfer q while maintaining a constant neutron energy transfer, or scanning energy transfer and maintaining a constant q. As a consequence, TAS is usually time-consuming when mapping out the whole dispersion relation in every branch. Compared with ToF-type instruments however, the higher focused intensity of the TAS technique can be advantageous when studying specific points on the dispersion.
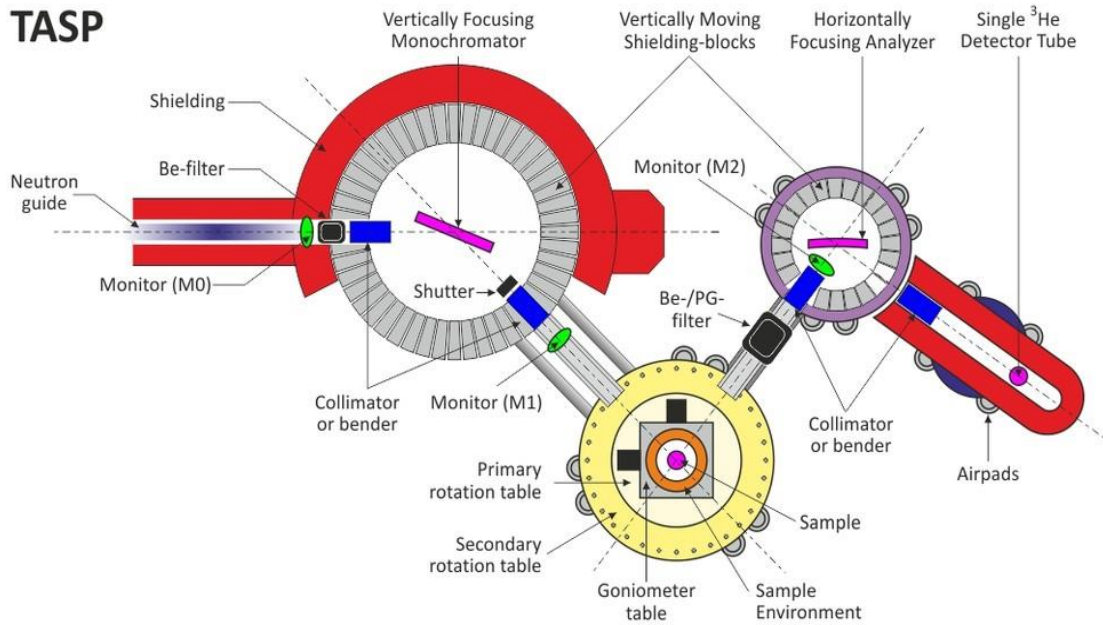
Fig. 2.6: A schematic layout of the triple-axis spectrometer at the TASP beamline, Paul Scherrer Institute. Image copied from the official website of the institute [47].

In this thesis work, we have used a recent technical upgrade of the TAS concept. This new TAS instrument is equipped with multiple detector arrays which improve the mapping capabilities, so the mapping efficiency of dispersion relations normally only possible at ToF beamlines becomes feasible. In contrast to the point detector TAS, there is an array of position-sensitive ^{3}He detector tubes. Fig. 2.7 (a) provides the schematics of the CAMEA (Continuous Angle Multiple Energy Analysis) beamline spectrometer, located at Paul Scherrer Institute, where a series of eight upward scattering analyzer arcs diffract neutrons onto a detector array consisting of 104 position-sensitive ^{3}He tubes. A prism analyzer is employed, which records a range of neutron energies for each analyzer segment. Its working principle is sketched in Fig. 2.7 (b). Cross-talk shielding prevents the interference between different analyzers. This spectrometer simultaneously delivers scattered neutrons to the corresponding pre-calibrated detector tube and allows users to obtain the whole dispersion efficiently with a TAS-based instrument.

Depending on the incident neutron energy, TAS instruments can be classified into cold neutron TAS and thermal neutron TAS. This translates into a range of energy transfer over which excitations can be studied most efficiently, so the choice of beamline needs to consider the energy range of the excitation in the material under investigation. Generally, a cold TAS covers energy transfer from zero to 4 ~ 5 meV, while a

thermal TAS can measure from 4 meV to 50 meV. In this thesis work, the magnon excitations up to energy transfers 6 meV were studied in the skyrmion hosting material $VOSe_2O_5$ at magnetic ground state, thus both cold and thermal TAS were used.

(a)   **(b)**
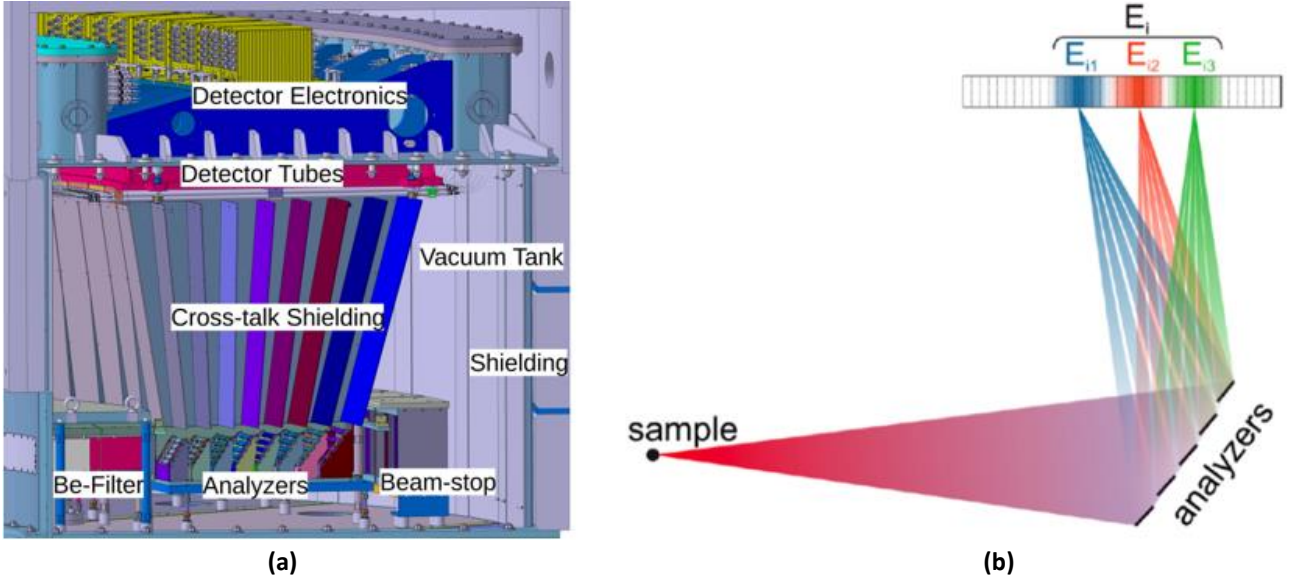
Fig. 2.7: (a) A schematic layout of the Continuous Angle Multiple Energy Analysis (CAMEA) spectrometers at Paul Scherrer Institute; (b) the working principle of the prism analyzer in this spectrometer. Both Images were copied from the official website of the institute [48].

When it comes to performing measurements and analyzing TAS data, one needs to take into account the instrument resolution. The resolution volume is a 4D ellipsoid in energy-momentum space. Its orientation depends on the TAS instrument and scattering geometry, as indicated in Fig. 2.8. The resulting influence of the orientation of the resolution ellipsoid can be manifested as a broad or sharp peak depending on the mutual orientations between the ellipsoid and the dispersion. Therefore, one needs to choose between performing a constant energy scan or a constant q scan. The criterion is to select the one that produces a sharp peak in intensity.
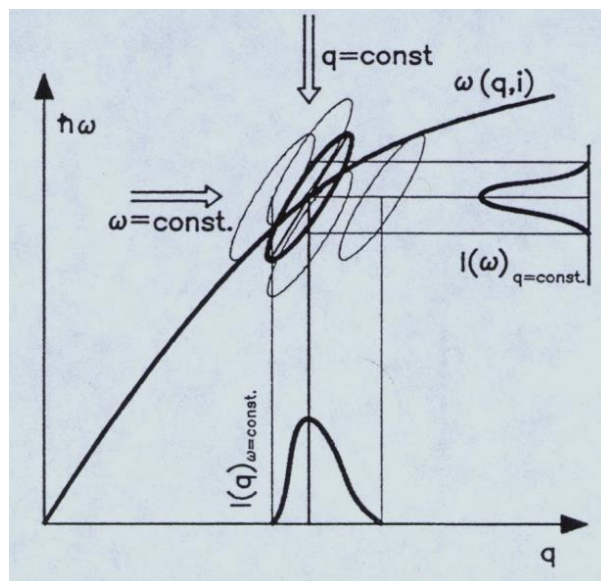
Fig. 2.8: Demonstration of the resolution effect in a TAS instrument, showing the resulted constant energy and constant q scans when the resolution ellipsoid crosses the dispersion curve. Image reproduced from Ref. [49].

2.3 Principles of Lorentz transmission electron microscopy

The transmission electron microscope (TEM) is another versatile experimental tool offering both real and reciprocal space investigations based on collimated, high energy electron beams. Since it is relatively easy to produce and manipulate electron beams, there are various techniques to use electrons for probing atomic structures, magnetism and excitations in solids, for example, high resolution TEM, magnetic imaging, electron diffraction and electron energy loss spectroscopy (EELS). Electrons have an electric charge, so compared with neutrons, they interact strongly with materials via electromagnetic forces and cannot probe bulk sample volumes. Consequently, TEM samples are made very thin, typically on the order of 100 nm. Focused Ion Beam (FIB) is one of the commonly adopted TEM sample preparation methods, where a bulk material is milled by heavy metal ions (usually gallium) until a thin film (lamella) is taken out and attached to a standard TEM grid called omniprobe, as shown in Fig. 2.9.
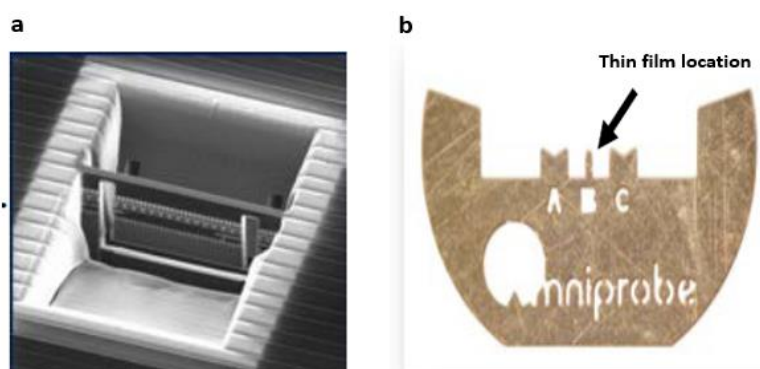
Fig. 2.9: (a) A thin film in the bulk sample, milled by FIB; (b) a standard TEM grid called omniprobe. The arrow indicates the position where the lamella is attached.

In addition, electrons are fermions with spin ½, thus they can interact with the magnetic moment of atoms in materials. Electrons are deflected by Lorentz force and then form magnetic contrasts on the camera. TEM operating at this mode is called Lorentz transmission electron microscope (LTEM), which is a powerful tool to obtain real space images of magnetic textures. By far, most real space studies of skyrmions are performed with LTEM. However, for Néel-type skyrmions, their spins deflect electrons rotationally. Hence it is necessary to tilt the sample at a large angle to form magnetic contrasts. In this circumstance, electrons in LTEM have limited coherence and thus, limited spatial resolution. An alternative imaging technique named magnetic force microscopy (MFM) has been applied to GaS_4V_8 [8] – one of Néel-type skyrmion hosting materials. Here, a magnetically coated cantilever is scanned over the magnetic specimen and deflected characteristically by its magnetic stray fields. Moreover, x-rays can allow several magnetic imaging techniques, such as magnetic transmission soft x-ray microscopy (MTXM) [50] and x-ray photoemission electron microscopy (x-PEEM) [51]. Because $VOSe_2O_5$ hosts Néel-type skyrmion lattice, LTEM is not suitable to study this material and it was mainly studied in reciprocal space by neutrons in this thesis work.

2.3.1 Components of a transmission electron microscope

A standard commercial TEM consists of the following components: electron source, condensing system, objective and projective system, and lastly, a 2D electron detector. Fig. 2.10 and 2.11 provide photos and schematics of two main components in an electron source: electron gun and Wehnelt electrode, respectively. The electron gun emits electrons which are then accelerated to the desired energy (typically 200 keV) by the electric field produced between the cathode and anode. There are two significant types of electron guns: thermionic guns, where electrons are emitted by heating the filament to a high temperature; field emission guns, where electrons are extracted by a large potential gradient between the emitter surface and nearby

electrodes. Field emission guns usually produce more coherent electron beams with higher brightness than thermionic guns. However, it is more technically complex to implement them because an extremely high vacuum environment is required. In the project of ultrafast LTEM in this thesis work, a thermionic gun was used because the electron source column is equipped with an additional mirror to produce photoelectrons so the TEM is not vacuum compatible with field emission sources.

(a)   (b)
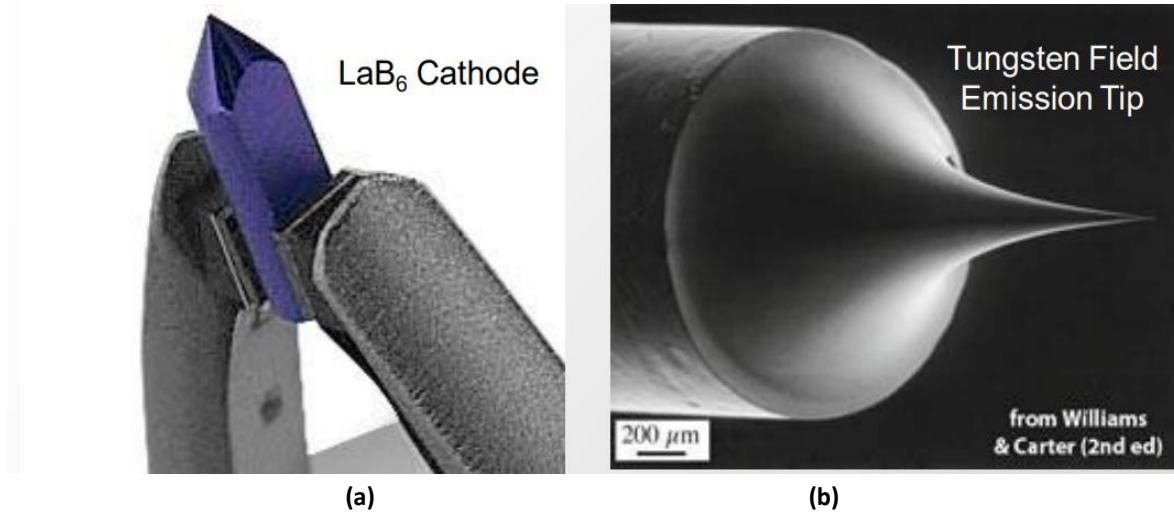
Fig. 2.10: Photos of standard commercial (a) thermionic LaB₆ electron gun and (b) field emission tungsten gun.

The electron source also contains a Wehnelt electrode – a hollow cylinder positioned directly below the electron gun. It is biased with a small negative voltage (around 200 V) opposing the cathode-anode voltage. The emitted electrons experience the Wehnelt bias before they are accelerated. This negative bias creates a repulsive electric field which suppresses electron emissions from most areas of the filament and enhances the beam coherence. As a result, an electron beam crossover (Fig. 2.11) is formed between the cathode and anode. Therefore, the Wehnelt also serves as an effective convergent lens and determines the emission area, beam current and convergent angle. By carefully tuning the Wehnelt bias, one can balance the loss in beam current and improvement in beam coherence. The control over the beam crossover is essential in producing a parallel or convergent beam at the sample position.
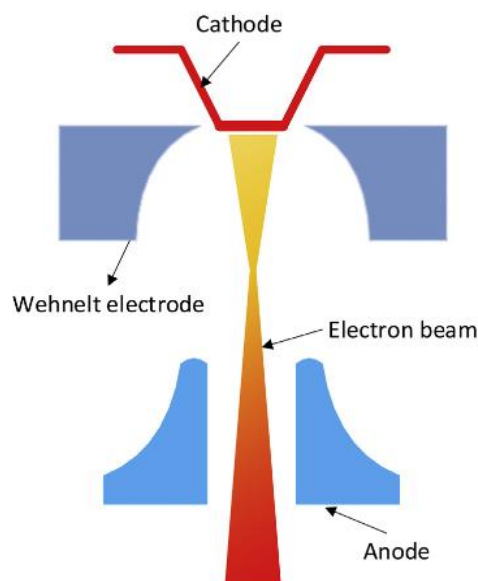
Fig. 2.11: Schematic illustration of an electron source, consisting of an electron gun (not shown) above the cathode, a Wehnelt electrode and an anode. Image reproduced from Ref. [52].

33

The electron beam is accelerated to the desired energy, and then it enters the condensing system, comprising of condenser lenses, a condenser aperture and scanning coils, as shown in Fig. 2.12. The purpose of the whole system is to produce a uniform, coherent, monochromatic and intense beam on the sample, with the ability to magnify/demagnify and shift the gun crossover. There are typically three condenser lenses in a TEM: the first condenser lens (C1) defines the probe size; the second condenser lens controls the illumination area and beam intensity; the third condenser lens, also called the condenser mini-lens, controls the convergence angle. The scanning coils allow users to shift the beam over the sample. It is noted that the principles of electron lenses are based on Lorentz force acting on electrons. A strong magnetic field is required to deflect high-energy electrons. Therefore, the metals producing magnetic field are compactly arranged in a small area, and electrons pass through the pole-piece gap. As a result, the images produced by TEM are rotated.

| (a) | (b) |
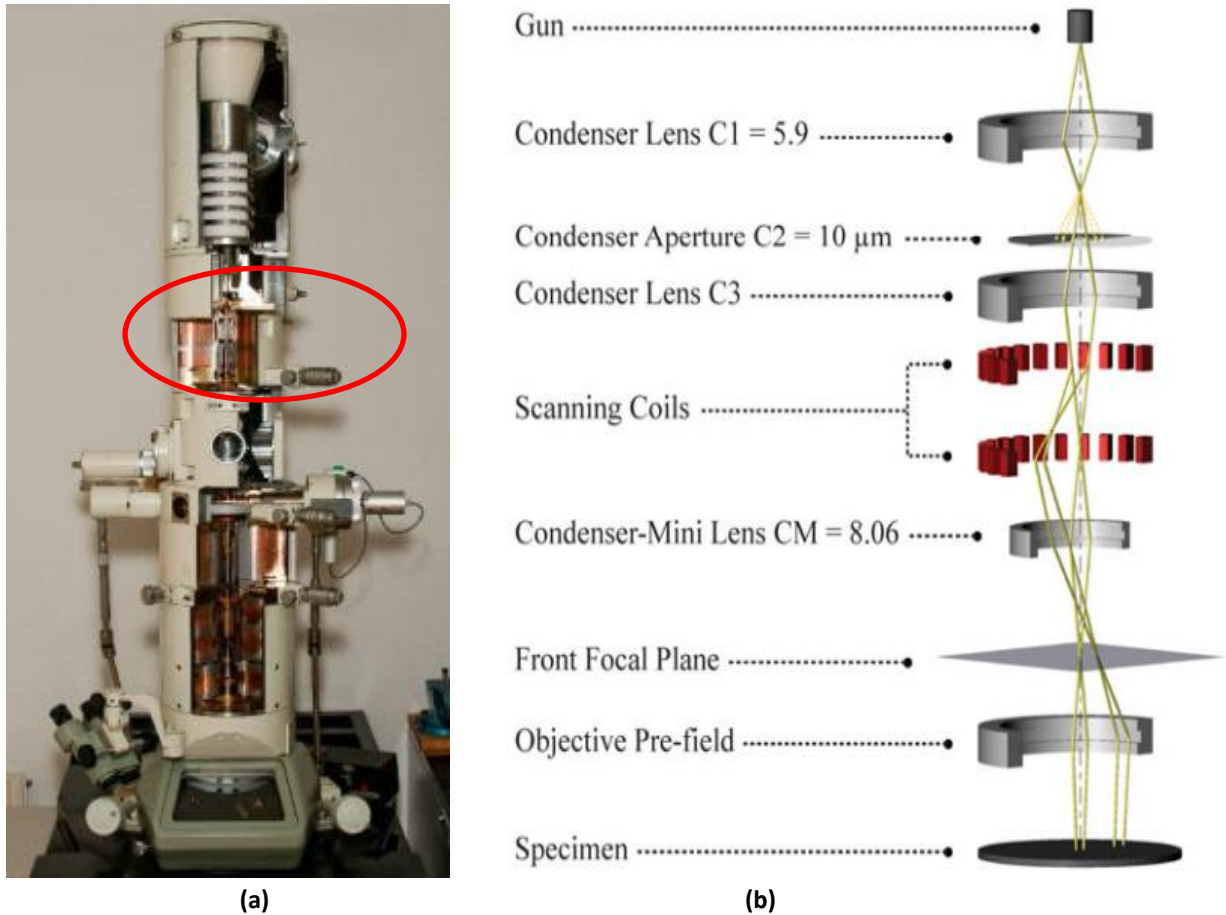
Fig. 2.12: (a) A photo and (b) schematic illustration of the TEM condensing system. The schematic image is reproduced from Ref. [53].

After the electron beam impinges the sample, the scattered electrons enter the objective lens shown in Fig. 2.13. Real space images and diffraction patterns are formed at the back focal plane and the first image plane, respectively. The intermediate lens selects whether the projective lens magnifies the diffraction pattern or the real space image at the camera. It allows users to switch between diffraction mode and imaging mode. The most common TEM camera is a CCD (charge-coupled device) which stores electrons in a potential well under each pixel. The stored charges are amplified and digitalized, forming an image or a sample diffraction pattern.
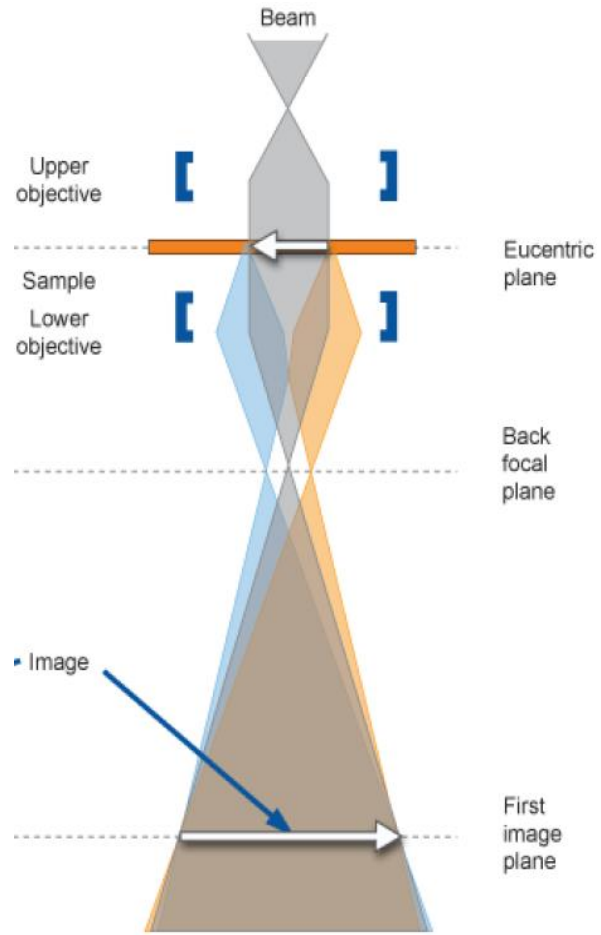
Fig. 2.13: A photo and schematic illustration of the TEM objection and projection system.

Finally, TEM is capable of studying materials under various types of sample environments. For example, an external magnetic field can be applied to the sample by objective lens; temperature control is realized by customized sample holders with liquid nitrogen or liquid helium flow cycles. The recently developed pump-probe technique in TEM even allows external excitation in the sample induced by ultrafast laser. In this thesis work, a unique microwave excitation system is proposed, and its details are presented in Chapter Four.

2.3.2 LTEM and operation modes

From a classical point of view, consider an electron beam experiencing Lorentz force generated by the magnetic induction **B** and electric field **E** from the sample:

$$\mathbf{F} = -e(\boldsymbol{E} + \boldsymbol{v} \times \boldsymbol{B}) \tag{2.27}$$

where *e* is the electron charge 1.602 x 10 $^{-19}$ C. The deflection angle of the electron beam passing through a sample with magnetic induction **B** and thickness *t* is given by:

$$\theta_L = \frac{e\lambda}{h} B_\perp t \tag{2.28}$$

where λ is the electron wavelength, and *h* is the Plank constant. Equation (2.28) tells that the field component perpendicular to the electron beam trajectory ($B_\perp$) determines the deflection angle. The Lorentz deflection angle is typically two orders of magnitude smaller than Bragg scattering angles. Therefore, the magnetic contrast can be easily differentiated from contrast formed by atomic structures.

When using LTEM to investigate magnetic samples, a dedicated objective lens – called objective mini-lens or Lorentz lens is employed to form an image of the magnetic structures in the sample. Compared with the main objective lens, the Lorentz lens has weak focusing power and does not exert a significant magnetic field on the sample, creating an almost magnetic field free sample environment. The main objective lens is switched on only when applying an external magnetic field is required, for example, when simulating the phase transition from the helical phase to the skyrmion phase in chiral magnets. By sweeping the temperature and magnetic field, one can obtain different magnetic textures and map out the phase diagram of the sample.
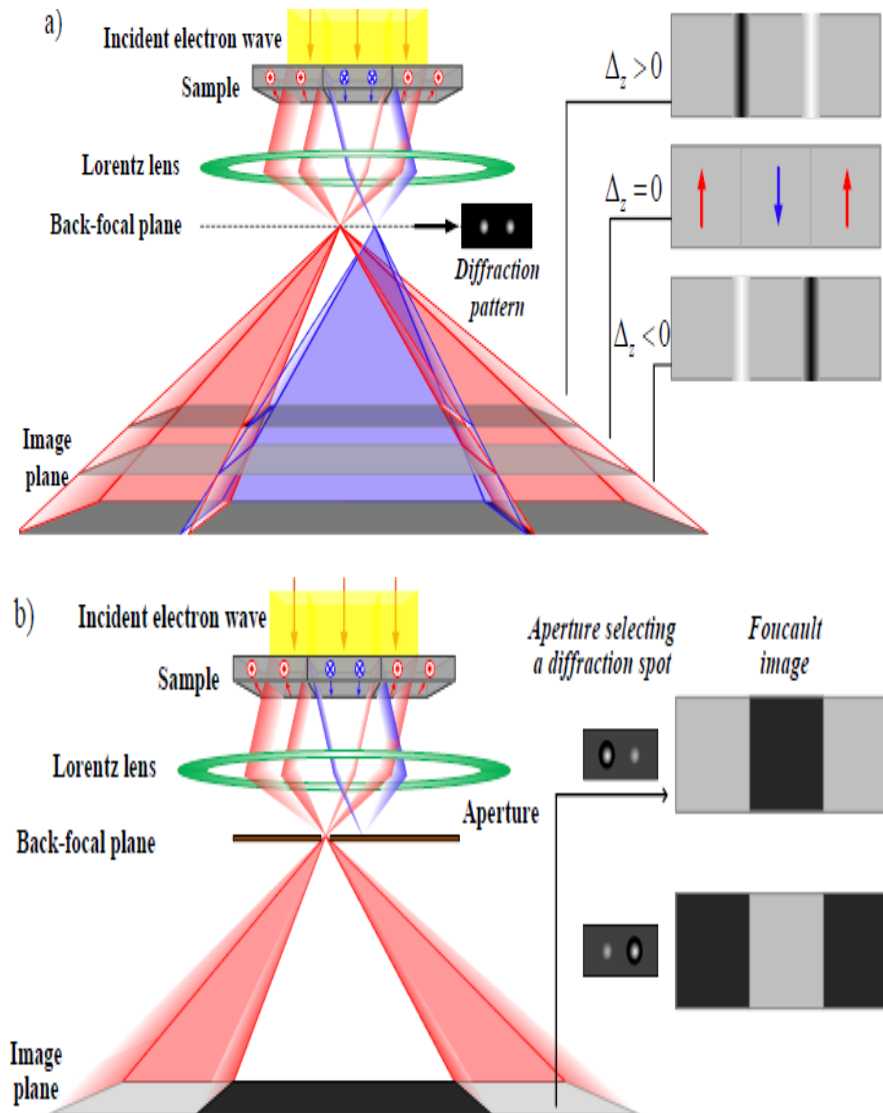
Fig. 2.14: Schematic illustrations of magnetic imaging in LTEM in (a) Fresnel mode and (b) Foucault mode. The sample has ferromagnetic domains with parallel or anti-parallel spin orientation. Image reproduced from Ref. [54].

For the observation of magnetic contrasts and textures, LTEM can operate in two modes: Fresnel mode and Foucault mode. The principles of each mode are displayed in Fig. 2.14, where a magnetic sample with parallel or anti-parallel ferromagnetic domains was used for illustration. The electron beam is deflected in opposite directions by domains with opposite spin orientations. The Fresnel mode is implemented by defocusing the objective lens, leading to areas of enhanced and reduced intensities on the camera. In Fig. 2.14 (a), the image with the defocusing parameter $\Delta_z > 0$ is obtained by over-focusing the objective lens. Conversely, $\Delta_z < 0$ means under-focusing. No magnetic contrast is formed under in-focus condition. The regions with enhanced and reduced intensities are direct images of domain walls. In Foucault mode, however, the sample is observed

under in-focus condition, while an aperture is inserted to select one diffraction spot in the back focal plane. The image projected to the camera only contains intensities resulting from that particular diffraction spot. Thus, image is formed showing magnetic domains with one spin orientation. In reality, Fresnel mode is more widely used due to the ease of implementation. Further advanced operation modes include differential phase contrast (DPC) and electron holography (EH). However, since these techniques were not used in this thesis work, they are not elaborated further.

2.3.3 Analytical formalism of LTEM imaging

A quantum mechanical approach is required to fully quantify the detected image in a TEM. A plane wave can model the incoming electron beam travelling down the column of the microscope:

$$\psi_{in}(\boldsymbol{r}) = Ce^{i\boldsymbol{p}\cdot\boldsymbol{r}} \tag{2.29}$$

where C is the isotropic amplitude of the wavefunction with a momentum $\boldsymbol{p}$. Assuming weak phase object approximation, where electrons are scattered elastically by a thin sample, the electron wave exiting the sample is given by the object wavefunction:

$$\psi_{obj}(\boldsymbol{r}) = C(\boldsymbol{r})e^{i\phi(\boldsymbol{r})+i\boldsymbol{p}\cdot\boldsymbol{r}} \tag{2.30}$$

where $\phi(\boldsymbol{r})$ is the phase shift introduced by scattering from the sample, and the amplitude $C(\boldsymbol{r})$ becomes position dependent. In the case of magnetic imaging, this phase shift is due to the internal magnetic induction $\boldsymbol{B}$ and electric field $\boldsymbol{E}$. This is described by the Aharonov-Bohm effect:

$$\phi(x,y) = \frac{\pi\gamma}{\lambda U}\int V(x,y,z)ds - \frac{e}{\hbar}\oint \boldsymbol{A}(x,y,z)\cdot d\boldsymbol{s} \tag{2.31}$$

where λ is the relativistic wavelength, γ is the Lorentz factor and U is the accelerating voltage. Equation (2.31) contains two terms contributed by electric potential $V(x, y, z)$ and magnetic potential $\boldsymbol{A}(x, y, z)$. As the electron beam propagates through a magnetic sample, the sample information is contained in this phase shift.

The propagation of the exit wave through the TEM column can be modeled by the image forming process of the objective lens. The diffraction pattern formed at the back focal plane is given by the Fourier transform of the object electron wavefunction (Abbye's Lens Approximation):

$$\psi_{obj}(\boldsymbol{k}) = \int C(\boldsymbol{r})e^{i\phi(\boldsymbol{r})}e^{(2\pi i\boldsymbol{k}\cdot\boldsymbol{r})}\,d\boldsymbol{r}^3 \quad . \tag{2.32}$$

When it comes to the image formation, the exit wavefunction is mixed by the aberrations of the objective lens, including defocus, spherical aberration etc., which are all characterized by a transfer function $T(\boldsymbol{k})$. In the back focal plane, the diffraction wave function is given by the multiplication between the object electron wavefunction and the transfer function; and the image wavefunction located at the first image plane is the inverse Fourier transform of the diffraction wavefunction:

$$\psi_{im}(\boldsymbol{r}) = F^{-1}\{\psi_{obj}(\boldsymbol{k})T(\boldsymbol{k})\} \tag{2.33}$$

The general form of the transfer function can be characterized by:

$$T(\boldsymbol{k}) = B(\boldsymbol{k})\exp(i\chi(\boldsymbol{k}))\exp(-g(\boldsymbol{k})) \tag{2.34}$$

where $B(\boldsymbol{k})$ is an exponential pre-factor describing the effect of apertures that cut the electron beam width. $g(\boldsymbol{k})$ is the damping factor accounting for microscope instabilities and electron incoherence. The phase shift

introduced to the electron wavefunction caused by the objective lens is captured by the $\chi(\boldsymbol{k})$ term called phase contrast function, expressed by:

$$\chi(\boldsymbol{k}) = \frac{2\pi}{\lambda}\left[\frac{C_S}{4}\lambda^4 k^4 + \frac{\Delta_z}{2}\lambda^2 k^2 - \frac{C_A}{2}\lambda^2(k_y{}^2 - k_x{}^2)\right] \tag{2.35}$$

where C_S and C_A are the spherical aberration coefficient and astigmatism coefficient, respectively.

Finally, after being magnified by projective lenses, the intensity of the image recorded by the camera is the square modulus of the image wavefunction:

$$I(\boldsymbol{r}) = \psi_{im}(\boldsymbol{r}) \cdot \psi_{im}{}^{*}(\boldsymbol{r}) \tag{2.36}$$

To sum up, the intensity on the detector plane is the convolution of the sample exit wavefunction and the microscope transfer function. The TEM imaging analysis requires the extraction of the phase shift from the intensity recorded by the camera. The strategy is to tune the microscope transfer function (usually defocus) so that the image wavefunction modulates in intensity, thus the phase shift can be deduced from the fringes. This process is done by transfer of intensity equation, and the details are shown in the next section. For a thin magnetic sample positioned in the *x-y* plane, the local magnetic induction can be deduced from the phase shift using the following relation:

$$B_x = \frac{\hbar}{et}\frac{\partial\nabla\phi}{\partial y}, B_y = \frac{\hbar}{et}\frac{\partial\nabla\phi}{\partial x} \tag{2.37}$$

where Gauss' Law has been applied: $div\ \mathbf{B} = 0$; t is sample thickness. Therefore, together with many other TEM imaging techniques such as high resolution transmission electron microscopy (HRTEM), LTEM is also a phase contrast imaging technique. The method of tuning the microscope transfer function in LTEM is mainly done by introducing a defocus, namely, the Fresnel mode operation, since defocus is the most convenient to implement, model and quantify. However, in HRTEM only a small defocus is applied; hence the advanced TEM setting with corrected spherical aberration is usually required.

2.4 Introduction to modelling techniques

For neutron scattering in reciprocal space and LTEM imaging in real space studies, modelling is indispensable to obtain physical interpretation from the results. This section briefly introduces three modelling methods that are most relevant to this thesis work: linear spin-wave theory, micromagnetic simulation and transport of intensity equation (TIE).

2.4.1 Linear spin wave theory

Localized spins in a magnetic material may interact with each other through various magnetic interactions, most dominantly the Heisenberg exchange interaction, and often the Dzyaloshinskii-Moriya interaction (DMI). A spin wave is defined as the collective spin-precessional motion upon excitation. In quantum mechanics, the quanta of spin waves are called magnons according to particle-wave duality. Since the inelastic neutron scattering technique allows us to measure the dispersion relation of magnons, one can extract the magnitude of magnetic interactions in specific materials by fitting the experimental data with an appropriate model. This process is essential in constructing the spin Hamiltonian of a material, and the linear spin wave theory is a standard tool for analyzing magnetic dispersions measured by neutron spectroscopy. In recent years, software packages allowing the routine calculation of spin wave spectra according to this theory are widely available, including the SpinW software package [55] implemented in this thesis.

In a semi-classical model, the linear spin-wave theory computes the magnon spectrum by assuming a small deviation in the spin orientation from their respectively equilibrium positions (spin aligned along **z**-axis):

$$S^z(n) = -\sqrt{1 - \sum_{\alpha=x,y}\left(S^\alpha(n)\right)^2} \simeq -1 + \tfrac{1}{2}\sum_{\alpha=x,y}\left(S^\alpha(n)\right)^2$$

with the hypothesis $\left(S^\alpha(n)\right)^2 \ll \left(S^z(n)\right)^2$ (2.38)

where α denotes the x and y transverse spin component. The theory breaks down when the hypothesis in Equation (2.38) fails to hold. Non-linear spin wave regime corresponds to large fluctuations of spins from equilibrium, and such excitations are known as spin wave chaos [56]. It is noted that the validity of the linear spin wave theory becomes increasingly compromised for low spin systems, in particular for spin ½ systems with significant quantum fluctuations.

Here, we consider a quantum spin model, with the z-axis being the quantization axis. The general spin Hamiltonian reads:

$$H = \sum_{i,d} J(d)\boldsymbol{S_i S_{i+d}}$$

(2.39)

where J is the magnitude of exchange interaction between two neighboring spins separated by a distance d. The quantum spin state is denoted by $|n\rangle$, and ladder operators are denoted by S^- and S^+:

$$S^-|n\rangle = \sqrt{2S}\sqrt{1 - \tfrac{n}{2S}}\sqrt{n+1}|n+1\rangle \quad S^+|n\rangle = \sqrt{2S}\sqrt{1 - \tfrac{n-1}{2S}}\sqrt{n}|n-1\rangle \;.$$

(2.40)

By performing second quantization, we introduce the creation operator a^+ and annihilation operator a:

$$a^+|n\rangle = \sqrt{n+1}\,|n+1\rangle \qquad a|n\rangle = \sqrt{n}\,|n-1\rangle$$

(2.41)

The ladder operators and creation/annihilation operators are related by Holstein-Primakoff transformation:

$$S^- = \sqrt{2S}\,a^+\sqrt{1 - \tfrac{\langle a^+a\rangle}{2S}} \qquad S^+ = \sqrt{2S}\,a\sqrt{1 - \tfrac{\langle a^+a\rangle}{2S}}$$

(2.42)

In this quantum mechanical model, linear spin wave theory assumes that the expectation value of magnon number, defined by $\langle a^+a\rangle$, is much smaller than the spin length S. Then Equation (2.42) reduces to:

$$S^- = \sqrt{2S}\,a^+ \qquad S^+ = \sqrt{2S}\,a$$

(2.43)

Therefore, the system of N spins can be effectively modelled as a system of N coupled harmonic oscillators. By substitution of Equation (2.43) into Equation (2.39), the magnon dispersion up to the first order can be written as:

$$E = S^2 \sum_{i,d} J(\boldsymbol{d})\cos(\boldsymbol{q}\cdot\boldsymbol{d}) + S^{3/2}\sum_{i,j}\tfrac{i}{2}J(\boldsymbol{d_{ij}})\sin(\boldsymbol{q}\cdot\boldsymbol{d_{ij}})\left(a_i^+ - a_i + a_j - a_j^+\right) \;. \quad (2.44)$$

The expression of higher-order terms are more complex, which require performing diagonalization in order to separate operator mixing on different spin sites. Furthermore, the spin-spin correlation function can be obtained through the diagonalization of the second-order term in the expansion. For the Heisenberg model, the linear excitations associated with the quadratic Hamiltonian are spin waves with dispersion relation given by Equation (2.44).

2.4.2 Micromagnetic simulation

Micromagnetics is a widely used tool to predict the magnetic ground state spin configuration at a sub-micrometer length scale. The spins are modelled as collective spins produced by a group of atoms at this length scale. It is a convenient tool since the detailed atomic structure is ignored, while it is sufficient to capture of nature of magnetic structures. The spins are modelled as classical spins which can vary their orientations smoothly under continuum approximation. The simulation program is available in a number of software packages, such as OOMMF [57] and Mumax [58].

Micromagnetics deals with both static equilibrium and dynamic problems. The magnetic interaction terms are expressed in the continuum limit, and the magnetic ground state is obtained by minimizing the magnetic energy. After the ground state is determined, the dynamical behaviors can be simulated by solving the time-dependent Landau-Lifshitz-Gilbert Equation.

The total magnetic energy consists of various terms in micromagnetics:

$$E_{mag} = E_{ex} + E_{DMI} + E_{anis} + E_Z + E_{demag} + E_{me} \tag{2.45}$$

which are exchange interaction, DMI, anisotropy energy, Zeeman energy, demagnetization energy and magnetoelastic energy, respectively. All these energy terms are expressed in the continuum limit, for instance, the exchange energy has the form:

$$E_{ex} = A \int ((\nabla m_x)^2 + (\nabla m_y)^2 + (\nabla m_z)^2) dV \tag{2.46}$$

where A is the averaged exchange energy between neighboring macro-spins across the sample; m_x, m_y, m_z are the components of the magnetization vector produced by the spin. Usually, one only focuses on the direction of the magnetization vector so a unit vector is usually inserted |**m**|=1.

2.4.3 Transport of intensity equation

In the field of magnetic imaging based on LTEM, the transport of intensity equation (TIE) provides a simple formalism that allows us to extract the phase shift from the intensity pattern recorded by the camera. There are several commercial software packages that implement TIE [59]. The magnitude and direction of the magnetic induction vectors (**B**) are also calculated. In Fresnel mode, because the magnetic contrast is mainly produced by the defocus term in the microscope transfer function shown in Equation (2.34), the image wavefunction, up to the first order in defocus Δ_z, can be written as:

$$\psi_{im}(\boldsymbol{r}) = F^{-1}\{\psi_{obj}(\boldsymbol{k})e^{i\pi\Delta_z\lambda k^2}\} \tag{2.47}$$

here we have assumed an ideal microscope where the aperture and damping effects can be neglected. By performing Taylor expansion to the transfer function, we can obtain:

$$\psi_{im}(\boldsymbol{r}) = \psi_{obj}(\boldsymbol{r}) - i\pi\Delta_z\lambda F^{-1}\{k^2 F\{\psi_{obj}(\boldsymbol{r})\}\} \tag{2.48}$$

where $\psi_{obj}(\boldsymbol{r})$ is given by Equation (2.32). By substituting $\psi_{obj}(\boldsymbol{r})$ into the above Equation and applying the chain rule, the second term becomes:

$$F^{-1}\{k^2 F(ae^{i\phi(r)})\} = \frac{-1}{4\pi^2}\nabla^2[ae^{i\phi(r)}] \tag{2.49}$$

where the amplitude of the object electron wavefunction is replaced by a for simplicity. Equation (2.48) and (2.48) imply that for a small defocus, the LTEM image is formed by the interference between the object wave

40

and a plane wave modulated by defocus. Taking the modulus square of Equation (2.48) and truncation at first order in defocus, we obtain the intensity pattern:

$$I(x, y, \Delta_z) = a^2 - \frac{\Delta_z \lambda}{2\pi} \nabla \cdot (a^2 \nabla \phi(x, y)) \quad . \tag{2.50}$$

In applications, three images are usually acquired: one at zero defocus (in focus) $\Delta_z = 0$, one at over-focus Δ_z and one at under-focus $-\Delta_z$ with equal distance. When the microscope is operated in focus, the intensity pattern is the square of the amplitude in the object electron wave:

$$I(x, y, 0) = a^2. \tag{2.51}$$

Therefore, equation (2.50) can be expressed as:

$$-\frac{2\pi}{\lambda} \frac{\partial I(x,y,\Delta_z)}{\partial \Delta_z} \Big|_{\Delta_z \to 0} = \nabla \cdot [I(x, y, 0) \nabla \phi(x, y)] \tag{2.52}$$

by taking the limit $\Delta_z \to 0$. Equation (2.52) is the standard form of TIE, which shows that the first-order derivative of the intensity map with respect to defocus is equal to the gradient of phase shift caused by the sample. Fig. 2.15 shows an example of an LTEM image and the corresponding spin configuration obtained by TIE [59]. The sample is FeGe, one of the Bloch-type skyrmion lattice hosting systems, and the whirl-like spin configuration can be clearly resolved.

(a) (b)
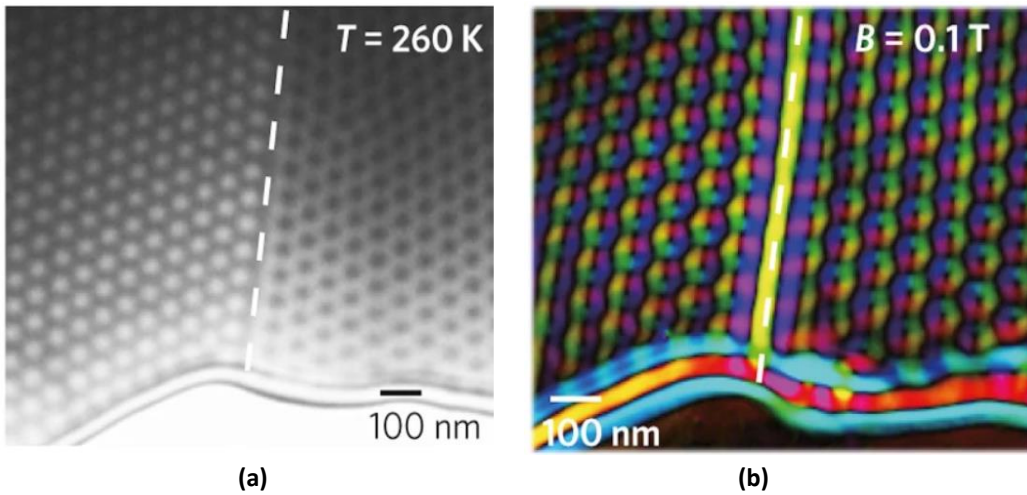
Fig. 2.15: (a) LTEM image of FeGe in the skyrmion phase; (b) spin configuration obtained from TIE analysis, where the in-plane magnetization is color-coded. A grain boundary is marked by a dashed line. Image reproduced from Ref. [60].

Chapter Three: Results – part one: neutron scattering studies of the skyrmion hosting polar magnet $VOSe_2O_5$

In this chapter, we present the experimental details and main results of scattering experiments on the polar magnet $VOSe_2O_5$ which hosts Néel-type skyrmion lattice. We start with an introduction to the motivations of studying this material, followed by details of the sample growth, crystal structure, bulk characterization, and several supplementary studies such as SANS and x-rays. The main results are obtained from inelastic neutron scattering and they are presented in section 3.4. The final section focuses on the interpretation of results, and further gives a summary and outlook.

3.1 Introduction to $VOSe_2O_5$ and research motivation

Since the first skyrmion lattice was experimentally observed in MnSi in 2009 [29], various Bloch-type hosting systems have been found, including metallic FeGe [60], insulating Cu_2OSeO_3 [61], semiconducting $Fe_{1-x}Co_xSi$ [30]. These systems are non-centrosymmetric cubic compounds (space group $P2_13$) with chiral symmetry. The other famous family of Bloch-type skyrmion lattice hosting systems are β-Mn-type Co-Zn-Mn alloys with a different chiral cubic space group $P4_132$ or $P4_332$ [31]. Through theoretical and experimental work, the mechanism to stabilize Bloch-type skyrmion lattice in these systems is well understood, which involves delicate balance amongst exchange interaction, DMI, Zeeman energy, and also thermal fluctuations slightly below Curie temperature [24]. Due to the feasibility of accessing materials, the primary amount of research concerning the practical applications of skyrmion lattice has been using Bloch-type.

Néel-type skyrmions are most commonly observed in synthetic magnetic multilayer systems where the inversion symmetry is broken at interfaces, and skyrmions are formed individually [21]. However, bulk crystals hosting Néel-type skyrmions in a lattice form are rare. As a consequence, the other type of skyrmion lattice, Néel-type, has been much less studied from both a fundamental level and the view point of applications in bulk materials. The main challenge that hinders the research in this field is the lack of known hosting systems. The first hosting system was discovered in 2015 in a rhombohedral magnetic semiconductor GaV_4S_8 with polar symmetry and easy-axis anisotropy along the polar [1 1 1] direction [8]. There are several additional compounds belonging to this family, for example GaV_4Se_8 [62]. A second known hosting system is $VOSe_2O_5$, a tetragonal polar magnet with space group $P4cc$, discovered in 2017 [26]. Until present, the research of Néel-type skyrmion lattice in the bulk has been largely limited to a phenomenological level [8, 26, 62]. The competition among the magnetic interactions, and the stabilization mechanism are not fully understood on a fundamental level yet. Therefore, the main motivation to study $VOSe_2O_5$ in this thesis work is to address the microscopic magnetic interactions present in this system through a combination of experimental, computational and modelling techniques.

In this context, the theory community recently started to consider quantum chemistry calculation as a means to compute magnetic interactions in skyrmion hosting materials and predict new hosting systems. Compared with conventional density function theory (DFT), quantum chemistry focuses on magnetic properties of local clusters. In principle, this allows us to accurately calculate magnetic interactions at a microscopic level, understand the competition amongst these interactions, and eventually, learn if a region of skyrmion lattice stability exists in the phase diagram described by the interaction scheme. Therefore, the further motivation to study $VOSe_2O_5$ here is to provide feedback for quantum chemistry calculations done in parallel with the present experimental work. In this thesis, we take the first step towards this broader, longer-term goal of integrating computational techniques as a novel tool with which one can predict further skyrmion lattice hosting systems, thus opening the possibility to use Néel-type skyrmion lattice in bulk systems as the alternative option in practical spin wave applications.

3.2 Sample information and characterization

In this section, we provide a brief introduction to the crystal growth, and important aspects of the crystal structure and related magnetic structure. The results of magnetic property characterization are also shown, which are essential to understand neutron scattering results presented in later sections.

3.2.1 Single crystal growth

There are two sources of sample providers during this thesis work. One is from the group of Prof. Yoshinori Tokura at RIKEN, Japan, and samples were only used in x-ray studies; the main source is the Crystal Growth Facility, Institute of Physics, EPFL, contributed by Dr. Arnaud Magrez and Mr. Priya Baral, used in all neutron studies.

At EPFL, single crystals of $VOSe_2O_5$ were grown in two steps. Firstly, a thoroughly homogenized stoichiometric mixture of VO_2 (Sigma Aldrich) and SeO_2 (also Sigma Aldrich) was enclosed in a quartz ampoule, and placed inside a muffle furnace. The temperature of the furnace was slowly raised to $450\,^\circ C$ over a period of 8 hours and then held at constant temperature for two weeks. After cooling down to room temperature, olive green $VOSe_2O_5$ polycrystalline powder was found to be formed. Phase purity was checked using a powder x-ray diffractometer. In the second step, this polycrystalline sample was used as the precursor for growing $VOSe_2O_5$ bulk single crystals via the chemical vapor transport (CVT) technique. About 2 grams of pure phase $VOSe_2O_5$ polycrystalline powder was enclosed in a quartz tube together with 100 mg of VCl_3 (Sigma Aldrich) powder. High reactivity and volatility of VCl_3 make it an excellent transport agent. The sealed ampoule was then placed inside a two-zone furnace. The source and sink of the ampoule were kept at $485\,^\circ C$ and $420\,^\circ C$, respectively. The transport reaction took place over a period of 7-8 weeks. After this, the furnace was slowly cooled down to room temperature.

Fig. 3.1 (a) shows a photo of quartz ampoule after cooling. Furthermore, post-growth annealing treatment was performed at $400\,^\circ C$ for 12 hours, under a constant flow of nitrogen gas. An example of a plate-shape single crystal is provided in Fig. 3.1 (b), where the c-axis is perpendicular to the plane of the plate. The grid size is 1 mm, so the typical crystal size and morphology can be seen. The single crystal can also be grown with needle shape where the c-axis is along the long axis, using a different transport agent NH_4Cl. The magnetic phase diagram of $VOSe_2O_5$ when the external magnetic field is applied along the c-axis is introduced again in Fig. 3.1 (c) for the convenience of referencing in upcoming sections. The notations and properties of magnetic phases were discussed in Section 1.2.

| (a) | (b) | (c) |
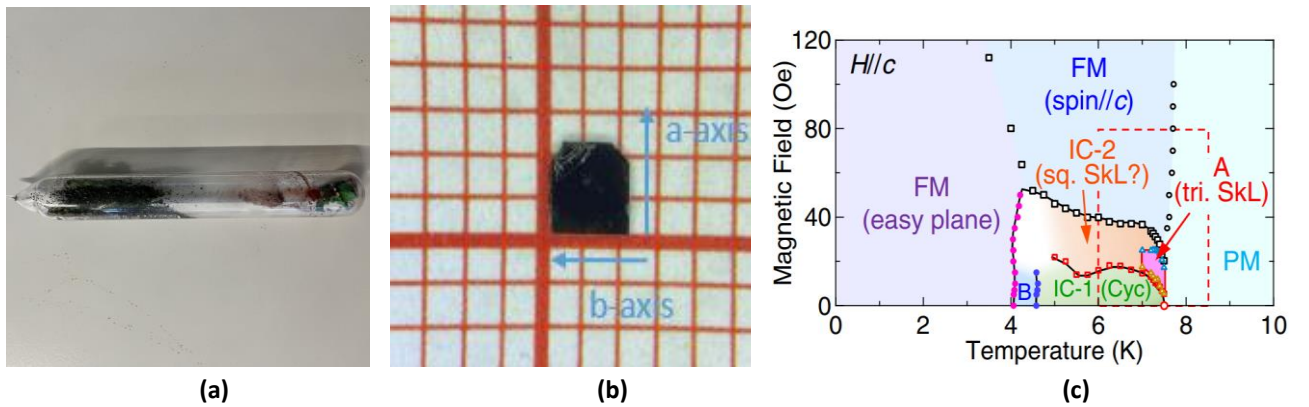
Fig. 3.1: (a) Photo of the sealed ampoule after taken out from the furnace; (b) photo of a plate-shape single crystal grown at EPFL; (c) magnetic phase diagram of $VOSe_2O_5$ for H//c, reproduced from Ref. [26].

3.2.2 Crystal structure and exchange interactions

The crystal structure of $VOSe_2O_5$ consists of three independent chains of corner-shared VO_6 octahedral parallel to the c-axis (also called polar axis), where V^{4+} ions are hybridized with neighboring oxygen ligands. The view along the c-axis of the crystal structure is shown in Fig. 3.2 (a). The three chains are labelled by V(1), V(2) and V(3) and are aligned with the corners, body-center and edges of the unit cell, respectively. There are eight vanadium atoms in the unit cell, and the VO_6 chains are connected by Se_2O_5 groups parallel to the a-axis and b-axis, as seen in Fig. 3.2 (b) (the a-axis and b-axis are equivalent according to the tetragonal symmetry). It is noted that the V(3) chain contains twice as many magnetic sites as the other two chains due to occupancy. The lattice parameters at 10 K are: a = b = 11.1957(1) Å, c = 7.8161(2) Å, verified by both previous literature [23] and single crystal neutron diffraction experiment as part of this thesis work.

The most profound feature in the crystal structure of $VOSe_2O_5$ is that the VO_6 octahedral are distorted since the V^{4+} ions are shifted along the c-axis by a small amount Δd_z from their respective octahedral centers, as indicated in Fig. 3.2 (c). Therefore, for each V^{4+} ion, there are one short and one long axial V-O bonds, in addition to four equivalent V-O equatorial bonds. This unequal displacement of V^{4+} ions is the origin of broken inversion symmetry, making $VOSe_2O_5$ a polar material. It also leads to a spontaneous electric polarization along the c-axis [23]. Despite the fact that $VOSe_2O_5$ is polar, the system is not believed to be ferroelectric because polarization reversal in the presence of an external electric field has not been demonstrated.
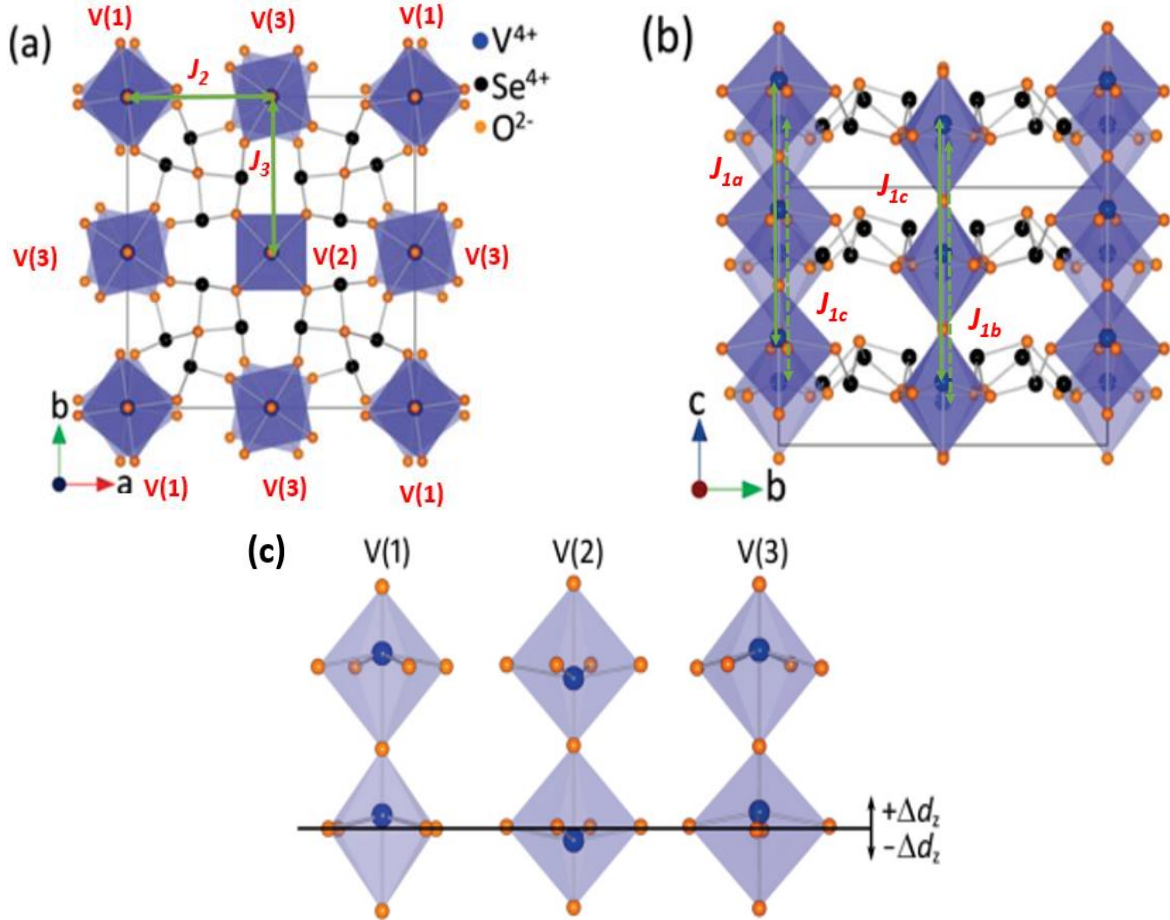
Fig. 3.2: (a) Crystal structure of $VOSe_2O_5$ viewed along the c-axis. Three different types of VO_6 chains and their positions are denoted by V(1), V(2) and V(3) respectively; (b) view along the a-axis where the Se_2O_5 groups connecting VO_6 chains are seen; the exchange interactions are denoted by green arrows; (c) details of individual chains showing the V^{4+} ions are off-center. Δd_z indicates the displacement of V^{4+} ions from the octahedral centers, and a solid line denotes equatorial planes for reference. Images modified from Ref. [23].

Further, it is essential to point out that the adjacent octahedral along V(1) chains and V(3) chains are mutually rotated around the c-axis, whereas the octahedral along V(2) chains display no such rotation around the c-axis. This difference is visualized in Fig. 3.2 (a). It affects the orbital distributions of V^{4+} ions with respect to oxygen ligands, thus the magnitude of exchange interactions. This results in three different types of exchange interactions along the c-axis, which are also the nearest-neighbor ones, labelled as J_{1a-c}. The effects of such feature become clear in section 3.4 after these exchange interactions are determined from inelastic neutron scattering experiments.

In the determination of the spin Hamiltonian for $VOSe_2O_5$, the following exchange interactions among magnetic V^{4+} ions are considered, ordered by distance: intra-chain interactions J_{1a}, J_{1b} and J_{1c}, along V(1), V(2) and V(3) chains, respectively; mainly in-plane inter-chain interaction J_2 connecting V(1) and V(3); inter-chain interaction J_3 connecting V(2) and V(3). These exchange interactions are expected to be calculable by quantum chemistry in a reasonable amount of time and with reasonable accuracy. In addition, simulations suggest that further nearest-neighbor interactions beyond J_3 are negligible, and thus in the resulting model, exchange interactions up to the third nearest-neighbors are taken into account. The mentioned exchange interactions are partly labelled in Fig. 3.2 (a) and (b). The details of orbital distributions for each exchange interaction are presented in section 3.4.

3.2.3 Macroscopic magnetic measurements

The bulk magnetic properties of single crystals grown at EPFL were characterized by DC magnetization and AC susceptibility measurements. A standard, commercial Quantum Design MPMS magnetometer was used for both measurements. The experimental work was done in collaboration with Mr. Priya Baral, Institute of Physics, EPFL.

Fig. 3.3 shows magnetization versus magnetic field at base temperature 2 K for a needle-shape single crystal, a = b = 0.5 mm, c = 1.5 mm. The external magnetic field is applied along the c-axis and a-axis in separate experiments for comparison. The sample's magnetic state is stabilized at around 150 Oe in both field orientations, and the magnetization at this plateau is approximately identical (0.013 emu) in both directions. However, the slope of magnetization against magnetic field at low field is steeper when the field is applied parallel to the a-axis.

To determine the magnetic moment per V^{4+} ion at this plateau where the magnetization becomes stable, the following formula was applied:

$$\mu = \frac{M_s Z}{5585.7 * m} = 0.482 \; \mu_B / f.u \tag{3.1}$$

where μ is the magnetic moment per formula unit, M_s is the magnetization in emu unit, 5585.7 is the conversion factor from emu to S.I. unit A/m, m is the mass of the crystal which is 1.7 mg, and Z = 305 is the atomic mass of $VOSe_2O_5$. The result of 0.482 μ_B per formula unit is consistent with previous measurement [22], given the d^1 electronic configuration of V^{4+} ion with **S** = ½, **L** = 1 and 3-up 1-down ferrimagnetic spin configuration. It is noted that the energy scale corresponding to the magnetic field (between 150 Oe and 400 Oe) is much smaller than the dominant exchange interaction in this system, to be presented in later sections. Therefore, at this magnetic field it is insufficient to polarize spins into the saturated ferromagnetic state.

(a)   **(b)**
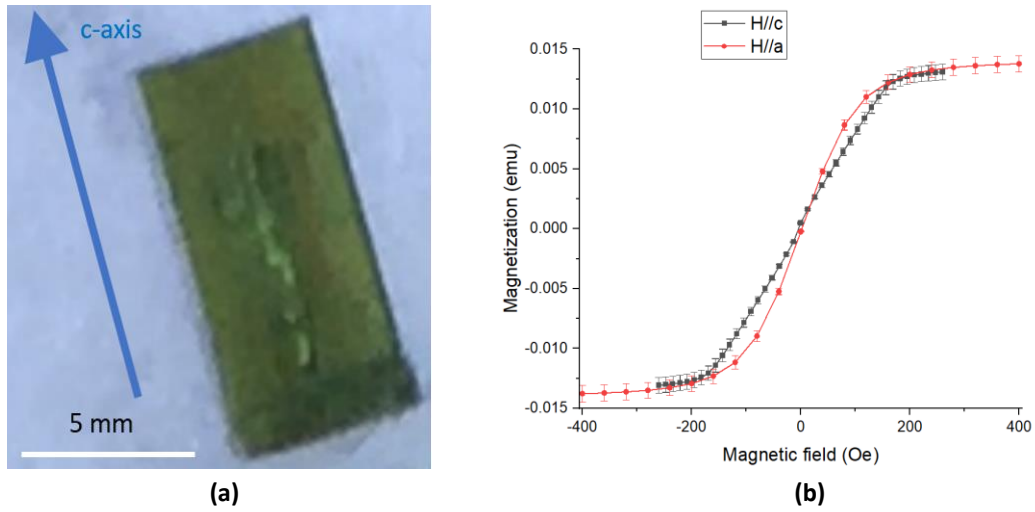
Fig. 3.3: (a) Photo of needle-shape VOSe₂O₅ single crystal grown at EPFL; (b) bulk magnetization versus magnetic field measurement at 2 K, for magnetic field along the c-axis and a-axis. The magnetization is corrected by sample shape for both field orientations.

The magnetic phases, in particular the skyrmion phase in VOSe$_2$O$_5$ were characterized by AC susceptibility in temperature and field scans. The frequency of the AC magnetic field was 1 kHz and the amplitude was 1 Oe. The results are presented in Fig. 3.4. The peak at 7.5 K in both real and imaginary parts of the temperature dependent susceptibility denotes the magnetic phase transition across Curie temperature (Fig. 3.4, left hand panels). The skyrmion phase can be identified in the imaginary part of 7.4 K post-annealing data (Fig. 3.4, bottom right panel). It resides in a tiny region between the small peak near 15 Oe and the large peak near 25 Oe. The second large peak at higher magnetic field around 80 Oe corresponds to the phase boundary between IC-2 phase and saturated ferromagnetic phase. The Curie temperature of crystals grown at EPFL is as expected according to the phase diagram reported in previous literature [26].
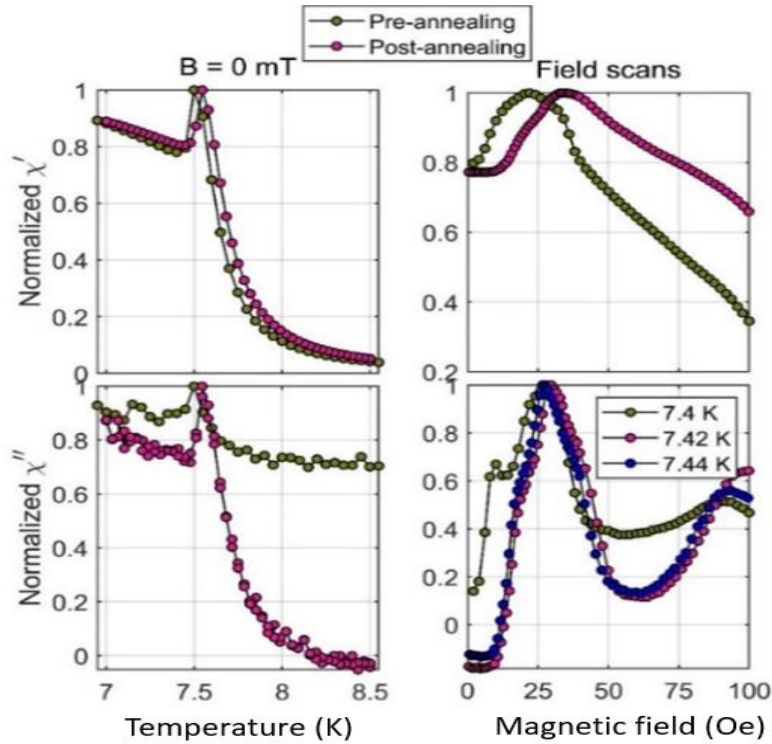
Fig. 3.4: The real and imaginary parts of the temperature and field-dependent AC susceptibility obtained on a VOSe₂O₅ single crystal grown at EPFL. Results before and after annealing are compared.

The data acquired before and after crystal annealing are also compared in Fig. 3.4. The peaks denoting the skyrmion phase move to slightly higher field after annealing, and manifest as a weak feature of the large peak spanning roughly 15 Oe to 25 Oe. These data indicate the skyrmion phase co-exist with another phase, likely one of the surrounding IC-1 and IC-2 spiral phases. Further attempts at crystal annealing did not yield any further particular noticeable improvement according to the bulk measurements (data not shown).

3.3 Diffraction studies

This section contains results obtained from three diffraction experiments on $VOSe_2O_5$ during this thesis work: resonant x-ray scattering, SANS and wide-angle neutron diffraction. Though some aspects of x-ray and SANS experiments did not result in specific new insights, the wide-angle neutron diffraction results are important for the inelastic neutron scattering results which are presented in the next section.

3.3.1 Resonant x-ray scattering

The first beamline experiment on $VOSe_2O_5$ was resonant elastic x-ray scattering (REXS) performed at the VEKMAG beamline, BESSY, Germany. This beamline allows the application of an external magnetic field along any direction in 3D space. A 200 nm thick lamella was prepared by focused ion beam (FIB) at PSI, shown in Fig. 3.5 (c) (the crystal was provided by the group of Prof. Yoshinori Tokura at RIKEN, Japan). At base temperature 2.5 K, the absorption spectrum and x-ray magnetic circular dichroism (XMCD) spectrum were measured, and they are plotted in Fig. 3.5 (a) and (b), respectively. These signals indicate the presence of magnetic V^{4+} ions at base temperature. The XMCD spectrum was obtained by subtraction of absorption spectrums at positive (0.5 T) and negative magnetic field (-0.5 T), each of which saturates the sample to the forced ferromagnetic state. The measured resonant energies at vanadium L3 (517.2 eV) and L2 (523.6 eV) edges agree with the reference spectrum of V^{4+} ion reported in the literature [63]. In addition, a strong signal of the oxygen K-edge at higher energy was detected. Usually, dichroism at oxygen K-edge is not expected in transition metal oxides, however, the fact that a considerable XMCD signal is observed here implies the presence of significant hybridization between V^{4+} ions and neighboring oxygen ligands. The hybridization effect in vanadium oxides VO_X is also reported in previous literature [64], which states that unoccupied oxygen 2p orbitals hybridize with vanadium 3d or 4sp orbitals. The hybridization present in $VOSe_2O_5$ may be the source of magnetic anisotropy discussed in later sections.

In scattering mode where the x-ray beam energy was tuned to the vanadium L3 edge, no Bragg spots signifying long-range incommensurate spiral magnetic order were measured in the 2D scattering pattern. Fig. 3.5 (d) shows one of CCD detector images at 6 K and zero magnetic field, where the sample is expected to be in the IC-1 cycloidal phase. According to previous study, the cycloidal wavevector is determined to be q=0.046 nm^{-1} [26], which lies within the field-of-view of the CCD detector.

For systems hosting Bloch-type skyrmion lattices, it was reported previously that helices and skyrmion lattices can exist in a thin crystal as long as the sample thickness is greater than the pitch length of skyrmion lattice [60]. The pocket of skyrmion phase in the phase diagram can even extend to lower temperature in thinner samples, due to a growing instability of the competing conical phase for which the propagation vector points along the external magnetic field [60]. However, the analogy for Néel-type skyrmion lattice was not found in this experiment on a $VOSe_2O_5$ lamella. Taken at face value, the properties of magnetic phases in this system vary more drastically between bulk crystals and thin samples, and further investigation is needed to understand this difference from a fundamental level. In the following sections, neutron are used as a probe for focusing on bulk sample properties.
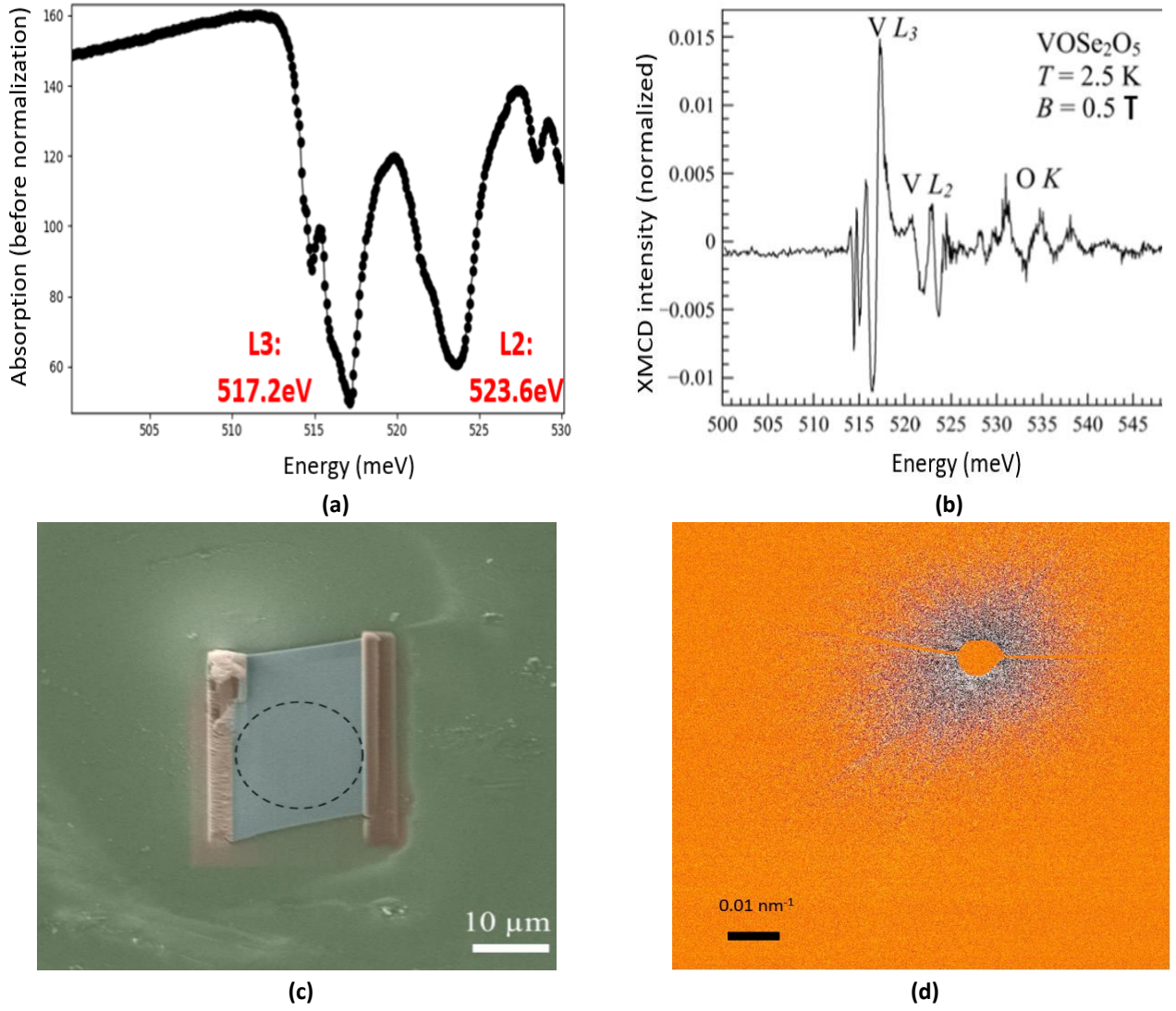
Fig. 3.5: (a) Absorption spectrum at 2.5 K showing the L3 and L2 absorption edges of V^{4+} ions; (b) XMCD spectrum at 2.5 K showing both vanadium edges and oxygen K edge; (c) a 200 nm thick $VOSe_2O_5$ FIB lamella placed onto the Si_3N_4 membrane; dotted circle indicates the hole drilled on membrane; (d) the CCD camera view of the scattering pattern at 6 K where no Bragg spots are found.

3.3.2 SANS and bulk electrical measurements

Multiple SANS experiments were performed during this thesis work, mainly at the SANS-I beamline, PSI and also the D33 beamline, ILL. The magnetic phases of $VOSe_2O_5$ were characterized and found to be consistent with previous work [26]. In this thesis we also made particular attempts to apply electric fields, aiming to demonstrate control over the skyrmion phase through the magnetoelectric (ME) coupling expected to be endowed on its magnetic spin texture by the polar lattice symmetry. The crystals studied had a plate-like shape and was provided by Dr. Arnaud Magrez and Mr. Priya Baral, the Institute of Physics, EPFL.

At 7.35 K and zero magnetic field in the IC-1 phase, the SANS pattern in Fig. 3.6 (a) contains four spots which indicate two cycloidal domains with equal modulation length of 0.052 nm^{-1}. In real space this corresponds to 121 nm, roughly consistent with the previous SANS measurement [26]. At D33, a skyrmion lattice pattern with six-fold symmetry at finite magnetic field was measured, shown in Fig. 3.6 (b). In the skyrmion phase, the spots at north and south poles are much stronger than other spots due to coexisting cycloidal domains. However, the SANS experiment with an external electric field at SANS-I did not indicate any effect for applied electric fields up to 3 kV/mm. The intensity or position of Bragg spots did not show any variation as the

49

external electric field was applied. This result is in contrast with the Bloch-type skyrmion lattice hosting system Cu_2OSeO_3, where previous demonstrations that an external electric field can couple to skyrmion lattice through ME coupling, and drive the sample to the neighboring phases, were reported [65].
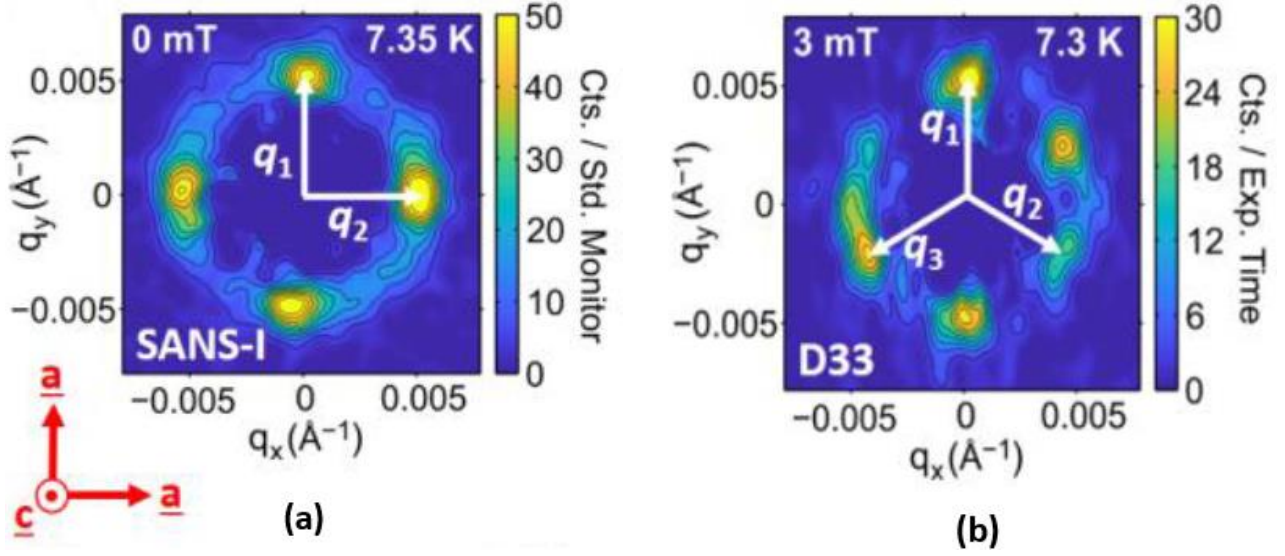
Fig. 3.6: (a) SANS pattern at 7.35 K, 0 mT, indicating cycloidal ground state; (b) SANS pattern at 7.3 K, 3 mT, revealing six-fold symmetry which indicates the presence of skyrmion lattice.

In order to investigate the ME coupling in $VOSe_2O_5$ in more detail, several bulk electric measurements were performed in collaboration with the group of Prof. Sun at Chongqing University, China. Both electric field and magnetic field were applied along the c-axis, identical to the geometry in SANS. The ME coupling constant is given by:

$$\alpha = \frac{E}{H} = \frac{V}{dH}$$

(3.2)

where E and H are the magnitude of external electric field and magnetic field, respectively, V is the voltage and d is the sample thickness. Equation (3.2) implies that the ME constant is proportional to voltage when a constant magnetic field is applied. In Fig. 3.7 (a), peaks in voltage are observed just above 8 K near the Curie temperature, and at 4.2 K, 50 Oe when transitioning between the IC-2 and FM phases. These data prove that ME coupling is indeed present in the sample, and phase transitions are observable when there are large changes in the magnetic structure. The pyroelectric current plotted in Fig. 3.7 (b) also shows a broad peak around 4.5 K. The corresponding magnetic-order-induced electric polarization is plotted in Fig. 3.7 (c). It is calculated using the following formula:

$$P = \frac{\int_0^t I dt}{S}$$

(3.3)

where S is the sample cross-section area. The polarization is the largest at base temperature. However, this is a rather weak electric polarization (maximum 2.8 $\mu C/m^2$), namely only 0.2% of the spontaneous electric polarization (around 1500 $\mu C/m^2$) produced by the polar crystal structure as measured in Ref. [23]. These results reveal that while ME coupling is indeed present, the strength of the coupling between the external electric field and the relevant magnetic order in the sample is too weak when both electric field and magnetic field are applied parallel to the c-axis. Consequently, the electric field applied in SANS experiment was insufficiently strong to provide direct control over the incommensurate magnetic structures in $VOSe_2O_5$.
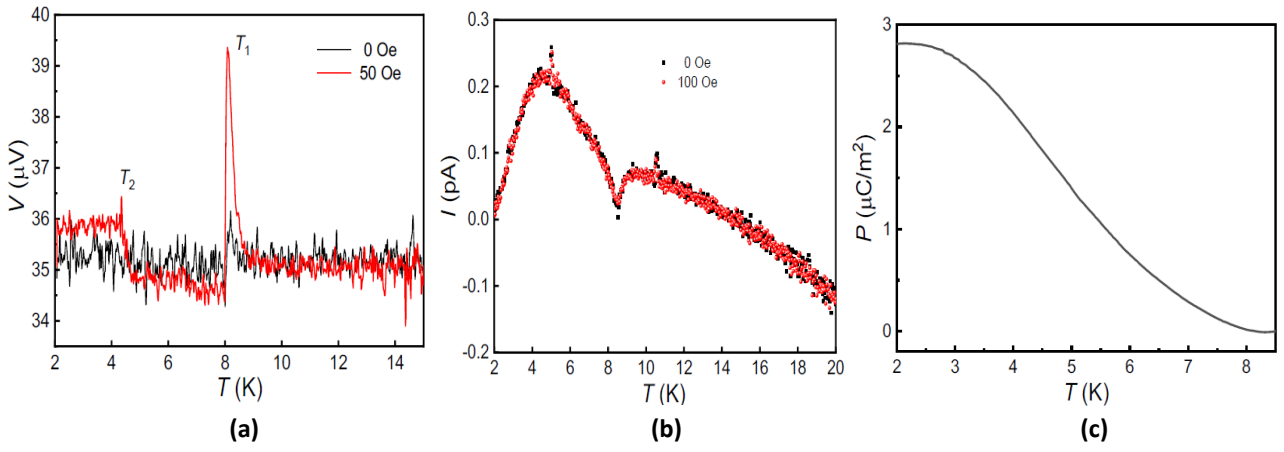
Fig. 3.7: (a) ME constant (proportional to voltage) versus temperature in VOSe$_2$O$_5$. (b) pyro-electric current and (c) magnetic-order-induced electric polarization versus temperature, suggesting weak ME effect in this system. Plots are contributed by the group of Prof. Sun at Chongqing University, China.

3.3.3 Wide-angle neutron diffraction

As discussed in section 2.4.1, the spin configuration of the magnetic ground state is an important diagnostic for the accuracy of a linear spin wave model that describes the spin Hamiltonian of a magnetic system. Therefore, a single crystal neutron diffraction experiment aiming at a direct determination of the magnetic ground state in zero field and base temperature (1.5 K) was performed at the neutron diffractometer of ZEBRA beamline, PSI. Data were collected at both 10 K and 1.5 K for the refinement of nuclear and magnetic structure. A plate-shape single crystal provided by Dr. Arnaud Magrez and Mr. Priya Baral, the Institute of Physics, EPFL, was used for this experiment.

In the experiment, a series of integrated intensities for selected Bragg peaks was measured, ranging from low index (1 0 0) to higher index (5 1 1) peaks. Fig. 3.8 (a) shows a rocking scan of the (1 0 0) peak at 1.5 K – base temperature, and 10 K – above Curie temperature. The difference in integrated intensity means that additional scattering appears below Curie temperature, implying (1 0 0) is also a magnetic Bragg peak. The magnetic scattering at base temperature is described by a general commensurate wavevector of **Q** = (0 0 0). In Fig. 3.8 (b), the hysteresis of the magnetic Bragg peak (0 1 0) intensity was measured through zero-field cooling and subsequent warming scans. The results indicate little hysteresis across the transition between the IC-1 and FM ground states around 4 K.
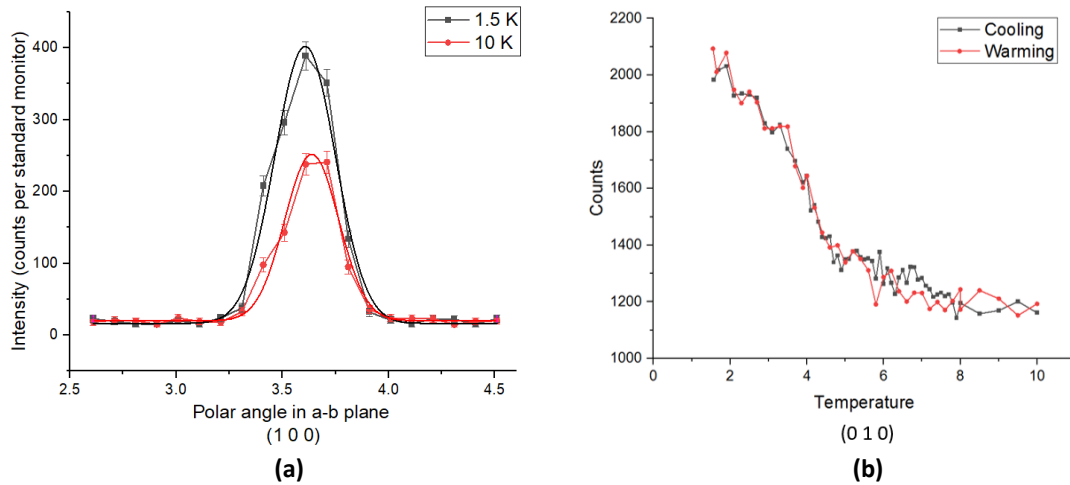
Fig. 3.8: (a) Scan over (1 0 0) Bragg peak in a-b plane at 1.5 K and 10 K. The solid lines are Gaussian fitting of integrated intensity; (b) the intensity of Bragg peak (0 1 0) versus temperature in warming and cooling scan.

The nuclear structure at 10 K was checked using the crystal structure model given by Ref. [23]. The calculated nuclear structure factor is broadly consistent with experimental data (refinement quality factor RF = 16.92), as shown in Fig. 3.9 (a). The refined lattice parameters from FullProf are: a = b = 11.2924 Å, c = 7.8499 Å, almost identical to the parameters given in Ref. [23]. Note that due to the limited dataset, the results can only be considered as consistent with the previously published crystal structure, rather than a true test of the model. For the latter, a low temperature x-ray diffraction study would be preferable.
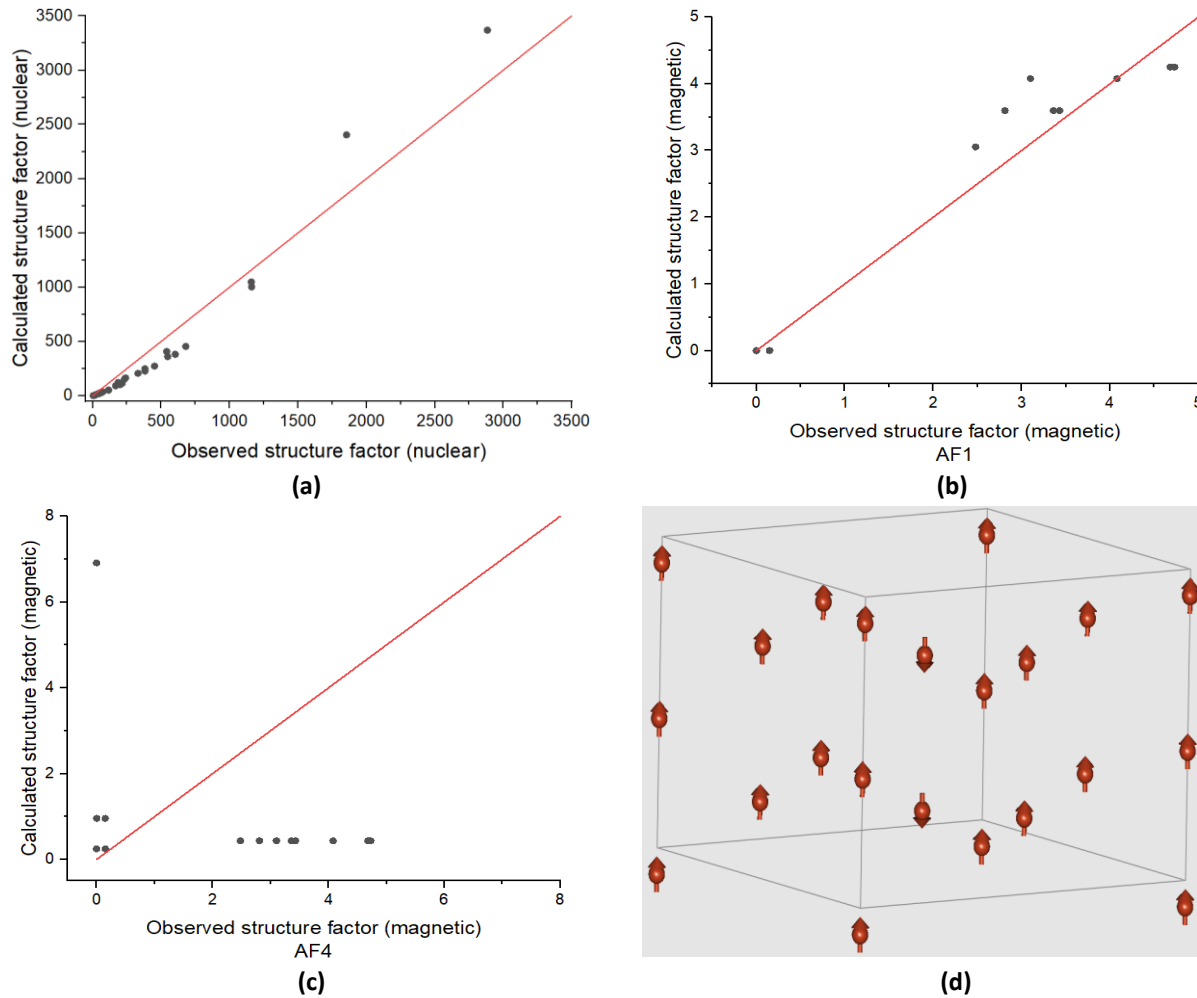
Fig. 3.9: (a) Nuclear structure factor according to refinement versus observed nuclear structure factor; (b) (c) magnetic structure factor according to refinement against model AF1 and AF4, respectively, versus observed structure factor; two red lines y=x are plotted for reference; (d) refined AF1 spin configuration at base temperature.

For the magnetic structure determination at 1.5 K, firstly, magnetic Bragg peaks were selected when the integrated intensity at 1.5 K and 10 K exhibit clear differences. The list ranges from low index (1 0 0) to higher index (1 2 2) peaks. The refinement of magnetic peaks were tested against the seven symmetry-allowed ferrimagnetic spin configurations identified previously in Ref. [23], called AF1 – AF7. The best refinement versus the experimental data was obtained using the AF1 model. The calculated magnetic structure factor of AF1 model is compared with experimental data in Fig. 3.9 (b), where reasonable agreement can be found (refinement quality factor RF = 11.39). Further consistency can be found in Ref. [23] which also claimed the AF1 model as the most likely to be the correct magnetic ground state, though this was left open in this earlier study since only powder neutron diffraction data were obtained so the candidate models could not be reliably discriminated. Indeed, in the earlier work [23], the AF4 model was suggested as providing the best consistency with the powder neutron diffraction data. As seen in Fig. 3.9 (c), the refinement of the single crystal data according to AF4 model is so poor that it can be ruled out.

The real space spin configuration of the refined AF1 model is shown in Fig. 3.9 (d). It is a 3-up 1-down configuration and the length of magnetization is determined to be 0.91(1) μ_B per V^{4+} ion. This leads to an equivalent bulk moment of 0.455 μ_B per formula unit, in agreement with the reported value in Ref. [26]. Here, the spins at the body-center of the unit cell – V(2) sites are anti-parallel to the spins at the edges and corners of the unit cell – V(1) and V(3) sites. This directly determined magnetic ground state is important for testing the linear spin wave theory simulation of the magnon excitation spectrum in $VOSe_2O_5$.

3.4   Neutron spectroscopy studies

In this section, we present results obtained from inelastic neutron scattering. After a brief introduction to sample preparation, the dispersion of magnon excitations in $VOSe_2O_5$ measured at three TAS beamlines (TASP, IN12 and CAMEA) is presented. This result is at the heart of the scattering project in this thesis work, because it examines the principal magnetic interactions that stabilize the observed magnetic ground state at base temperature. The measured spectrum is compared with linear spin wave simulations using the SpinW software which allows extractions of microscopic exchange interactions [55]. The values provide the crucial feedback to the quantum chemistry calculations. Single crystals were provided by Dr. Arnaud Magrez and Mr. Priya Baral, the Institute of Physics, EPFL.

3.4.1   Sample preparation

Since the inelastic neutron scattering cross-section is much weaker than the elastic scattering cross-section, and magnetic vanadium is weak spin ½ ion with intrinsically high incoherent background, a sufficient amount of sample mass is required in order to observe detectable signals. Here, a co-aligned mosaic consisting of around 80 $VOSe_2O_5$ single crystals was prepared. They were distributed on the front and back sides of two aluminum plates and fixed using a Cytop glue which is hydrogen-free and hence does not itself significantly contribute to the background scattering intensity. Fig. 3.10 (a) shows a photo of the mosaic on one side of a plate. The crystals selected for inelastic neutron scattering experiments have a square-plate shape, where the a-b plane is in the plane of the plate, and the c-axis points perpendicular to the plate. As a result, co-alignment becomes much more convenient and accurate, thanks to this crystal morphology.

The quality of the co-aligned mosaic was examined by neutron diffraction at the Morpheus beamline, PSI. A photo of the sample mounted on the Euler cradle at Morpheus is shown in Fig. 3.10 (b). At room temperature, the crystallographic planes (2 0 0) and (0 0 2) were selected to characterize the mosaic due to the expected high scattering intensity. The width of intensity distribution represents the spread of a-axis and c-axis in the mosaic. These two Bragg peaks were scanned in the a-b plane and out of plane, indicated by polar angle and azimuthal angle in Fig. 3.10 (c) and (d). According to the 2D intensity maps, the spread is largely contained within 2 degrees in the a-b plane and within 4 degrees out of plane, with some signal from more strongly misaligned grains also observed. This characterization illustrates that a sufficiently large number of crystals are co-aligned with the expected orientation, and with sufficiently small mosaic spread for inelastic neutron scattering studies.

(a)

(b)

(c)

(d)
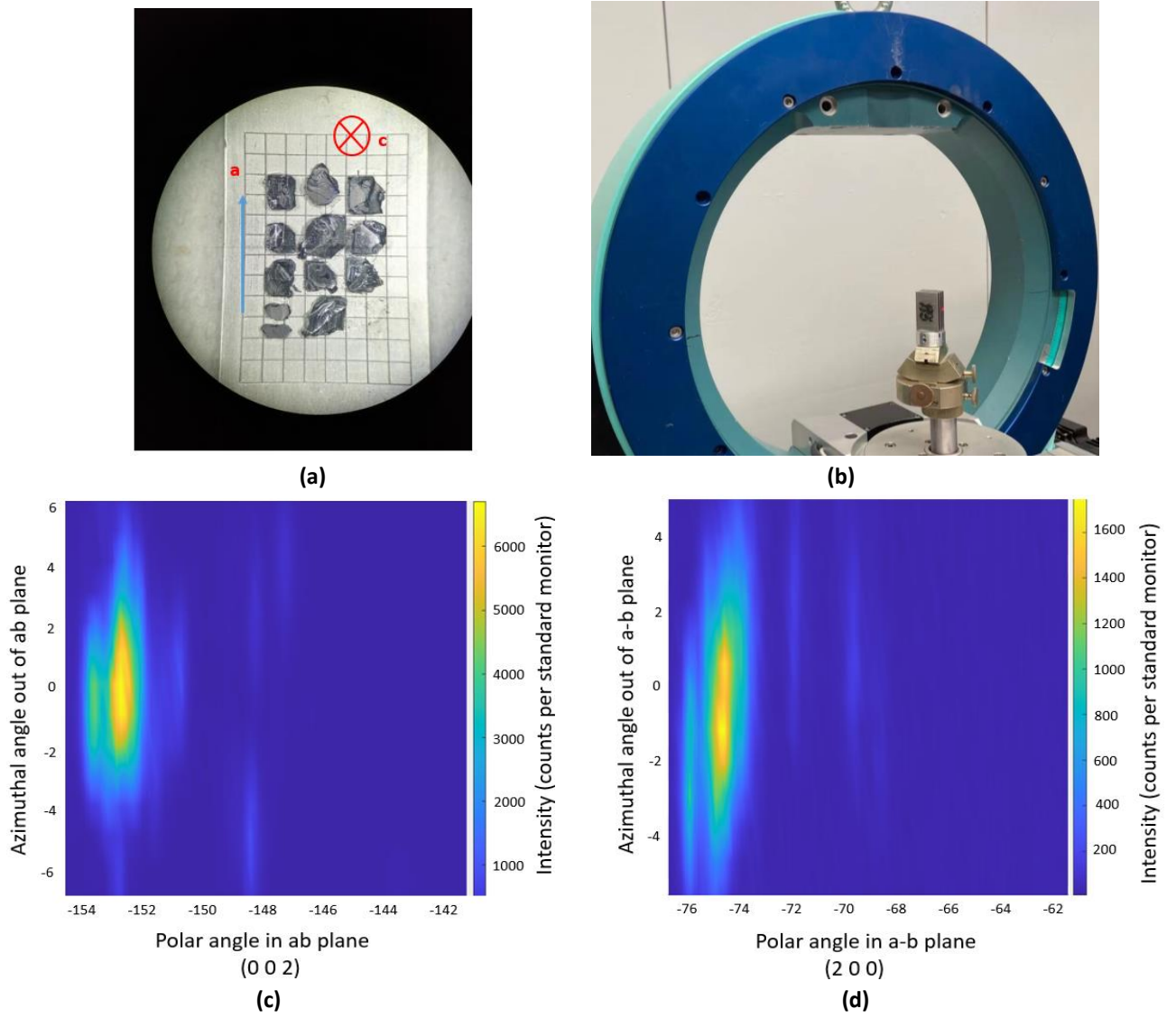
Fig. 3.10: (a) Photo of co-aligned VOSe$_2$O$_5$ single crystal mosaic on an aluminum plate; (b) photo of the sample mounted on the Euler cradle at the Morpheus neutron diffractometer, PSI; (c) (d) the intensity distribution of (0 0 2) and (2 0 0) in a-b plane and a-c plane, indicating the spread of c-axis and a-axis, respectively.

3.4.2 Neutron spectroscopy measurements

Firstly, the magnon spectrum of VOSe$_2$O$_5$ in magnetic ground state was explored at the TASP beamline, PSI. Since the energy of magnon excitations were expected to lie within a bandwidth of just a few meV, a cold neutron spectroscopy beamline was selected. Measurements were performed with a fixed outgoing neutron wavevector k_f = 1.55 Å^{-1} (E_f = 5meV). The incoming neutron energy varied in order to cover energy transfer up to 5 meV at various locations of momentum transfer. Constant energy scans were performed for selected high symmetry q directions in reciprocal space – (1 0 L), (H 0 1) and (H 0 0). The energy resolution of the instrument at this setting is 0.16 meV, thus 0.1 meV was chosen as the step of energy scan. The experiment was performed at base temperature 1.5 K without external magnetic field. A picture of the sample holder setup is shown in Fig. 3.11 (a), where the bottom is covered by a neutron-absorbing cadmium foil to reduce background noise. For the measurements, a counting monitor of 100,000 was chosen which took roughly 6 minutes to complete counting at a given energy transfer and q point. A typical energy scan for (1 0 1) at 1.5 K is displayed in Fig. 3.11 (b). The high intensity on the approach to 0 meV is due to a tail of scattering from the elastic position, while a weaker peak signal near 3 meV is due to magnon scattering.
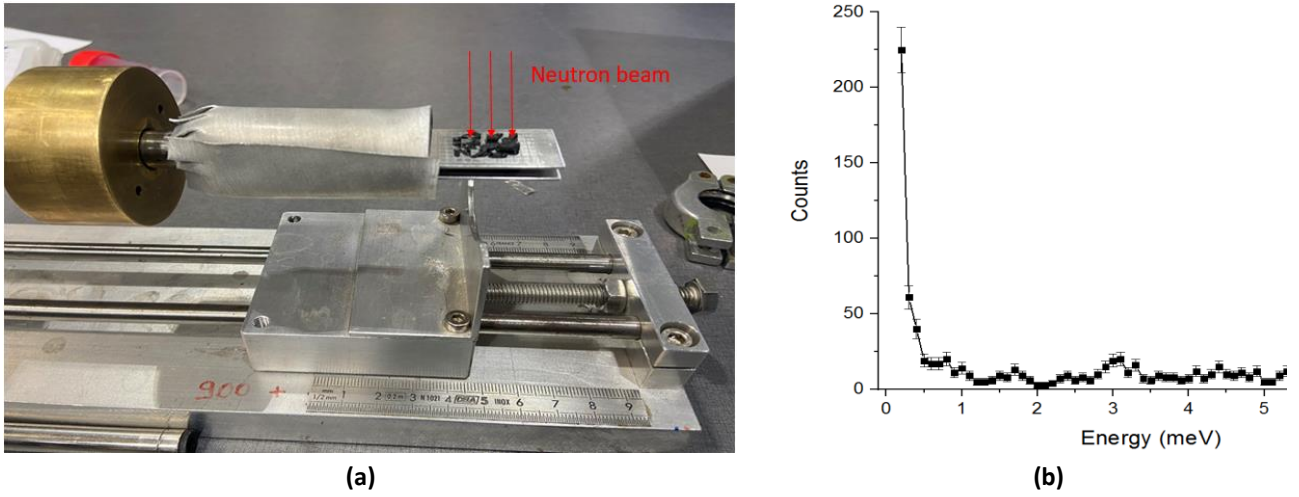
Fig. 3.11: (a) A photo of the sample and sample holder setup; (b) a typical scan for (1 0 1) at 1.5 K.

In Fig. 3.12 (a), a detailed scan at (1 0 0.5) from 1 meV to 5 meV is presented. Next to the magnon peak near 3 meV, there is a broad peak near 4 meV. At first, it was considered to be a phonon mode because, unlike the magnon mode near 3 meV, the intensity did not vanish at temperatures above the Curie temperature. However, more dedicated studies revealed that this feature is actually a so-called Currat-Axe spurion [66], which appears when q is parallel to k_f and $|k_f + q| = |k_i|$. In this configuration, the analyzer scatters an elastic incoherent signal from the sample which subsequently appears as a deceiving inelastic peak [66].

The dispersion of the magnon mode near 3 meV constructed from 1D scans at TASP is plotted as 2D color maps in Fig. 3.12 (b) - (d), along the three selected high symmetry directions in reciprocal space. The main magnon mode appears rather flat, as expected for an optical mode, though the intensity is observed to vary strongly with q. This result implies that there are competing magnetic interactions, in addition to acoustic magnon modes at lower energy transfer. They were not detected by TASP due to limitations in the flux and thus available beamtime needed for searching and surveying all magnon modes.

(a)

(b)
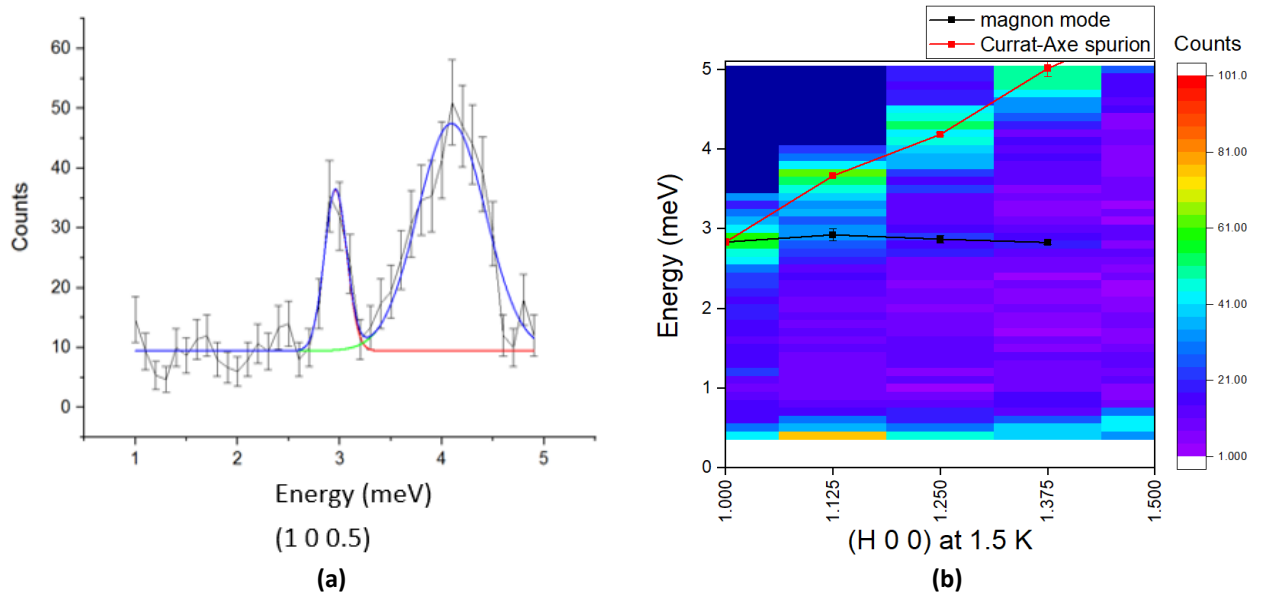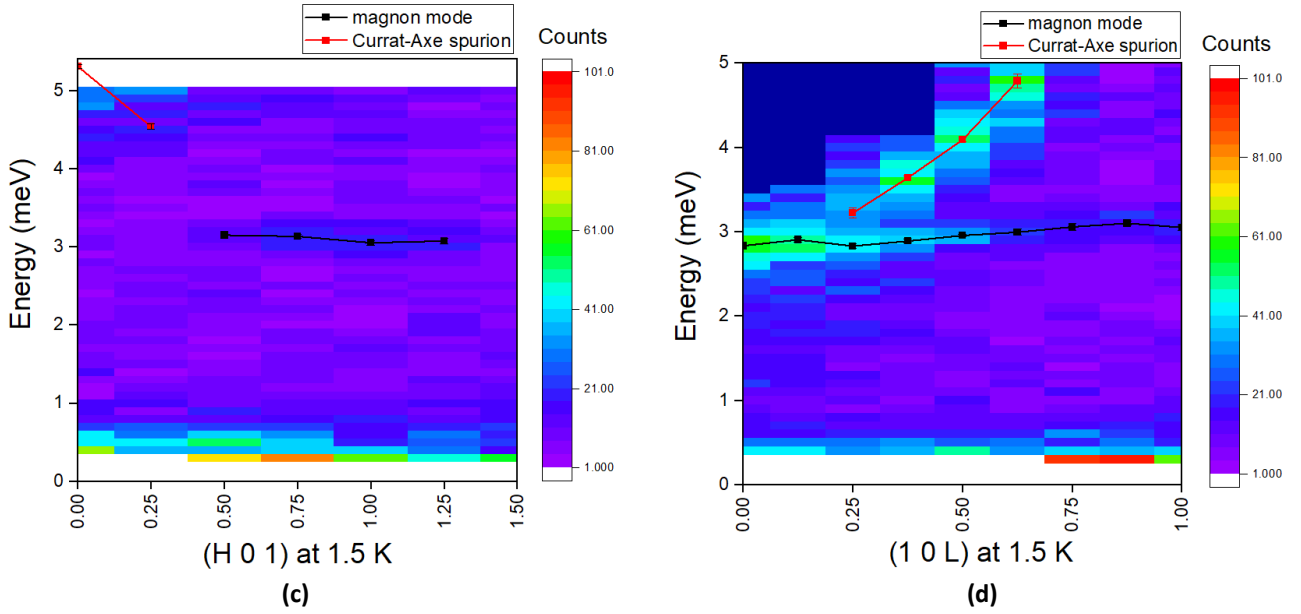
*Fig. 3.12: (a) Energy scan at (1 0 0.5) from 1 meV to 5 meV at 1.5 K. Two Gaussian functions with constant background fit two peaks, and the blue curve is the overall function; (b) - (d) 2D color maps of energy transfer up to 5 meV versus **q** along (H 0 0), (H 0 1) and (1 0 L), respectively, showing the data at 1.5 K only. Counts in the intensity scale bar refers to counts per standard monitor.*

The effect of temperature was also investigated along (1 0 L) at TASP. Fig. 3.13 shows the same 2D color map at 6 K and 10 K, where the sample is in the IC-1 cycloidal phase and paramagnetic phase, respectively. The intensity of the magnon mode near 3 meV starts to decrease at 6 K and eventually vanishes at 10 K. It is noted that at 6 K, the color map indicates that additional intensities appear at low energy transfer up to around 1 meV. These intensities include contributions from magnon excitations due to the cycloidal spin configuration in IC-1 phase. However, the intensity pattern amounts to the overlap of several modes and it is infeasible to resolve them. At this stage it is considered infeasible to obtain sufficient data to determine the spin Hamiltonian from the cycloidal phase, even it lies in closer proximity to the Néel-type skyrmion phase. Instead, the subsequent experiments were focused on the more tractable problem of determining the spin Hamiltonian for magnetic ground state at base temperature.
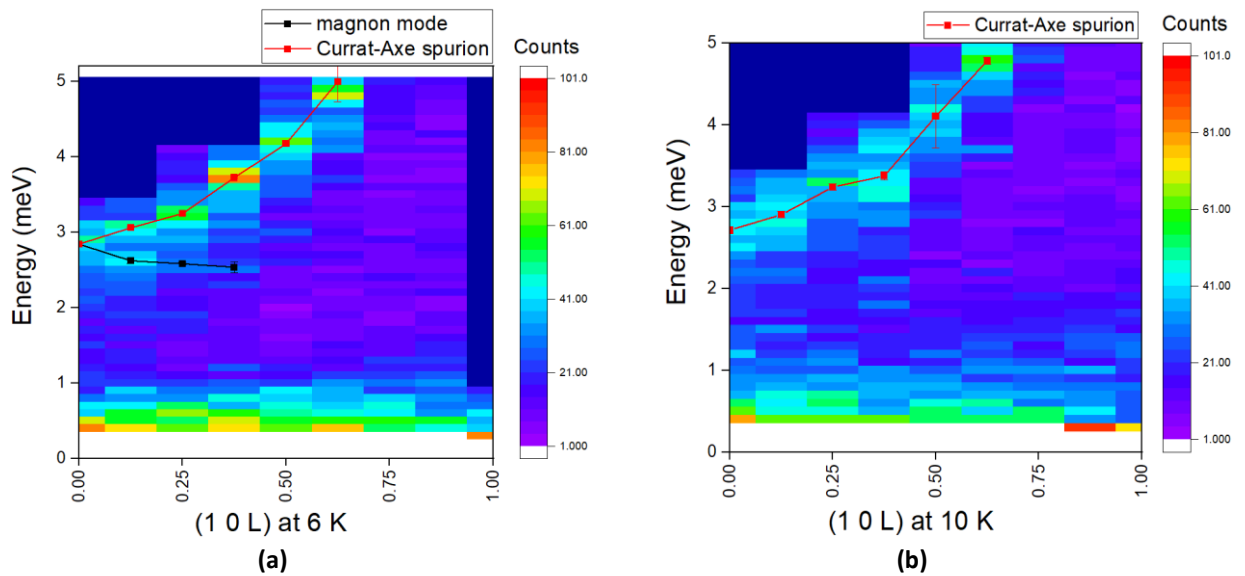
*Fig. 3.13: 2D color map of energy transfer versus **q** along (1 0 L) at (a) 6 K and (b) 10 K, respectively, showing the data at 1.5 K only. Counts in the intensity scale bar refers to counts per standard monitor.*

To search for possible acoustic-like magnon modes at lower energy transfer, the same mosaic was measured at the IN12 beamline, ILL where the cold neutron flux is much higher than at TASP. Two wavevector settings were implemented: k_f = 1.1 Å^{-1} to cover energy transfer from 0.2 meV to 1 meV; k_f = 1.3 Å^{-1} to cover energy transfer from 1 meV to 3.6 meV. The energy resolution can reach 0.1 meV at both settings, hence 0.05 meV was selected as the step of energy scan. The counting monitor was set to be 2,000,000 which corresponded to approximately 6 minutes of counting time at each point in the magnon spectrum.

Using the first setting k_f = 1.1 Å^{-1}, a new low energy mode was identified around 0.6 meV, and its dispersion was measured along two high-symmetry directions in reciprocal space: (H 0 1) and (1.5 0 L). Two example scans at (1.5 0 0) and (1.5 0 1) with energy transfer from 0.2 meV to 1 meV are shown in Fig. 3.14 (a) and (b). Peaks at 1.5 K are fitted by Gaussian function with an exponential background which takes into account the intensity from the elastic tail. In addition, each scan is repeated at 50 K to provide comparison. The fact that the peak vanishes at 50 K further supports the presence of the magnon mode at this energy transfer. Its dispersion is plotted in 2D color maps, shown in Fig. 3.14 (c) and (d), along H and L directions, respectively.
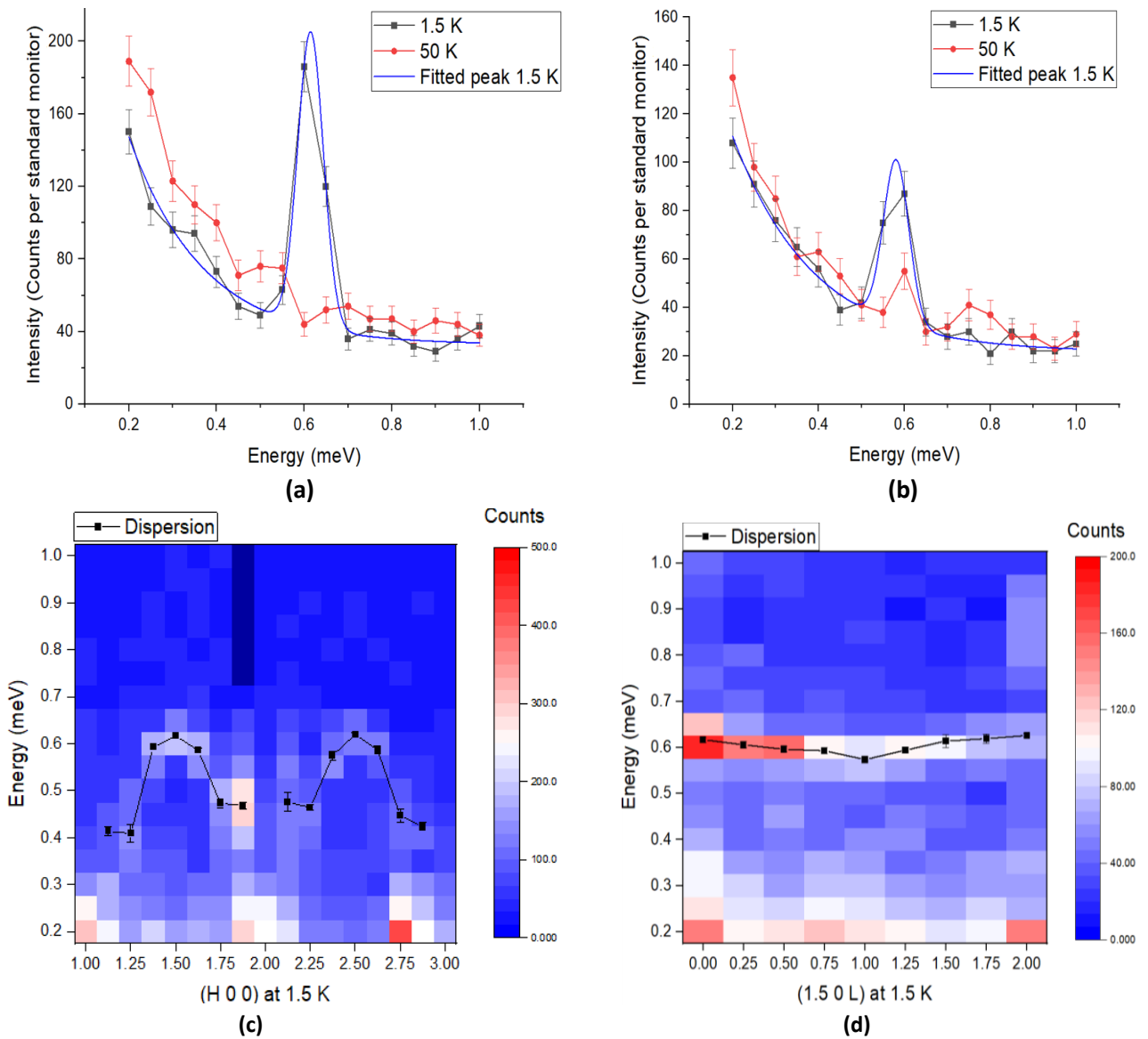
Fig. 3.14: (a) (b) Energy scans at (1.5 0 0) and (1.5 0 1) at 1.5 K and 50 K. Scans at 1.5 K are fitted by a Gaussian function with exponential background; (c) (d) 2D color maps constructed from 1D scans of energy transfer from 0.2 meV to 1 meV versus **q** along (H 0 0) and (1.5 0 L). Only data from 1.5 K are plotted in the color maps. Counts in the intensity scale bar refers to counts per standard monitor.

This mode displays a notable dispersion in the H direction and a comparatively weaker dispersion in the L direction. Intriguingly, the dispersion along H becomes flat near integer values of H along (H 0 0) (H = 1, 2 or 3). This implies that there are additional magnetic interactions other than exchange interactions in the spin Hamiltonian which gap out the spectrum and prevent this mode from softening at the zone centers.

In the other setting k_f = 1.3 Å^{-1}, another magnon mode near 1.5 meV was identified. Fig. 3.15 (a) provides an example scan at (1 0 2) for this mode. Its dispersion along the L direction was measured and plotted as a 2D color map in Fig. 3.15 (c). The intensity of this mode is the strongest at (1 0 2), and starts to become weaker in both directions of increasing and decreasing L. It becomes too weak to be measured at (1 0 1) and (1 0 2.75). This implies that the intensity of this mode modulates periodically along L. This finding was later confirmed by the results to be presented shortly from the CAMEA beamline, where the dispersion across multiple Brillouin zones could be measured efficiently. The dispersion of this mode along H was not measured at IN12 due to the limitation of beamtime.
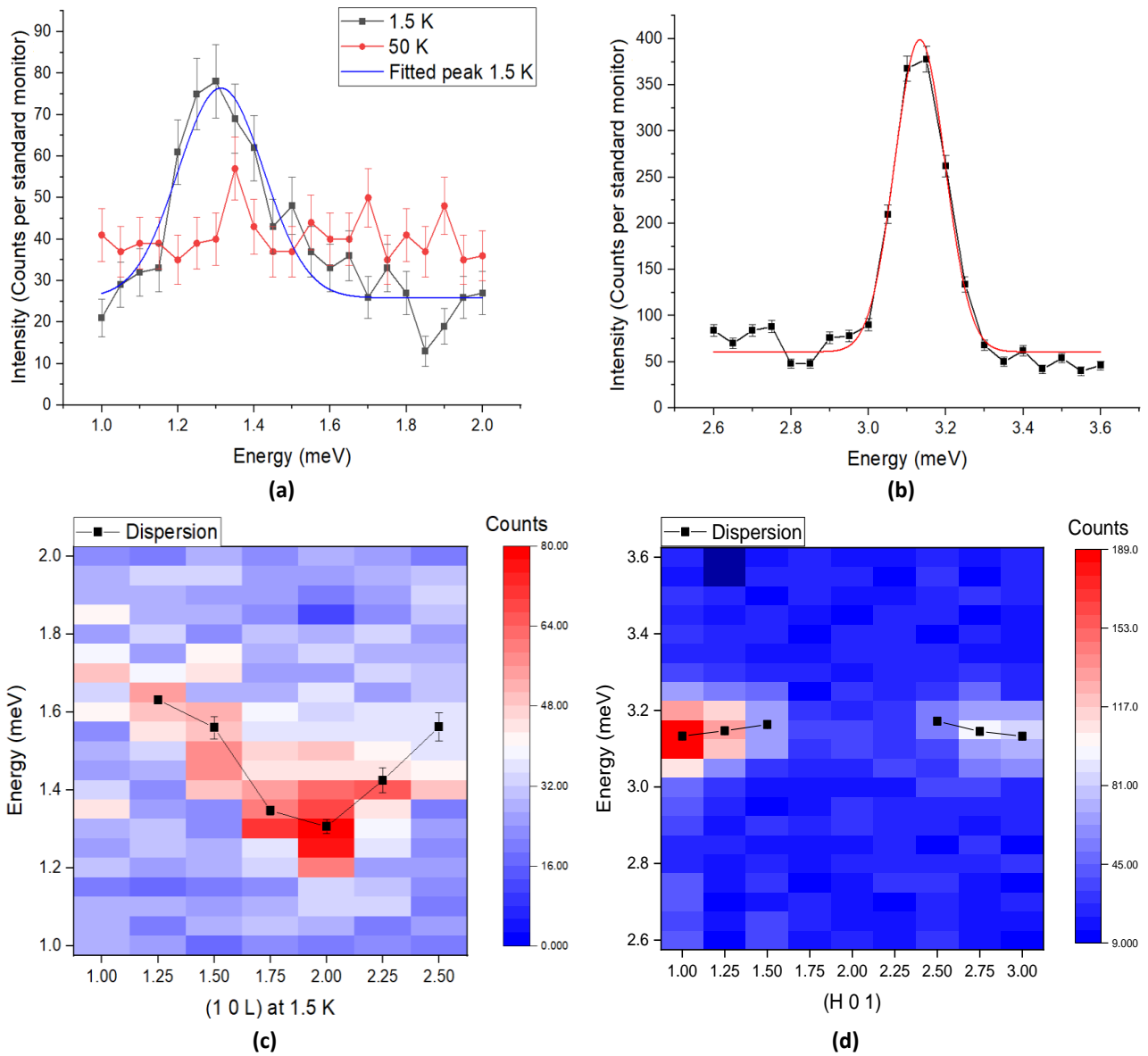
Fig. 3.15: (a) (b) Energy scan at (1 0 2) and (1 0 1) at 1.5 K and 50 K, indicating the mode near 1.5 meV and 3 meV, respectively; (c) 2D color map constructed from 1D scans of energy transfer from 1.0 meV to 2.0 meV versus **q** along (1 0 L); (d) 2D color map of energy transfer from 2.6 meV to 3.6 meV versus **q** along (H 0 1). Only data from 1.5 K are plotted in the color maps. Counts in the intensity scale bar refers to counts per standard monitor.

Finally, the magnon mode near 3 meV already discovered at the TASP beamline was identified again at IN12. An example scan at (1 0 1) and its dispersion along H direction are shown in Fig. 3.15 (b) and (d), respectively. Again, the intensity is weak in the range 1.5 < H < 2.5, which implies the magnon dispersion modulates in intensity periodically in $VOSe_2O_5$.

Since there are four V^{4+} magnetic ions in the unit cell of $VOSe_2O_5$ determined by occupancy, four modes are expected to be present in its magnon dispersion according to band theory. Within the range of energy transfer from 0.2 meV to 3.6 meV, the results obtained from the cold neutron beamlines TASP and IN12 have revealed three modes near 0.6 meV, 1.5 meV and 3.0 meV. Hence, another mode is expected, and suspected to be dispersing at higher energy transfers. As TAS-type of beamlines become inefficient at higher energy transfer, where energy resolution is low and point-by-point counting time becomes so long, the CAMEA beamline at PSI was employed to search for the suspected magnon mode above 3.6 meV. The incoming neutron energy varied from 3.6 meV to 10.2 meV, allowing a coverage of energy transfer from 0.2 meV to 12 meV across entire Brillouin zones. The measurement was only performed at 1.5 K, and background was taken into account through a subtraction of powder-averaging applied to portions of the collected data where no magnon intensity or spurious background intensity, e.g. Currat-Axe spurions, exist.
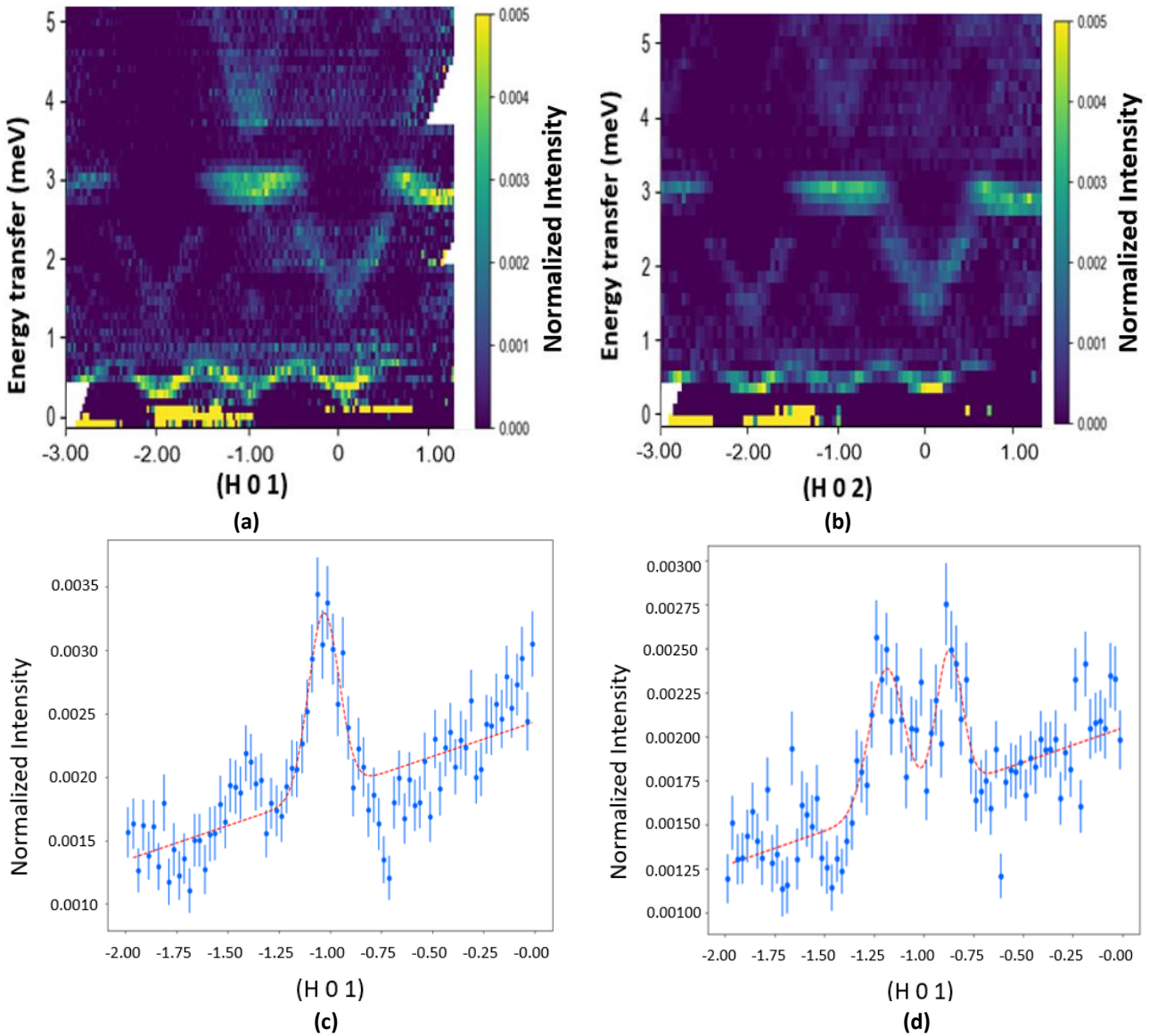
Fig. 3.16: 2D color map of energy transfer versus (a) (H 0 1) and (b) (H 0 2), measured by CAMEA beamline. (c) Intensity versus H along (H 0 1), integrated from 4 meV to 4.2 meV and from 4.4 meV to 4.6 meV, respectively.

Fig. 3.16 (a) and (b) display subtracted data along (H 0 1) and (H 0 2) from 0 meV to 5 meV energy transfer. The integration width out of plane (along L) is set to be 1 reciprocal lattice unit. Four modes are clearly identified, in which the bandwidths of the three lowest energy branches are consistent with the data measured at the TASP and IN12 beamlines. The highest energy mode is found to disperse within the range from 4 to 5 meV energy transfer. As expected, all modes modulate in intensity periodically with the reciprocal lattice. No further modes above 5 meV energy transfer were found either at CAMEA, or in a subsidiary experiment at the thermal TAS at EIGER beamline, PSI (data not shown).

To characterize the dispersion of the newly discovered highest energy mode, constant energy cuts were made to the dataset and fitted by a Gaussian function with linear background. Fig. 3.16 (c) shows intensity integrated over 4 – 4.2 meV range against H along (H 0 1). The single peak near (-1 0 1) corresponds to the bottom of the dispersion. As the range of integrated energy moves to higher energy transfer, the cut starts to show two peaks. An example cut is shown in Fig. 3.16 (d), integrated over 4.4 – 4.6 meV.

The dispersion along the L direction can also be extracted from the CAMEA dataset. Plots in Fig. 3.17 show the subtracted data along (1 0 L) and (2 0 L) from 0 meV to 5 meV energy transfer. The integration width along H is set to be 1 reciprocal lattice unit. Unfortunately, except the mode near 3 meV, the intensity of the other three modes is extremely weak. The 3 meV mode also almost vanishes along (2 0 L), implying the modulation of intensity along L. The energy and dispersion of this mode is consistent with the data measured at the TASP beamline.
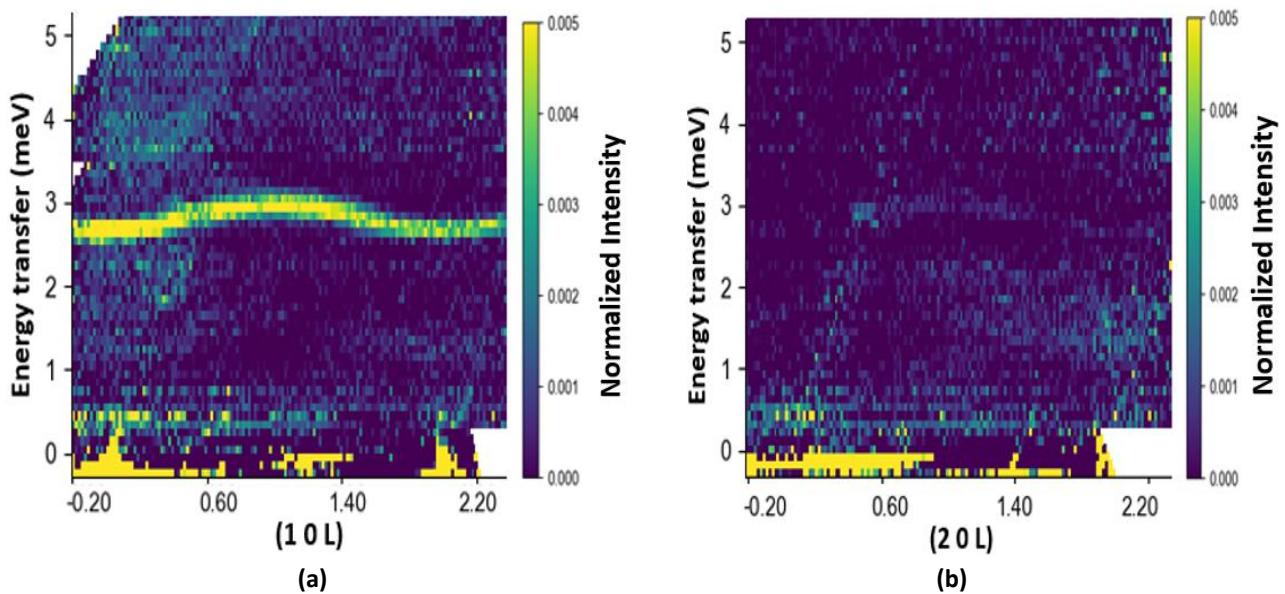
Fig. 3.17: 2D color maps of energy transfer versus (a) (1 0 L) and (b) (2 0 L), measured by CAMEA beamline. The data presented are subtracted by background.

To better determine the magnon dispersion in $VOSe_2O_5$ experimentally, and provide additional data for comparison with the simulation, the mosaic was rotated by 45 degrees around the c-axis so the dispersion in (H H L) planes could be measured by CAMEA. The sample holder configuration with respect to the incoming neutron beam and axes of the mosaic are displayed in the photo of Fig. 3.18. The integration width along the L direction is set to be 1 reciprocal lattice unit.
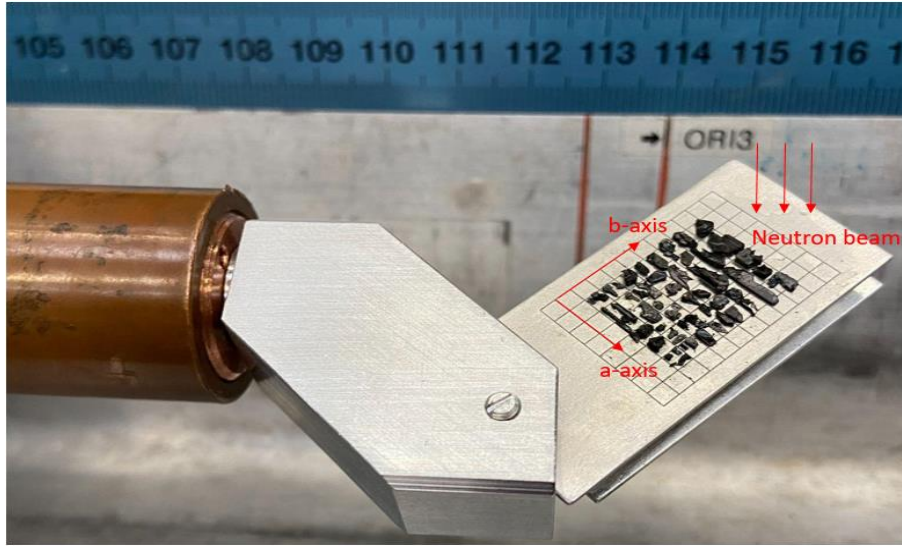
Fig. 3.18: A photo of the sample and sample holder setup, where the aluminum plates are rotated by 45 degrees in a-b plane. The neutron beam and a-b axes of the mosaic are indicated.

Two magnon modes were identified with comparatively stronger intensities than the modes in (H 0 L) planes, shown in Fig. 3.19 (a) and (b). They correspond to the modes at the second lowest and highest energy transfers, respectively. The flat mode near 3 meV in (H 0 L) planes was found to have vanishing intensity in (H H L) planes. However, the intensity of the mode at the lowest energy transfer, and the dispersion along the L direction, were both too weak to be measured.
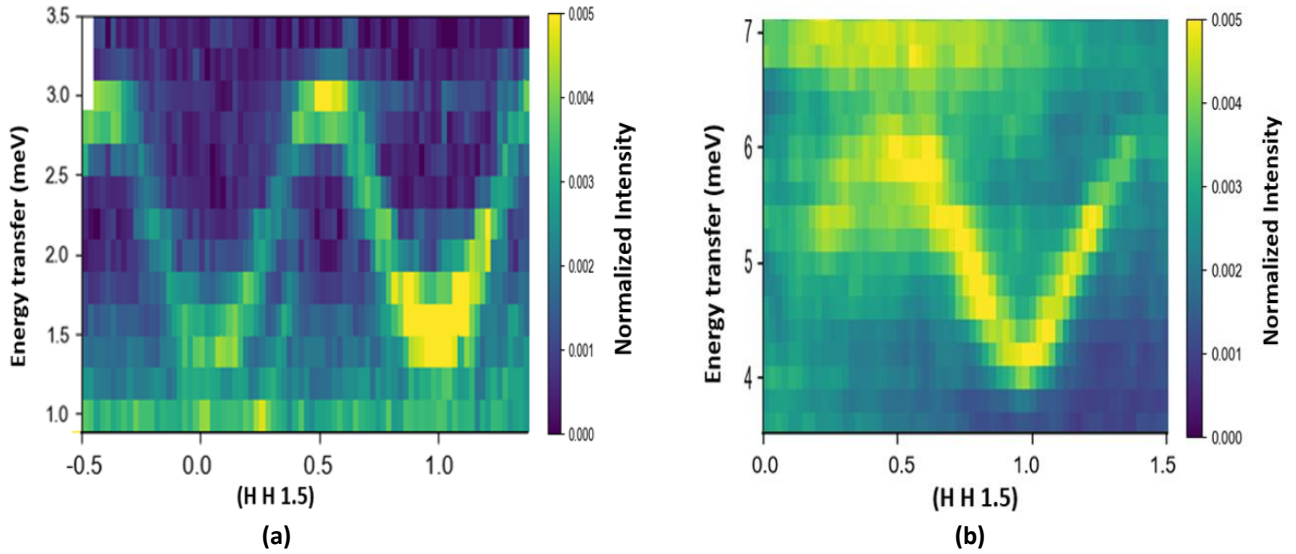
Fig. 3.19: The magnon dispersion measured along (H H 1.5) in the energy transfer range (a) 1 meV - 3.5 meV and (b) 3.5 meV - 7 meV, respectively.

3.4.3 Overview of quantum chemistry calculation

The microscopic spin Hamiltonian of $VOSe_2O_5$ can be proposed theoretically using many-body wavefunction calculations on the electrostatically embedded finite-size model based on the crystal structure described in Section 3.2.2. The detailed calculations were performed by Dr. Ravi Yadav, Institute of Physics, EPFL.

As introduced earlier, the crystal structure consists of three types of V^{4+} ions that are octahedral-coordinated by oxygen atoms. The finite-size model comprises a central unit hosting two octahedral. The central unit is treated by multi-reference wavefunctions surrounded by the nearest octahedral, while the other octahedral

account for the charge distribution in the vicinity of the central unit and are treated at the Hartree-Fock level. The crystalline environment is restored by embedding each model in an array of point charges thus the long-range Madelung electrostatic potential is reproduced [67]. All-electron basis functions are used for the V^{4+} ions in the two-octahedral central unit while the bridging ligand ions are modeled with an all-electron basis set. Electron correlation effects in the central units are described at the complete-active-space self-consistent field (CASSCF) and multi-reference configuration interaction (MRCI) levels of theory [68], including spin-orbit interactions. Each V^{4+} ion has only one electron in the d_{xy} orbital. The two electrons belonging to the two V^{4+} ions are considered in the active space along with $2p$ bridging ligand orbitals. MRCI calculations involve single and double excitations from $3d$ valence shells of V^{4+} ions and p valence shells of the bridging ligands. The ab-initio data consisting of four spin orbit states (one singlet and one triplet state) are mapped onto the model spin Hamiltonian in the spin-orbit coupled basis. The symmetric Heisenberg interaction and anti-symmetric DMI are obtained using such analysis for three types of J_1 (called J_{1a}, J_{1b} and J_{1c}), J_2 and J_3 as shown in Section 3.2.2. It is remarked that the embedded finite-size model has proven to be effective in describing electronic excitations and magnetic interactions in a rich variety of strongly correlated insulators [69, 70], including d-electron lattices [71-75], owing to their localized nature. Fig. 3.20 displays the orbital plot of J_{1a} exchange interaction relevant for the calculation, where Fig. 3.20 (a) is a view along the c-axis of the d_{xy} orbitals of V^{4+} central unit, and Fig. 3.20 (b) is an in-plane view indicating the spatial distribution and overlap between p orbitals of the oxygen ligands and d_{xy} orbitals of V^{4+} ions. Further results are discussed in the next section.

(a)	**(b)**
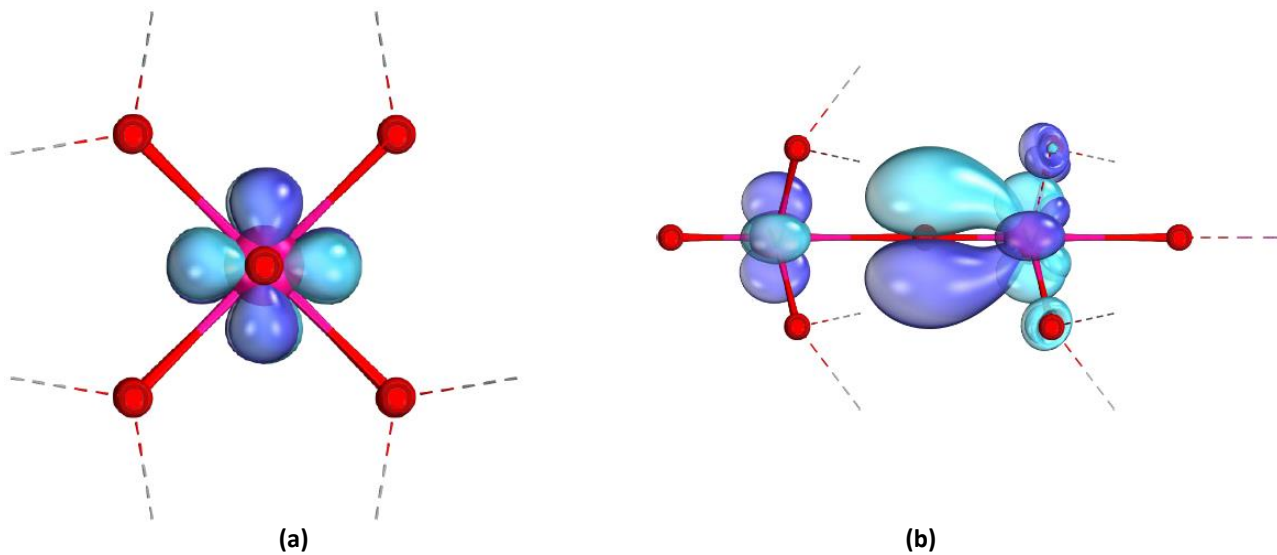
Fig. 3.20: Schematic illustration of J_{1a} orbitals. (a) is a top-down view along the chain, (b) is the side view. The V^{4+} central unit sits at the center of image (a).

3.4.4 Spin Hamiltonian according to SpinW fitting

The magnon dispersion of $VOSe_2O_5$ at base temperature measured at the TASP, IN12 and CAMEA beamlines was fitted using the SpinW simulation software [55], which calculates the dispersion according to linear spin wave theory introduced in Section 2.4.1. The magnetic ground state determined at ZEBRA beamline was entered into the SpinW script as the starting ground state spin configuration. The magnetic interaction scheme that can stabilize the observed ground state can be extracted from an optimization of the interaction parameters.

A comparison between the experimentally determined dispersion and the simulated dispersion with optimal fitting of the interaction parameters is presented in Fig. 3.21. The error bars represent the width of magnon peaks measured in experiments, and they are either horizontal or vertical depending on whether constant

energy scans/cuts or constant **q** scans/cuts are performed. The magnon dispersion obtained from simulation also disperses in intensity periodically, in agreement with the observation from experiments. The periodicity of the dispersion in reciprocal lattice units along the L direction is twice as much as that along the H direction. This is due to the crystal structure, since there are twice as many V^{4+} ions along the a-axis as there are along the c-axis in real space. One notable feature in the experimentally determined spectrum is the existence of a low energy gap across the entire Brillouin zone, and no genuinely soft modes descending to zero energy transfer. To account for the energy gap in the SpinW simulation, an Ising-type anisotropy term along the polar axis was introduced. A pictorial interaction scheme including exchange interactions, anisotropy and spin configuration in the SpinW model is provided in Fig. 3.22. Here, g_1 represents *g*-factor anisotropy, which by calculations is almost isotropic and has negligible effect on the magnon dispersion. The SpinW script used for simulating the magnon spectrum and extracting the interaction parameters, also the experimental data of fitted spin wave modes are provided in the Appendix.
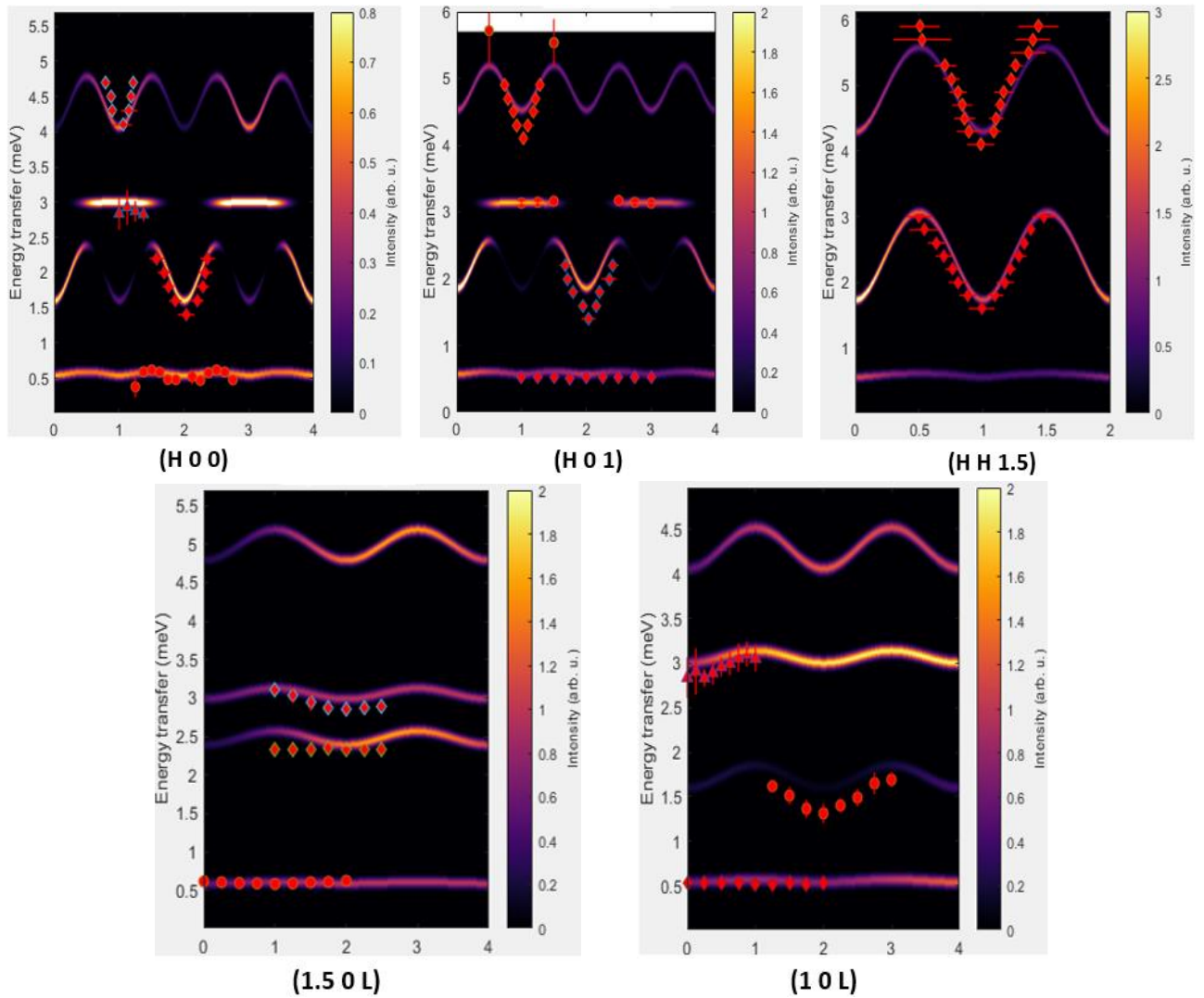
Fig. 3.21: Magnon dispersion of VOSe$_2$O$_5$ at base temperature fitted to experimental data by SpinW software. Different symbols represent data measured from different beamlines: sphere – IN12, triangle – TASP, diamond – CAMEA.
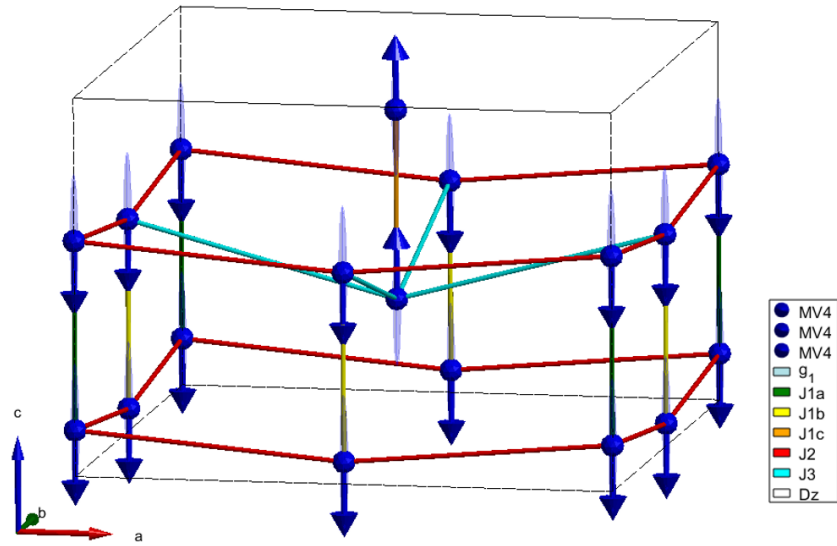
Fig. 3.22: A schematic overview of spin configuration, relevant magnetic bonds and anisotropy applied in SpinW simulation.

Finally, a comparison between the best fit of the magnetic interactions according to SpinW and Quantum Chemistry (QC) calculations is presented in Table 1. The exchange interactions, from J_{1a} up to J_3, are calculated by Quantum Chemistry, while the estimate for the magnetic anisotropy energy D_z was obtained by a DFT calculation. The latter was done by artificially aligning all spins along a-axis and c-axis, and then computing the energy difference between these two configurations. The result of this calculation suggest that the configuration along the c-axis has lower energy, which agrees with the magnetic structure determined at the Zebra beamline. The results of both the SpinW fitting and the QC calculation suggest that the third nearest-neighbor exchange, J_3, is the dominant exchange interaction. Here, the magnetic anisotropy is found to feature exchange anisotropy, that is, the dominant exchange J_3 has different magnitude in the a-b plane (J_{3xy}) compared with the out-of-plane (J_{3z}) directions. The difference along these two directions is expected to be equal to the D_z term introduced to SpinW simulation, which is also evaluated by DFT calculation. The magnitude of DMI on the J_3 bond was also calculated by QC. The value is 0.1 meV, called DM_3 in Table 1. However, its existence cannot be verified by fitting the spectrum in SpinW simulation due to its small overall effect on the magnon spectrum. The interaction scheme obtained from fitting the dispersion by SpinW has an anisotropy term D_z as one of fitting parameters, so the J_3 in the script is entered as J_{3xy} while J_{3z} is given by the summation between J_{3xy} and D_z. Since the interaction scheme obtained from theoretical calculations treated anisotropy D_z in a separate DFT calculation, the calculated J_3 by QC is interpreted as J_{3z} while J_{3xy} is given by the subtraction of D_z from J_{3z}.

Magnetic interaction (meV)	SpinW simulation and fitting	Calculations (results)	Calculations (comparison)
J_{1a}	-0.01	-0.20 (QC)	-2.10 (DFT)
J_{1b}	-0.07	-0.20 (QC)	-2.10 (DFT)
J_{1c}	-0.18	-0.85 (QC)	-2.10 (DFT)
J_2	-0.22	-1.00 (QC)	-2.20 (DFT)
D_z	0.52	0.67 (DFT)	
J_{3z}	2.70 (summation)	2.70 (QC)	3.50 (DFT)
J_{3xy}	2.18	2.03 (subtraction)	
DM_3	N/A	0.1 (QC)	

Table 1: Comparison between the spin Hamiltonian obtained from SpinW simulation and calculations. All values have unit meV.

3.5 Discussion, summary and outlook

The spin Hamiltonian obtained from both QC calculations and inelastic neutron scattering data display reasonable consistency. Consistent results include the identification of J_3 as being both antiferromagnetic and the strongest exchange interaction, and the nearest-neighbor interactions J_{1a-1c} as being the weakest and ferromagnetic in nature. Notably, the value of 2.7 meV for J_{3z} given by QC and SpinW fitting have perfect agreement. For comparison, Table 1 also shows exchange interactions evaluated by DFT calculations using GGA+U functional (U_{eff} set at 3 eV, calculation also contributed by Dr. Ravi Yadav, Institute of Physics, EPFL). The value of J_3 computed by DFT is roughly 30% higher than that computed by QC. In addition, the accuracy of J_{1a-1c} values given by Quantum Chemistry is improved by an order of magnitude compared with those obtained by DFT. This suggests Quantum Chemistry as a more convincing tool for computing microscopic magnetic interactions in complex magnetic systems.

The reason why the third shortest V-V bond has the strongest exchange interaction can be understood microscopically in terms of orbital overlaps plotted in Fig. 3.23. Despite comprising the shortest V-V bond lengths, the three types of J_1 have only one exchange path. As illustrated in the crystal structure in Section 3.2.2, V^{4+} ions are shifted along the c-axis by a small amount from their respective octahedral centers, hence, there are one short and one long axial V-O bonds along V(1) chains. The overlap between the p-orbital of oxygen and the d_{xy} orbital of one V^{4+} ion is much stronger in one direction than in the other direction. This greatly suppresses super-exchange interaction between V^{4+} ions along the chain. In addition, the d_{xy} orbital lobes of two neighboring V^{4+} ions are oriented parallel to each other. The overlap between d_{xy} orbitals, and thus the direct exchange of J_{1a-1c}, is also small. The situation for J_2 is similar. There are two principal exchange pathways in the tetragonal plane, however, the d_{xy} orbital lobes of V^{4+} ions are still not oriented directly to each other, though the resulting strength of the exchange interaction is comparatively stronger compared with J_{1a-1c}. In contrast, for J_3 the oxygen ligands sit in the center of V-O-V bonds, and the d_{xy} orbital lobes of V^{4+} ions directly point to each other. This creates considerable amount of orbital overlap through super-exchange interaction involving the mediating oxygen ligands, making J_3 the dominant exchange interaction in this system. The important role of magnetic oxygen anions in the dominant exchange bonds was demonstrated by XMCD signals in resonant elastic x-ray scattering, shown in Fig. 3.5 (b).

(a) **(b)** **(c)**
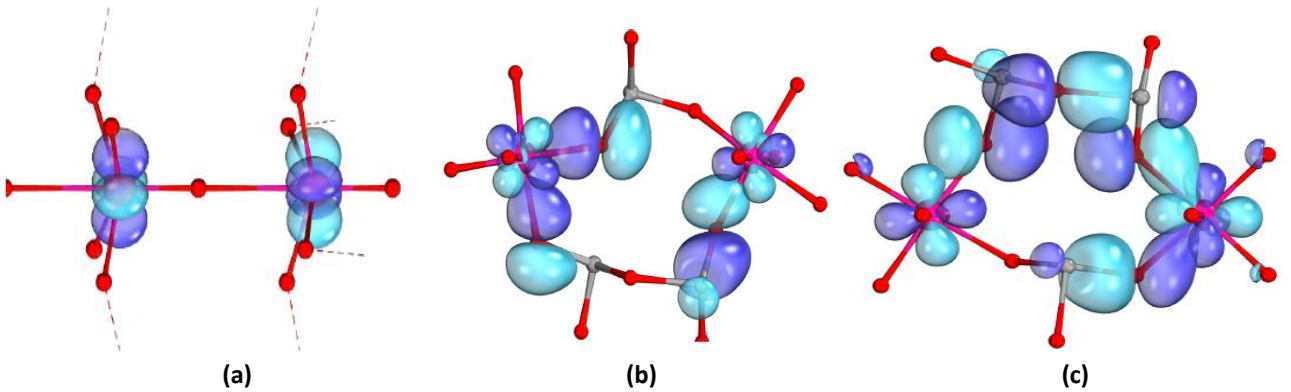
Fig. 3.23: Schematic illustration of (a) J_{1b} (b) J_2 and (c) J_3 orbital distributions and exchange pathways. Only d_{xy} orbital lobes from V^{4+} ions and partial oxygen p orbitals are shown to make the plots brief. The orbital distributions of J_{1a} and J_{1c} are similar to J_{1b}, with a rotation of 4-fold oxygen ligand in the equatorial plane. Oxygen atoms are indicated by red color and selenium atoms are indicated by grey color.

The pitch length of the skyrmion lattice hosted by $VOSe_2O_5$ was measured to be 134 nm at 7.45 K, 25 Oe [26], which is much longer than that in most Bloch-type skyrmion lattice hosted by B20 compounds. Within the Bak-Jensen picture for spiral order in chiral cubic B20 magnets, and assuming a similar concept can apply to

Néel-type spiral order in polar VOSe$_2$O$_5$, this implies that the DMI in this system is rather small, particularly bearing in mind the relatively small size of the determined exchange interactions. QC calculations were performed to evaluate the magnitude of DMI on J_3 where dominant exchange interaction was found. The obtained value of 0.1 meV is less than 5% of J_3 as shown in Table 1. It is unlikely that the DMI with such a small magnitude is responsible for opening the gap in the magnon spectrum, since the energy gap by observation is around 0.5 meV. Moreover, tests using the SpinW software for symmetry-allowed DMIs of different orientations and sizes on the J_3 bond did not result in the opening of the gap. Such a situation can arise if the DMI symmetry commutes with the spin Hamiltonian, that is, the DMI operator and the spin Hamiltonian share the same eigenvalues. In this event, the DMI does not provide additional symmetry breaking beyond exchange interaction and cannot gap the spectrum according to Goldstone theorem [76]. It is therefore reasonable to conclude that DMI is not the origin for the gap in the magnetic ground state of this system. This is again different from Bloch-type skyrmion lattice hosting system Cu$_2$OSeO$_3$, in which DMI is argued to be the origin for the large gap in its magnon spectrum [77].

The fact that the observed gap in the measured magnon spectrum in VOSe$_2$O$_5$ can be reproduced from SpinW simulation by introducing an anisotropy term implies magnetic anisotropy to be the origin for the gap in this system. The size of the anisotropy obtained by fitting the experimental spectrum is 0.52 meV, which agrees rather well with the estimate from DFT calculation (0.67 meV). The microscopic origin of the anisotropy is interpreted as arising due to exchange anisotropy, and additional tests reveal that the energy gap can be reproduced by solely making the J_3 bond anisotropic ($J_{3x} = J_{3y} \neq J_{3z}$) in the SpinW simulation. The overall simulated magnon spectrum in zero magnetic field remains nonetheless identical to the spectrum presented in Fig. 3.21. The anisotropy also features magneto-crystalline anisotropy from the way how it is calculated by DFT. A material is said to have magnetocrystalline anisotropy if it takes more energy to magnetize it in certain directions than in other directions. These directions are usually related to the principal axes (also called easy-axis) of the underlying crystal lattice structure. In a non-Heisenberg model, both exchange anisotropy and magnetocrystalline anisotropy share the same physical principles. In the previous literature, the presence of a complicated interplay between the tetragonal (i.e. in-plane) crystal anisotropy and a thermally varying uniaxial (i.e. Ising like) anisotropy was suggested in this system based on bulk measurements [26]. At the time of writing, further studies are needed to both confirm the origin of the magnetic anisotropy as due to exchange anisotropy and also its microscopic origin. Understanding the anisotropy may even shed light into the delicate competition among various magnetic interactions and the formation of Néel-type skyrmion lattice in this unique tetragonal polar magnet VOSe$_2$O$_5$. For example, this system may confine skyrmion lattice stability to modulate only within particular crystallographic planes or specific directions of external magnetic field. This contrasts strongly with the Bloch-type skyrmion lattice in B20 materials, in which the anisotropy underlying the formation of the equilibrium skyrmion phase is inherently weak, and skyrmion lattice can be stabilized for an arbitrary direction of the magnetic field [29].

We finally suggest a feasible experimental test of the spin Hamiltonian and the interpretation of magnetic anisotropy in VOSe$_2$O$_5$ concluded from this project, by investigating how the magnon spectrum varies when an external magnetic field is applied. Figs. 3.24 and 3.25 show the prediction of the dispersion along the (H 0 0) direction according to SpinW simulation, for a magnetic field of 10 T is applied along the a-axis or c-axis, respectively. The suggested spin Hamiltonian can become more convincing if further data can be obtained in future inelastic neutron scattering experiments with an external magnetic field, and found to agree with these predictions.

In addition, two magnetic anisotropy schemes are compared in the simulated spectra: magnetocrystalline anisotropy in which an anisotropic term D_z is directly inserted (and which is not expected based on physical grounds for S=1/2 V^{4+} magnetism); and exchange anisotropy in which J_3 exhibits different magnitudes along

the c-axis and in a-b plane. Intriguingly, the magnon spectrums are largely similar when the magnetic field is applied along the a-axis (Fig. 3.24); however, there are clear differences in the energy range of each magnon mode when the magnetic field is applied along the c-axis (Fig. 3.25). The results from experiments and simulations without any magnetic field also indicated that no clear difference is present in the spectrum given between these two types anisotropy schemes, which is consistent with H//a results shown in Fig. 3.24. This implies the competition between easy-plane and easy-axis types of anisotropy, as suggested in Ref. [26].
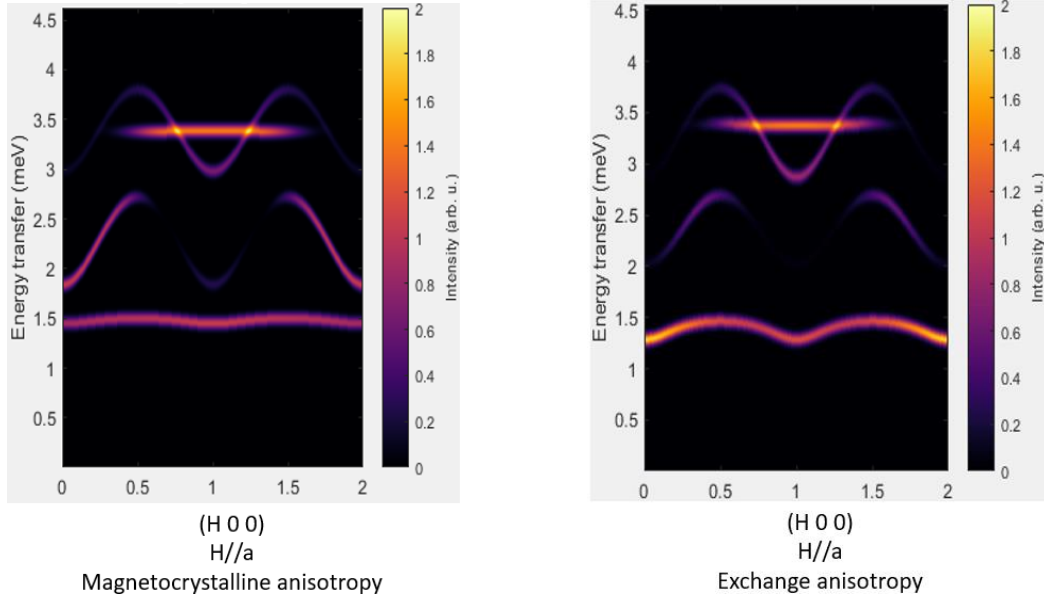
Fig. 3.24: Simulation of magnon spectrum along the (H 0 0) direction with an external magnetic field of 10 T along the a-axis. Two anisotropy schemes are compared: magnetocrystalline anisotropy (left) J_{1a} = -0.01 meV, J_{1b} = -0.07 meV, J_{1c} = -0.18 meV, J_2 = -0.22 meV, J_{3xy} = 2.18 meV, D_z = 0.52 meV; exchange anisotropy (right) J_{1a} = -0.01 meV, J_{1b} = -0.07 meV, J_{1c} = -0.18 meV, J_2 = -0.22 meV, J_{3x} = J_{3y} = 2.18 meV, J_{3z} = 2.7 meV.
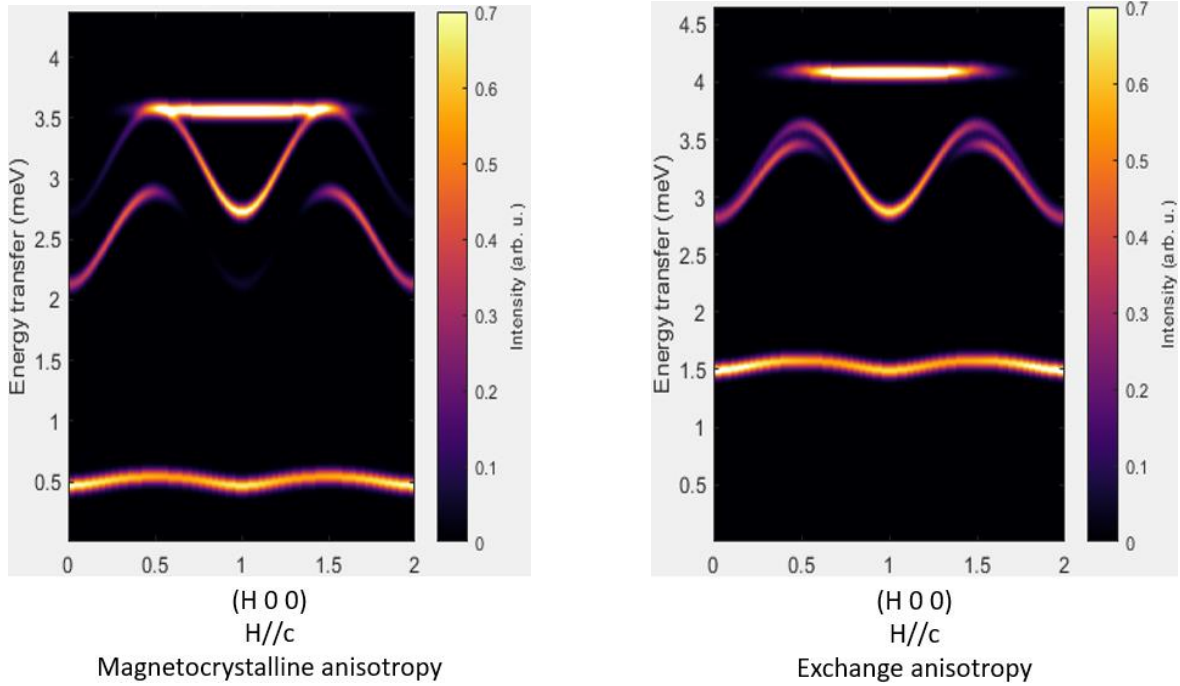
Fig. 3.25: Simulation of magnon spectrum along the (H 0 0) direction with an external magnetic field of 10 T along the c-axis. Two anisotropy schemes are compared as in Fig. 3.24: magnetocrystalline anisotropy (left) and exchange anisotropy (right).

67

Chapter Four: Results – part two: development of radio-frequency pumping system in ultrafast Lorentz Transmission Electron Microscopy

This chapter presents the other component of this thesis work. It consists of the idea, design, implementation, and characterization of the novel RF coherent pumping system in the ultrafast TEM in the Laboratory of Ultrafast Microscopy and Electron Scattering (LUMES), EPFL. The chapter also elaborates on the scientific impacts to be brought by this novel technique, with particular emphasis on the dynamics of skyrmion lattice research. Finally, the limitations of the currently adopted coplanar waveguide (CPW) design and possible ways to improve its performance are discussed.

4.1 Introduction to ultrafast TEM and motivation for the technical development

Since the establishment of TEM in the 1930s, the usage has been focused on acquiring static images from atomic or magnetic structures [78]. The initial pursuit of achieving time-resolved TEM was performed by Prof. O. Bostanjoglo at TU Berlin in the 1980s [79]. However, applications of ultrafast TEM in scientific experiments were not realized until 2005, when the group of Nobel Prize laureate A. H. Zewail (Caltech) made significant improvements to this technique by overcoming various practical difficulties and using advancements in laser technology [80]. After that, ultrafast TEM attracted tremendous interest, and it is currently applied extensively in material science because it allows directly acquiring dynamical information about microscopic structures in real space. Fig. 4.1 shows the basic schematics of an ultrafast TEM, where ultrafast laser pulses [typically UV frequency, nanosecond (ns) to femtosecond (fs) pulse duration] are delivered to the TEM cathode through a window installed in the TEM column, so the photoelectric effect generates ultrafast electron probe pulses. Just above the objective lens, another laser window with an in-column mirror is installed, which allows laser excitation pulses to trigger certain dynamics in the TEM sample. This pulse is called a pump, and its frequency varies depending on the sample's optical absorption and the dynamics being studied. A mechanical stage in the optical pathway is commonly employed to control the delay between pump and probe pulses. By shifting the delay time and acquiring an image at each frame in the dynamical process, the whole dynamics can be constructed. Such a method is also known as the pump-probe technique.
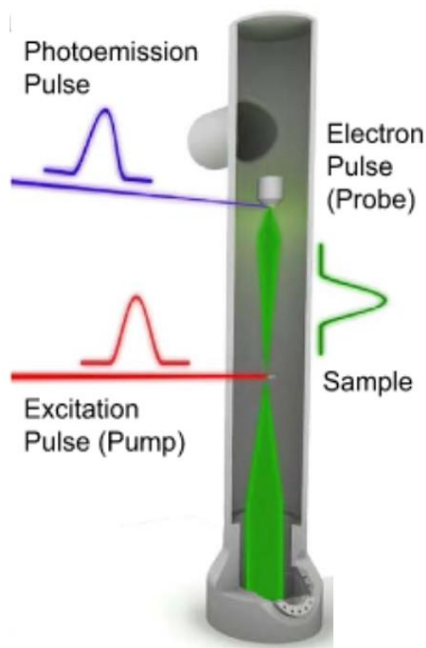
Fig. 4.1: Basic schematics of the setup for an ultrafast TEM. Image reproduced from Ref. [81].

The camera in the TEM acquires and integrates stroboscopic images, so the dynamics being probed must be reversible processes. That is, the sample reverts to the same initial ground state between sample excitation pulses. This allows repeated pump-probe on the sample to accumulate a sufficient amount of electrons (over 10^6) and form an image. The intrinsic frequency of the dynamics in the sample determines the maximum stroboscopic cycle frequency, which is controlled by the repetition rate of ultrafast laser pulses. Irreversible dynamics can be studied by another pump-probe technique called single-shot imaging [82]. However, this thesis only focuses on the stroboscopic imaging technique.

Over the past decade, the main effort in developing ultrafast TEM within the community has been pushing the limit of temporal resolution. This involves the implementation of even shorter and powerful pulsed laser systems alongside the optimization of electron emission (electron gun, Wehnelt, condenser lenses etc.) to enhance the spatial-temporal coherence and brightness of the electron beam. Nowadays, a typical laser based ultrafast TEM can achieve sub-nm spatial resolution and 100 fs temporal resolution. Furthermore, the ongoing development aiming at attosecond resolution is now under active research [83].

Though laser-based ultrafast TEM has become a standard and powerful tool in ultrafast science, it is not suitable to study eigenmodes of collective excitations in solids, such as phonons and magnons. This is because pulsed laser leads to impulsive excitations, whereas the sample needs to be driven coherently by a periodic stimulus to trigger a pure eigenmode. The driving frequency needs to be identical (or at least close) to the eigenfrequency of the dynamical mode being probed. Therefore, the motivation of the second project in this thesis work is to develop a coherent pumping system in an ultrafast TEM, thereby spatially and temporally resolve the collective excitations of Bloch-type skyrmion lattice. The long-term goal is to understand the long-range behaviors of spin waves in skyrmion lattice and their propagation properties around disorders or impurities. Such a technical development significantly impacts the community and may eventually contribute to better design of skyrmion-based spintronic devices in the future.

In chiral magnets, the frequency of collective spin wave excitations in the skyrmion phase (clockwise, anti-clockwise and breathing mode, described in section 1.4) ranges from 1 GHz to 10 GHz [35]. To study these three modes, we developed a novel, coherent pumping system which allows sinusoidal radiofrequency (RF or microwave) modulations on the sample. Fig. 4.2 shows the schematic diagram of this ultrafast TEM setup in LUMES, EPFL, incorporating all essential components. Firstly, the oscillator generates 500 fs infra-red pulses (wavelength 780 nm, average power 0.8 W) at a 80 MHz repetition rate. The pulses are subsequently amplified by employing the Chirp Pulse Amplification technique [84]. The output pulses have an average power of $1 - 2$ W with a repetition rate 1 MHz. Therefore, the energy per pulse increases by two orders of magnitude after amplification. High energy pulses are converted to UV frequency and stretched to picosecond (ps) regime before they strike the cathode to produce photoelectron pulses. Here, ps pulses are chosen because they still provide sufficient temporal resolution to the GHz dynamics of skyrmion lattice, while pulses with longer duration contain larger amounts of electrons. As a result, the acquisition time becomes shorter, so adverse effects from sample drift or TEM instability can be minimized.

The RF signal is delivered to the sample through a customized sample holder fully designed, manufactured and assembled at EPFL. In addition, a phase-locking loop that synchronizes electron pulses and microwave signal is introduced. These are the key developments in this thesis work, and the details are presented in section 4.2 and 4.3. The schematics of the pump-probe technique using a microwave pump is illustrated in Fig. 4.3. A clear difference is that laser-based pump-probe requires finding time zero – the moment when the dynamic begins is probed; whereas in microwave-based pump-probe, electron pulses constantly probe the sample at fixed phase shift relative to the microwave signal. The dynamics is constructed by varying the phase locking position. For this reason, such a novel scheme is also called "clocked" pump-probe.
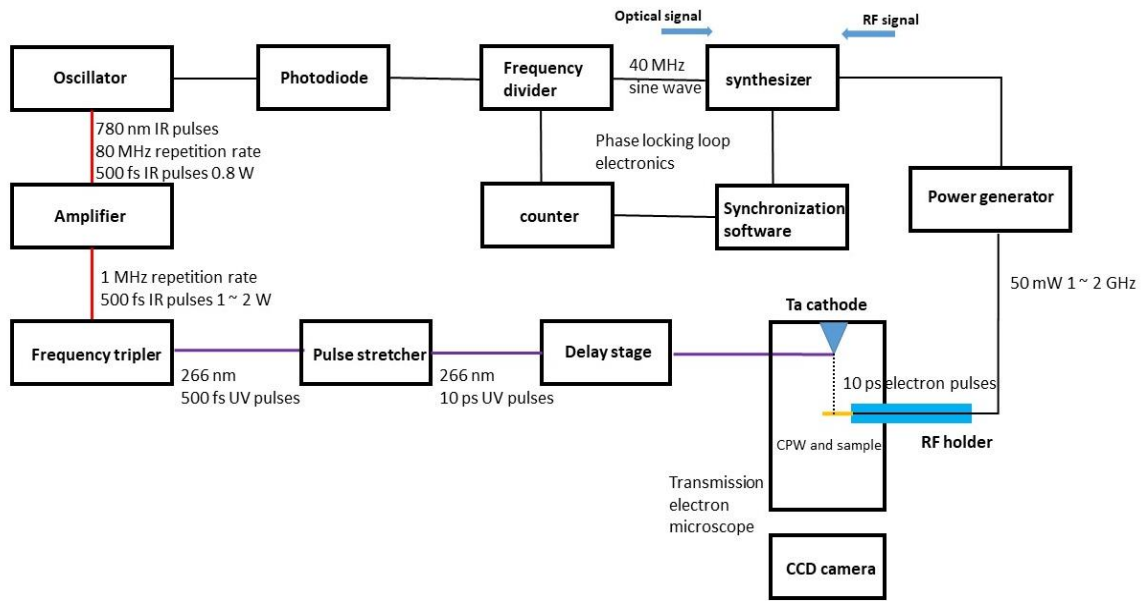
Fig. 4.2: Schematic diagram of the ultrafast TEM setup with the RF pumping system in LUMES.
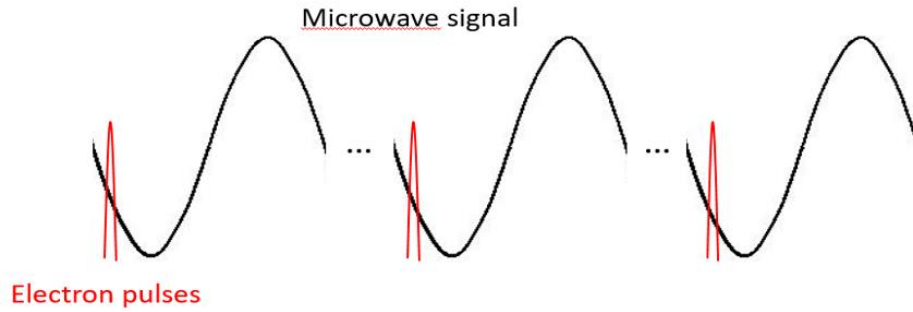
Fig. 4.3: Schematic illustration of the "clocked" pump-probe experiment allowed by the developed RF pumping system integrated into the ultrafast TEM in LUMES.

4.2 RF sample holder

This section presents in detail the customized RF sample holder developed at EPFL, which is mechanically and electronically compatible with the ultrafast TEM located at LUMES. Three main components of the holder are introduced separately: overall mechanical and electrical design, printed circuit board (PCB) and coplanar waveguide (CPW) on a microchip. The end of the section shows results obtained from the characterization of impedance matching and power loss done by time domain reflectometry (TDR), indicating low-loss RF transmission through this holder.

4.2.1 Overall holder design

The main body of the RF sample holder resembles the standard, commercial single-tilt beryllium holder for the JEOL-2100 TEM at LMUES, and a photo of the latter is provided in Fig. 4.4 (a). The difference is in the interior of the RF holder where a coaxial cable with a maximum operating frequency of 18 GHz [Fig. 4.4 (c)] passes through. The length of the coaxial cable matches the length of the rod. One terminal of the coaxial cable connects to the external RF power supply, while the other terminal connects to a PCB which replaces the plate retainer on the standard single-tilt holder. The CAD drawing showing the schematics of the RF holder is presented in Fig. 4.4 (b).

(a)
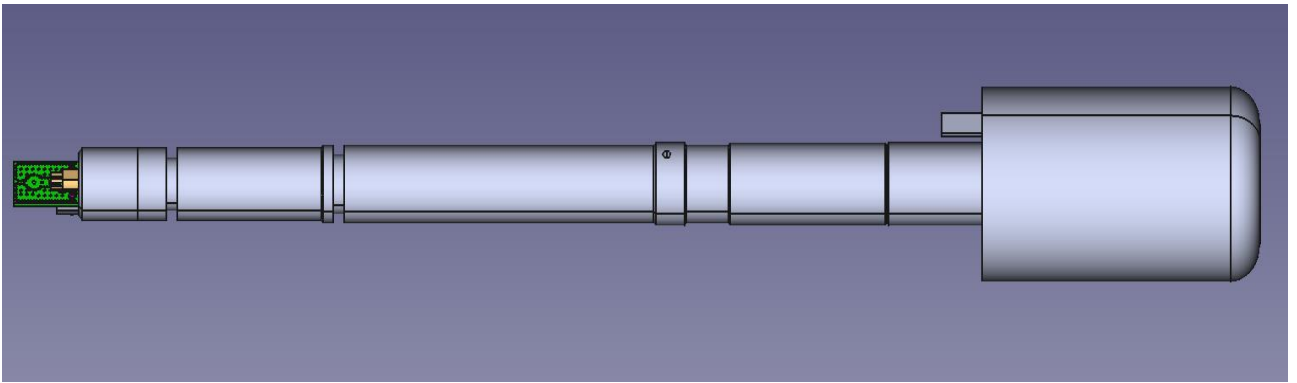
(b)

(c)

(d)
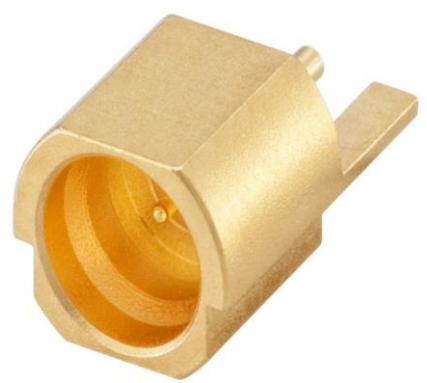
(e)

Fig. 4.4: (a) A photo of the standard, commercial single-tilt sample holder for JEOL-2100 TEM; (b) CAD drawing of the RF sample holder designed at EPFL; (c) – (e) photos of the coaxial cable, hermetically sealed connector and PCB connector, respectively.

To ensure vacuum compatibility to the TEM, a special hermetically sealed connector [Fig. 4.4 (d)] is employed to bridge the interior coaxial cable and the exterior PCB, so that the air leakage through the interior of the RF holder is minimized. The vacuum level in the TEM column can reach 1.6×10^{-4} Pa, which is the same order of magnitude when the standard single-tilt holder is inserted (typically 1×10^{-4} Pa). The transmission of RF signal from the coaxial cable to a PCB is realized by a special PCB connector [Fig. 4.4 (e)]. All electrical units have 50 Ω impedance to suppress power loss during transmission. A photo of the product RF holder is shown in Fig. 4.5. The manufacturing work was contributed by Mr. Olivier Haldimann at the mechanical workshop, Institute of Physics, EPFL.
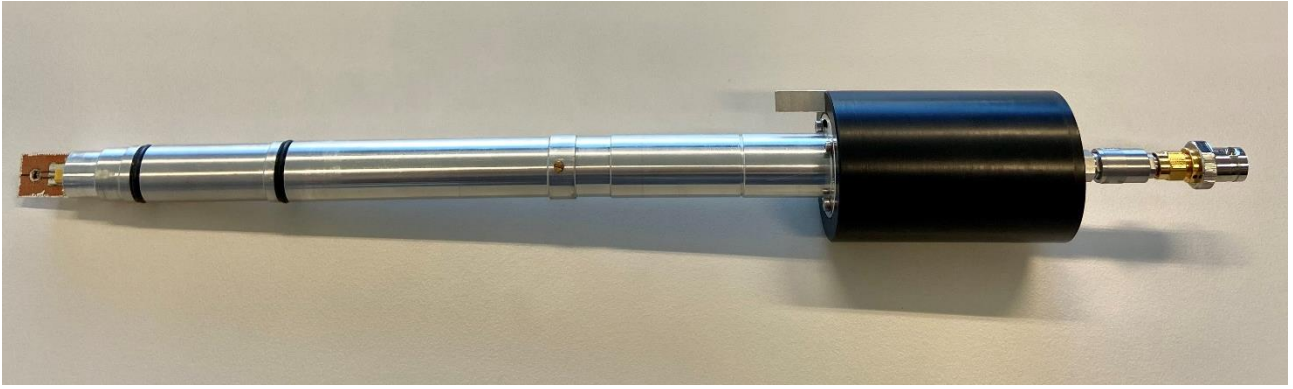
Fig. 4.5: A photo of the RF holder manufactured at the Institute of Physics, EPFL.

4.2.2 Printed circuit board

A PCB was employed to transmit the RF signal after the coaxial cable and host the sample carrying chip. Fig. 4.6 shows the schematic design of the PCB as part of the RF holder. The overall dimension of 17.5×12.5 mm^2 is identical to that of the standard single-tilt holder to ensure mechanical compatibility with the TEM. The PCB is made of FR4 (flame retardant epoxy resin, 0.8 mm thickness) material with a single layer of copper (35 µm thickness). The copper coating layer contains two gap lines of 0.5 mm width and 1.3 mm separation. The central signal line of the connector is soldered to the region between these two gap lines, while two ground lines of the connector are soldered outside this region. The signal line and ground regions are also indicated in Fig. 4.6. In addition, there is a semi-through hole of 3 mm diameter, 0.3 mm depth, and a through hole of 1 mm, which are concentric and the center is 12 mm away from the left edge of the PCB. This design allows the chip (2×2 mm^2, 0.2 mm thick) to sit in this cavity stably while maintaining a similar height to the copper surface of the PCB. As a consequence, wire bonding from the PCB to the chip becomes more convenient. The inner through hole is aligned with the electron-transparent membrane on the chip window as well as the electron beam. Its position on the PCB is the same as the hole in the plate retainer of the standard single-tilt holder. The chip layout and wire bonding details are presented in the next section. Near the left edge, there are two additional through holes for screws to fix the PCB to the RF holder.
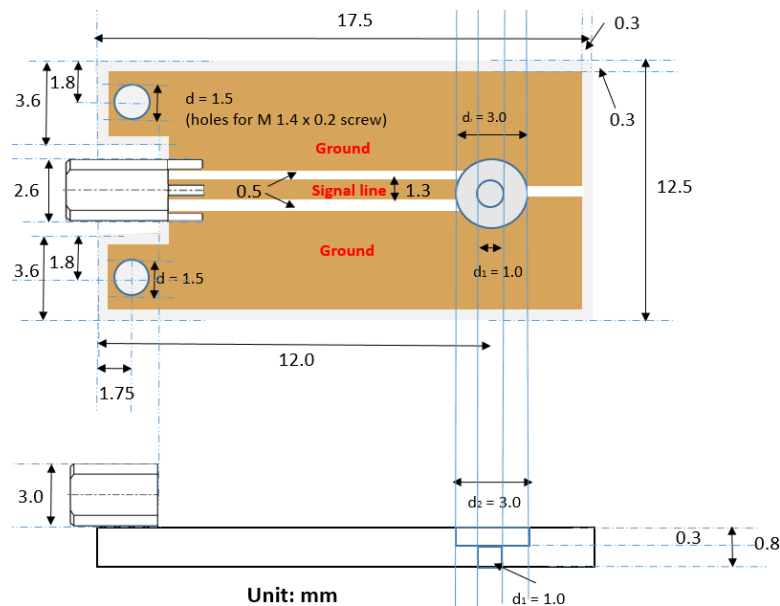
Fig. 4.6: Schematic design of the PCB. Top panel: top view; bottom panel: side view.

Fig. 4.7 (a) provides the CAD drawing of the PCB design. Here, we proposed to drill many small through holes in ground regions to suppress parasitic modes. A photo of the final product is shown in Fig. 4.7 (b), where a microchip sits in the cavity. The edges of the PCB are afterwards painted by silver epoxy to avoid charging effect from the electron beam of the TEM. The overall PCB has 50 Ω impedance matched with the RF holder. Such a PCB design has been proven to be more effective in controlling damping and parasitic modes than that in the other RF holder for TEM concurrently developed in Brookhaven National Laboratory, USA. [85] The manufacture of the PCB and relevant soldering work were contributed by Mr. Peter Brühlmeier and Mr. Barblan Jean-Marie at the PCB workshop, EPFL.

(a)   (b)
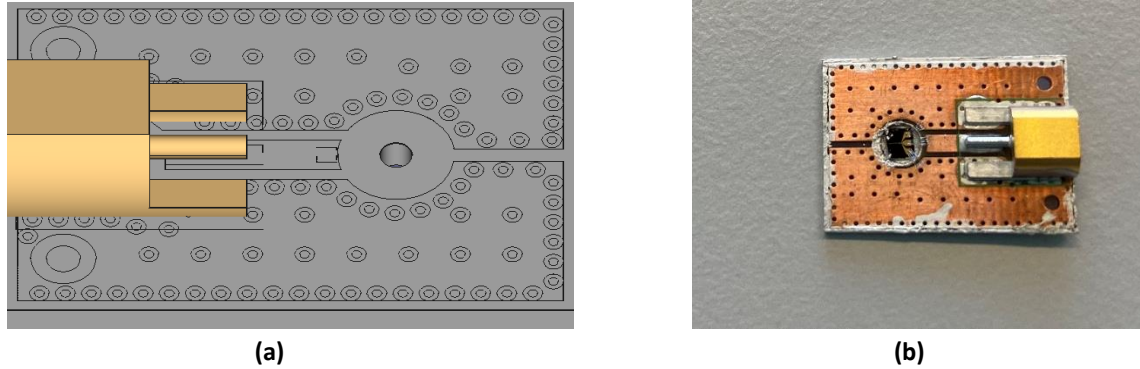
Fig. 4.7: (a) CAD drawing and (b) final product of the PCB.

4.2.3   Microchip and coplanar waveguide

Instead of the standard omniprobe TEM grid introduced in section 2.3.1, in this project, we used a microchip with an electron-transparent membrane, allowing the micro-fabrication of electric circuits on top and the generation of RF environment around the sample. Fig. 4.8 provides a schematic sketch and a photo of the commercially available SiRN (silicon-rich nitride) membranes with a silicon substrate. The whole frame consists of 3×3 arrays of 2×2 mm^2 sub-frames. The dimension of the whole frame is 10×10 mm^2 which is suitable for the photolithography technique. Micro-fabrication processes are repeated over all the 9 sub-frames. After that, the whole frame is fractured to break out into 9 microchips. The height of the substrate is 0.2 mm; the membrane has dimension of 100×100 μm^2 over the window and a thickness of 50 nm.

(a)   (b)
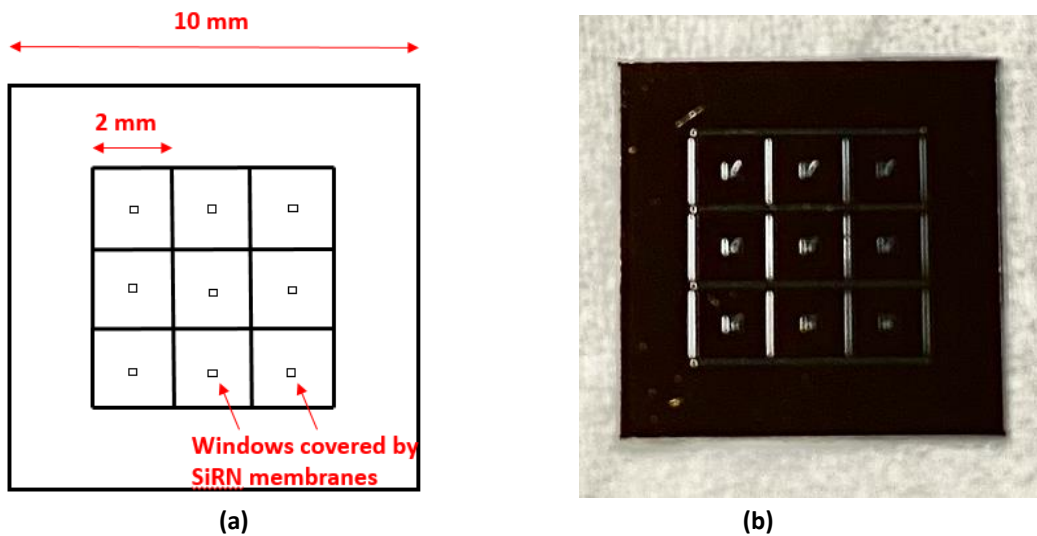
Fig. 4.8: (a) A schematic sketch of the SiRN membrane coated over Si substrate; (b) a photo of the commercial product.

CPW was chosen because it can produce extremely high-frequency responses with suppressed parasitic RF modes [86]. This advantage is in line with the scientific goal of developing this technique, namely, resolving the collective spin wave dynamics in skyrmion lattice where coherently pumping a single mode is desired. A CPW circuit was microfabricated on a SiRN membrane by photolithography. Fig. 4.9 shows the laser exposure pattern indicating the schematic design of the device. The drawing is done by the Klayout software. On the left of the pattern, there are three large pads of 400×400 nm^2. They provide wired-bonding areas which bridge the CPW to the PCB after the fabrication processes are complete. The central pad is bonded to the signal line and the top/bottom pads are bonded to the ground regions of the PCB. Three parallel transmission lines run over the membrane, where the skyrmion lattice hosting sample sits on top of them.

Since the RF holder operates at 1 GHz – 18 GHz range, the wavelength of microwave falls into the 10 mm – 100 mm regime, much longer than the overall dimension of the device. It is reasonable to assume that the CPW works in the quasi-static limit, in which the amplitude of the RF signal along the transmission lines of the device is constant [86]. Therefore, the sample experiences excitations due to sinusoidal AC magnetic field depending on the location with respect to the signal line and ground lines: in-plane field directly above all three lines and out-of-plane in the gaps between the signal line and two ground lines (full field configuration is shown in Fig. 1.8 of section 1.4). By carefully tuning the RF frequency to match the eigenfrequency of a magnon mode in the skyrmion phase of the hosting material, and choosing a suitable power, the pumping system can coherently drive the breathing mode or clockwise/anti-clockwise mode at a single frequency. In the meantime, the magnitude of the AC magnetic field can be roughly estimated by the Biot-Savart law:

$$B = \frac{\mu_0 I}{2L} \tag{4.1}$$

where μ_0 is vacuum permeability, I is magnitude of the current in the circuit, and L is the distance to the middle of the wire. The current (I) is related to the external RF power (P) by a simple formula:

$$P = IZ^2 \tag{4.2}$$

where Z is the impedance. In the quasi-static limit, the impedance of the CPW can be calculated by viewing the device as three resistors connected in parallel. The length (900 µm), line width (4 µm) and height (160 nm) were chosen to make the impedance 50 Ω matched with the PCB and RF holder. The gap width was designed to be small (3 µm) to enhance the amplitude of the AC magnetic field produced near the signal line. To estimate the RF power needed to drive the collective excitation modes in skyrmion lattice, we adopted the magnetic field of 1.7 mT in the calculation of breathing mode in Ref. [32]. By substituting this value into Equations (4.1) and (4.2), the power needed is 50 mW for the current design.

(a) **(b)**
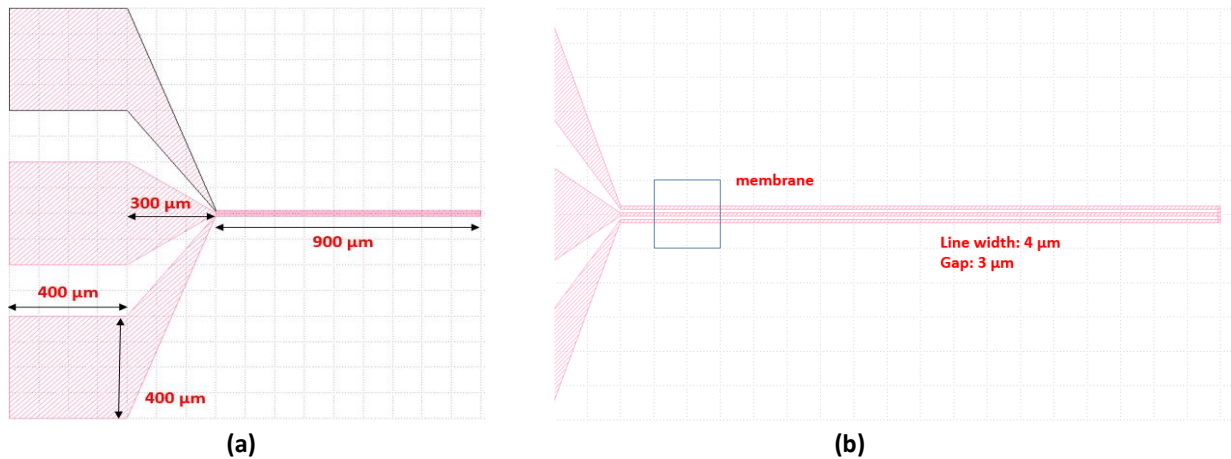
Fig. 4.9: Schematic design of the CPW circuit. (b) is a zoom-in view of (a), where the membrane location is indicated.

The photolithography procedures are schematically illustrated in Fig. 4.10: firstly, photoresist LOR 5A and AZ1512 (positive) are spin coated on top of the SiRN membrane. This creates a 0.4 μm LOR 5A layer and a 1.0 μm AZ1512 layer. Subsequently, a maskless laser aligner (MLA150) was employed to directly expose the pre-designed pattern [Fig. 4.9 (a)] onto the photoresist. By performing a series of tests, the optimal exposure condition was found to be 42 mJ/cm^2 dose with zero defocus. After that, the exposed regions are removed by AZ-726-MIF developer due to the positive nature of AZ1512. Then, the SiRN membrane is evaporated by gold nanoparticles (LAB600H), allowing the deposition of a 160 nm thick layer on both the membrane and the rest of the photoresist. In addition, there is a 16 nm chromium layer below gold deposition for better adhesion, and a 10 nm SiO$_2$ insulating layer above gold deposition to prevent an electric short in the circuit when a metallic sample is studied. Finally, the rest of the photoresist is removed by lift-off procedure using Microposit remover 1165, leaving gold wires on top of the membrane. The photolithography work was accomplished in the cleanroom at the Center of MicroNanoTechnology (CMi), EPFL.
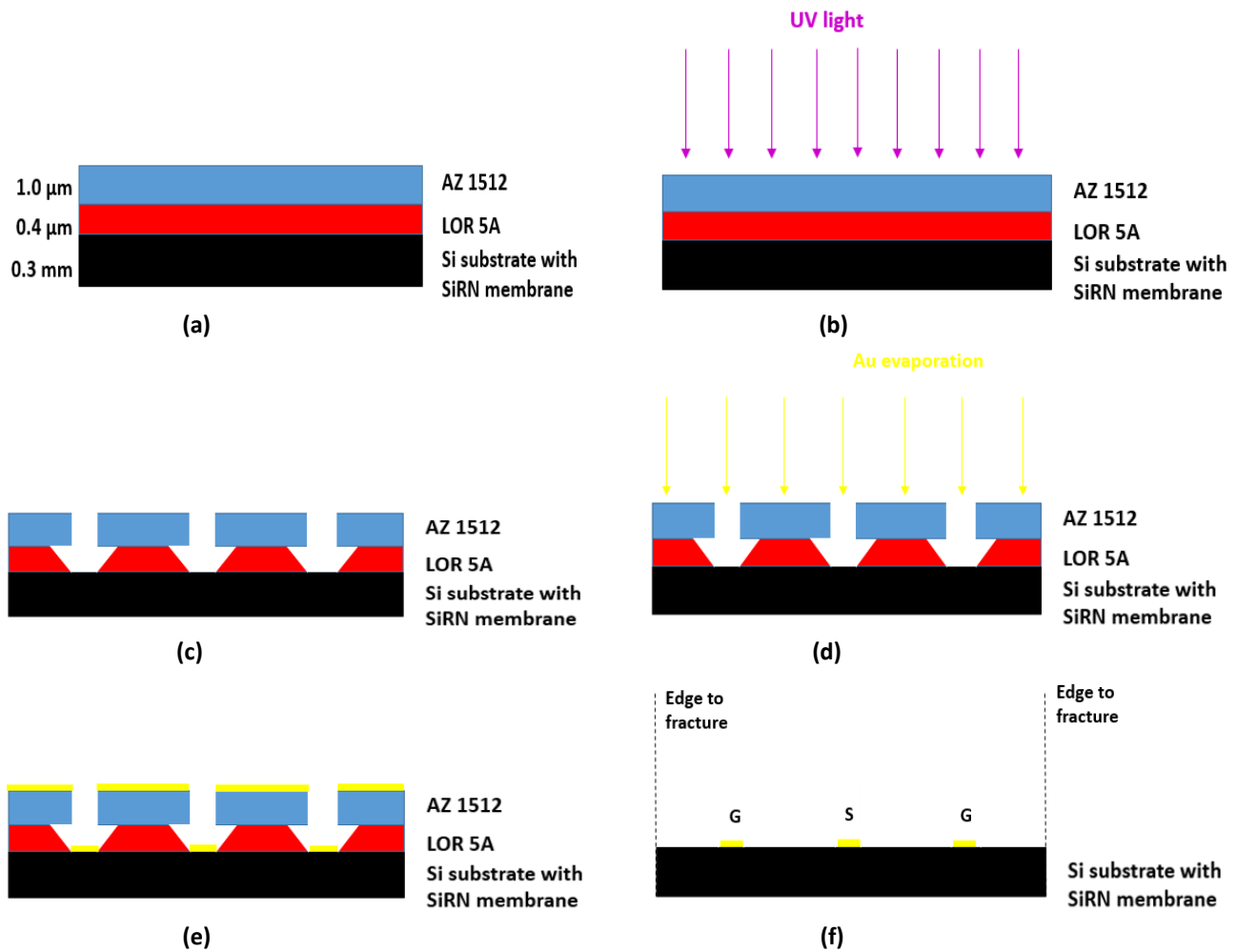
Fig. 4.10: Process flow of photolithography using double layer resist and direct laser exposure. (a) spin coating; (b) UV exposure; (c) developing; (d) (e) gold evaporation; (f) lift-off, leaving signal line (S) and ground lines (G) on the membrane.

Finally, the fabricated microchip was wired bonded to the PCB using aluminum bonding wires. Several parallel bonding wires were used on each pad to minimize the power loss due to impedance mismatch when the current flows through bonding wires. The microchip was placed in the cavity of the PCB and fixed with silver epoxy paint. Fig. 4.11 shows images of the device from a scanning electron microscope (SEM). The line width and gap distance obtained from fabrication were measured to be 4.1 μm and 3.4 μm, respectively. The wire bonding job was contributed by Mr. Adrien Toros at the Center of MicroNanoTechnology (CMi), EPFL.
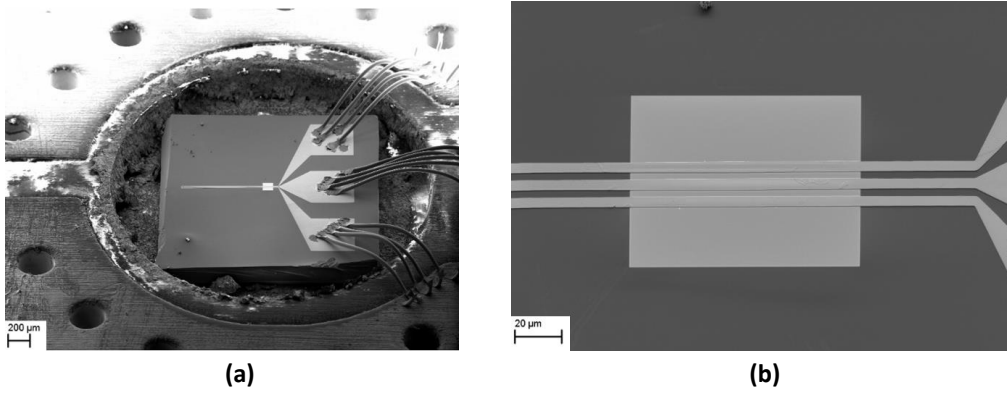
Fig. 4.11: SEM images of the microchip with the CPW sitting in the cavity of the PCB. Image (a) contains bonding wires; image (b) is a zoom-in view of the membrane.

4.2.4 Time domain reflectometry and excitation profile

After all components of the RF holder were manufactured and assembled, a TDR experiment was performed to test the impedance and power transmission of the whole system. This technique generates a square wave pulse (296 mV amplitude in this test) and subsequently measures the reflection that results from the RF signal traveling through a transmission line [87]. Three tests were run separately: cable only; cable and PCB; cable, PCB and CPW. In addition, measurements with an open circuit (denoted as open) and with a 50 Ω resistor (denoted as load) were performed to provide comparisons. The experimental work was contributed by Dr. Sho Watanabe at the Laboratory of Nanoscale Magnetic Materials and Magnonics (LMGN), EPFL.
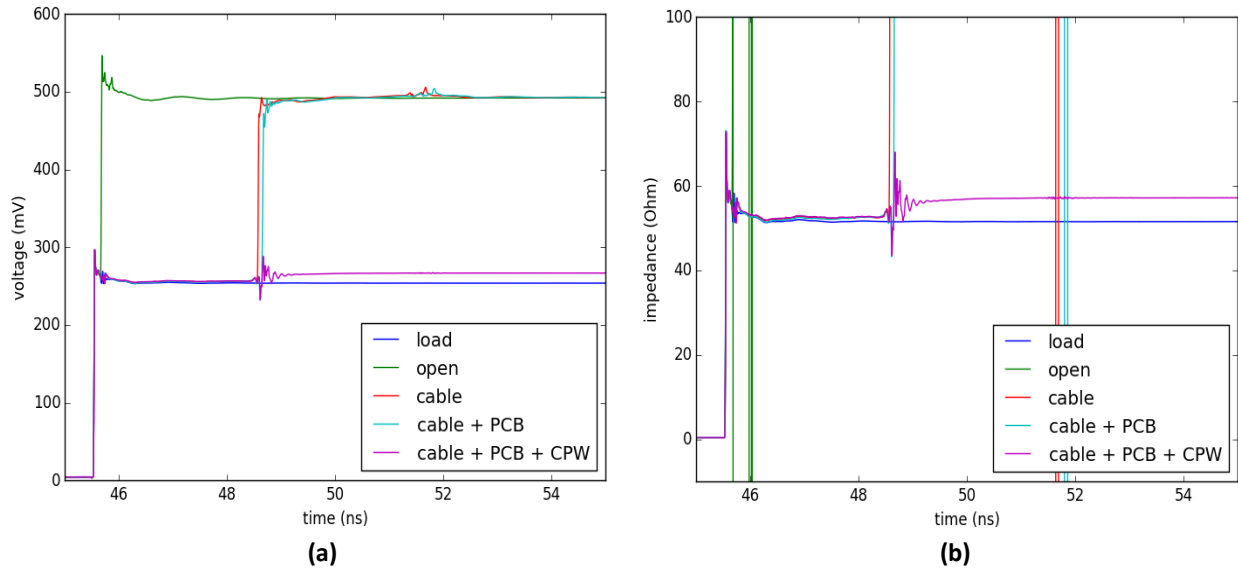
Fig. 4.12: Results from TDR tests showing (a) voltage and (b) impedance against time. Load represents a test with a standard 50 Ω resistor; open represents an open circuit.

The measured voltage and impedance against time are plotted in Fig. 4.12. It is clear that upon connecting the CPW, the voltage drops down to 266 mV, and the impedance of the RF holder system becomes around 57 Ω. Therefore, the transmission rate α can be estimated by:

$$\alpha = \frac{P_1}{P2} = \frac{V_1^2}{V_2^2} \tag{4.3}$$

where V_1 and V_2 are the voltages of the transmitted signal and applied signal, respectively. The transmission rate by calculation is 81%, which indicates that the RF signal propagates efficiently and delivers to the

microchip with reasonably low loss. Note that the transmission measured by TDR represents the average transmission rate of all frequencies up to a cut-off since a square pulse is applied.

Though the CPW designed in this thesis work is expected to operate in the quasi-static limit, its field distribution and excitation profile were studied by comparing it with a similar CPW design in Ref. [88], which also operates from a few to tens GHz regime. The performance of the CPW in this reference was modeled by Finite-Element simulations. A summary of comparisons between two CPWs is listed in Table 2.

CPW	Material	w_s (µm)	w_g (µm)	w_{sg} (µm)	t (µm)	L (µm)	Frequency range (GHz)
This thesis	SiO$_2$/Au/Cr/SiRN/Si	4	3	4	0.16	900	0 ~ 18
Ref. [88]	Au/Cr/GaAs	3	3	3	0.12	400	0.5 ~ 26.5

Table 2: Comparison of materials and dimensions between the CPW designed in this thesis work and the CPW in Ref. [88]. Here, w_s, w_g and w_{sg} represent signal line width, ground line width and gap distance, respectively; t is the thickness of gold deposition and L is the length.

Fig. 4.13 (a) shows simulated magnetic field distribution around the CPW in Ref. [88] by setting the microwave power at 1 mW and assuming 50 Ω impedance. The field distribution is as expected, namely, in-plane above the signal line and ground lines and out-of-plane in the gaps. A surprising result is that the field amplitude at 26.5 GHz is almost ten times stronger than that at 2 GHz, for both in-plane and out-of-plane components. The origin of this field enhancement with frequency is still unknown, according to Ref. [88]. The wavevector distribution of the RF signal in the CPW was also simulated, which is the Fourier transform of the amplitude profile. Fig. 4.14 (b) shows the results up to 8 µm^{-1}. The dominant excitation lies close to zero wavevector, and its amplitude is approximately five times higher than the secondary signal at around 2.6 µm^{-1}. Since the three collective excitation modes in skyrmion lattice feature static (or non-propagating) spin waves with zero wavevector, this result further supports that a CPW design may be suitable for resolving these dynamics by TEM in real space.
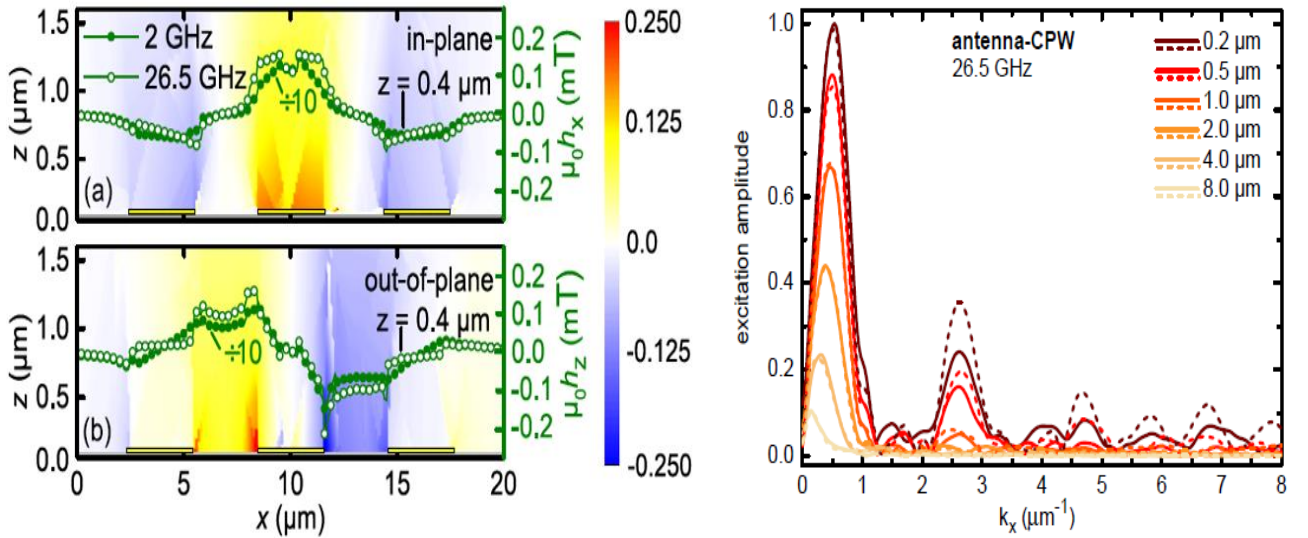
Fig. 4.13: (a) Near field amplitude profile of the CPW in Ref. [88]. Two cuts at a constant height of 0.4 µm with frequencies of 2 GHz and 26.5 GHz are taken. Top and bottom panels correspond to in-plane and out-of-plane components, respectively; (b) wavevector distribution at 26.5 GHz of the CPW in Ref. [88], at different heights above the CPW from 0.2 µm to 8 µm. Solid and dashed lines represent in-plane and out-of-plane components, respectively. Images reproduced from Ref. [88].

4.3 Overview of synchronization instruments

The other key ingredient in the RF coherent pumping system is the phase-locking loop which synchronizes the probing electron pulses and the driving RF signal. The detailed schematic diagram of this setup is shown in Figure 4.14, corresponding to the top right part of Fig. 4.2 in the whole RF pumping system. This phase-locking loop is designed and implemented by the BSW TestSystems & Consulting company.

Firstly, a photodiode is employed to convert the pulsed laser signal from the oscillator into square waves, which are then filtered and amplified to produce a sinusoidal RF signal at around 80 MHz frequency. The frequency of this RF signal is divided by a factor of two using a prescaler module [Fig. 4.15 (a)], and it delivers two buffered 40 MHz outputs with good phase noise control. One output signal is read by a universal frequency counter [Fig. 4.15 (b), top], which gives a high precision frequency trigger input for the waveform microwave synthesizer unit [Fig. 4.15 (b), bottom]. The computer synchronization software monitors the oscillator's frequency and sets the output waveform frequency in the synthesizer from 1 MHz to 20 GHz. The set frequency must be an integer multiple of the divided frequency of the signal from the counter unit (around 40 MHz) to the precision of 1 Hz. Otherwise, the electron pulses would wander temporally with respect to the phase of the RF signal applied to the CPW microchips (this is called temporal jittering). With this phase-locking loop, the synthesizer can generate sinusoidal RF signals as the power source to the RF holder, where electron pulses are always at a fixed phase relative to the RF signal. The phase noise in this system is controlled within 200 fs which can be stable for hours. It is sufficient for performing clocked pump-probe experiments to study the collective magnon modes in skyrmion lattice hosting materials with ps temporal resolution. An additional DC power supply powers the RF amplifier and prescaler. Finally, a DC block is placed at the output of the synthesizer to prevent reflected DC signals produced by the electron beam from damaging the equipment.
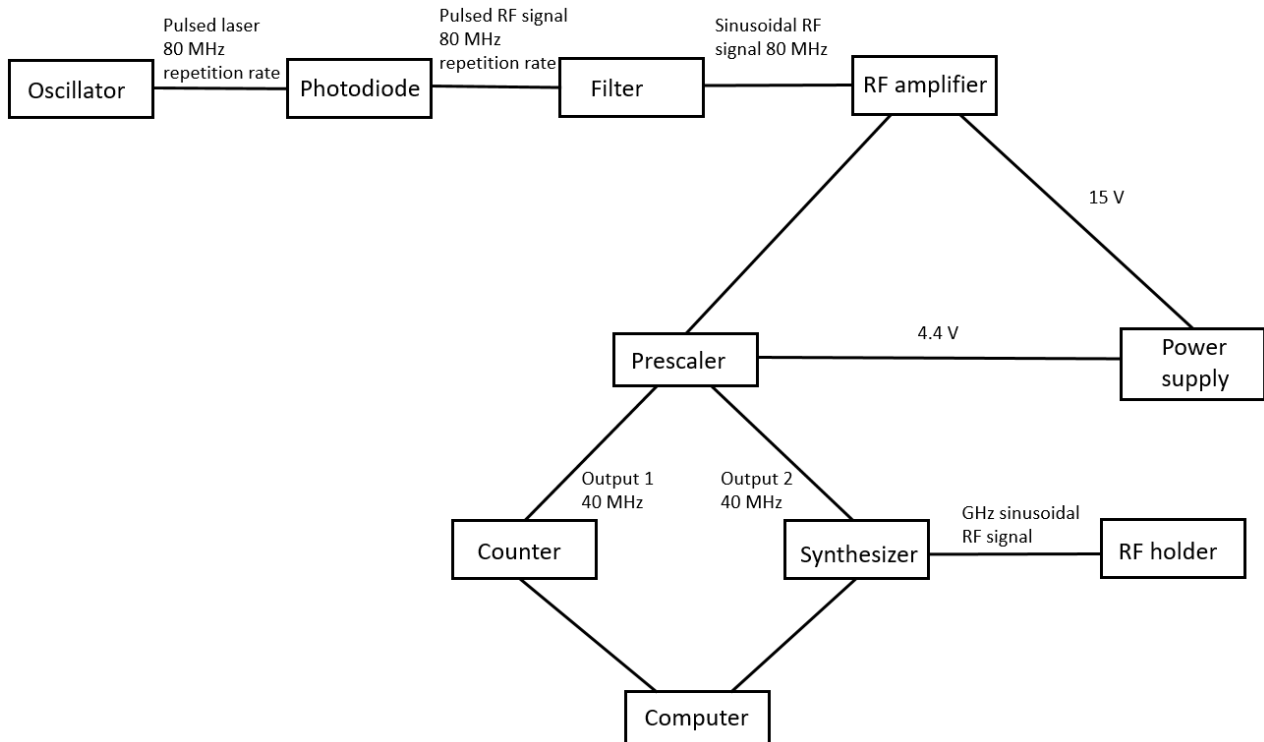
Fig. 4.14: Detailed schematic diagram of the phase-locking loop and synchronization instruments.

Fig. 4.15: Photos of (a) the prescaler; (b) the counter (top) and synthesizer (bottom) in the phase-locking loop.

4.4 Study of candidate materials and description of experiments

The RF sample holder for TEM developed at EPFL can only operate at room temperature. As the first attempt to spatial-temporally resolve the collective magnon modes of Bloch-type skyrmion lattice, a chiral hosting material is desired at or slightly above room temperature. Here, the heating effect from the CPW upon applying the RF power is considered. After an exhaustive review of all bulk hosting systems, the β-Mn-type Co-Zn-Mn alloys are considered the most promising candidates for these experiments. According to Ref. [31], their skyrmion phase pockets in the phase diagram vary by composition, and in specific compositions, they can extend to room temperature or even above.

Fig. 4.16 (d) shows the DC magnetization measurements versus temperature at a constant magnetic field of 20 Oe, indicating the Curie temperature of each composition [31]. We can learn that both $Co_8Zn_8Mn_4$ and $Co_8Zn_9Mn_3$ host equilibrium skyrmion phase near room temperature (approximately from 290 K to 310 K). Moreover, the skyrmion phase in $Co_8Zn_{10}Mn_2$ and $Co_9Zn_9Mn_2$ persists even above room temperature, up to around 370 K and 420 K, respectively. Though the Curie temperature of $Co_{10}Zn_{10}$ is also higher than room temperature, this composition does not host skyrmion lattice (only the helical state is present). For a CPW of dimensions introduced in Section 4.2.3, the local temperature at the SiRN membrane increases by roughly 30 K – 50 K when a microwave of 25 mW – 75 mW power is applied, which is the estimated power to drive collective magnon dynamics of skyrmion lattice according to Ref. [32]. There are additional sources of heating effect such as the electron beam, electrical units in the microscope etc. Consequently, $Co_8Zn_{10}Mn_2$ and $Co_9Zn_9Mn_2$ are the most suitable candidates since they can host skyrmion lattice at room temperature under microwave and TEM environments.

Through external collaborations, a high-quality $Co_8Zn_{10}Mn_2$ single crystal lamella was provided by Dr. Valerio Scagnoli, Mesoscopic Systems Group, at PSI. The skyrmion lattice and phase diagram from room temperature to 355 K in this sample were studied by LTEM. A standard single-tilt sample holder with temperature control device was employed. Fig. 4.16 (a) and (b) are two LTEM images obtained at 298 K and 355 K, respectively, with an external magnetic field of 75 mT. A clear hexagonal arrangement of skyrmions can be seen at 298 K, while the magnetic contrast becomes weaker on the approach to the phase boundary, the skyrmion lattice is still visible at 355 K. The skyrmion phase was created by firstly zero-field warming from above the Curie

temperature, slowly cooling down, and then applying an external magnetic field. The resulted state is called the metastable skyrmion state [31], which is considered more ideal for time-resolved experiments than the equilibrium skyrmion lattice phase due to the enhanced stability.
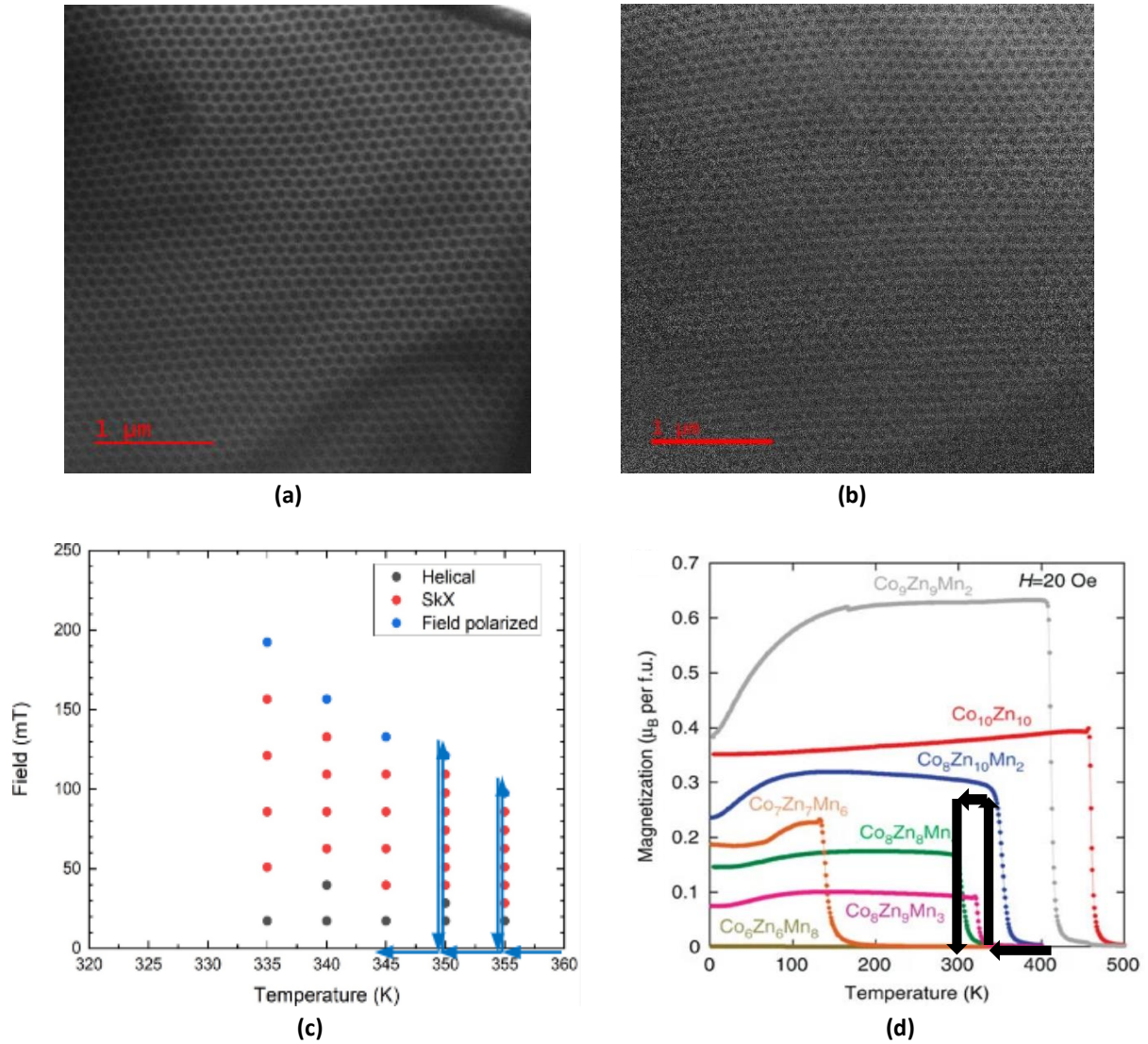
Fig. 4.16: LTEM images of a Co$_8$Zn$_{10}$Mn$_2$ lamella taken at (a) 298 K and 75 mT; (b) 355 K and 75 mT; sample is provided by Dr. Valerio Scagnoli at PSI; (c) phase diagram characterized in LTEM by zero-field cooling and subsequently sweeping the external magnetic field; (d) Magnetization at a constant magnetic field (20 Oe) against temperature for β-Mn-type Co-Zn-Mn alloys, indicating the Curie temperature of each composition; image reproduced from Ref. [31].

The phase diagram of this particular sample between 335 K and 355 K was characterized by a series of zero-field cooling procedures followed by magnetic field scans. The metastable skyrmion phase was found to be present in a wide range of temperatures and magnetic fields, as displayed in Fig. 4.16 (c). The metastable skyrmion lattice in the phase diagram covers the temperature range that our RF sample holder can reach including heating effect from microwave propagation and electron beam. These results indicate that suitable candidates of skyrmion lattice hosting systems exist in the nature, and high-quality samples are accessible for the long-term goals in the scientific aspects of this technical development. Note that the metastable skyrmion phase cannot be directly reached in this RF holder because no temperature control is available, and ex-situ generation (outside the microscope) procedures are required. More advanced RF sample holders for TEM with built-in cryogenic devices allowing continuous, steady helium flow cycles is currently being developed in several companies, while the progress is still in early stages at the time of this thesis.

The detailed procedures of the proposed experiment aiming at spatial-temporally resolving the breathing mode dynamics in the metastable skyrmion lattice of the $Co_8Zn_{10}Mn_2$ lamella using the RF sample holder developed in this thesis are the following: firstly, adjust the prism-based UV pulse stretcher and obtain laser pulses of around 10 ps duration and 1 MHz repetition rate from the chirp pulse amplifier; after that, align the laser pulses to the TEM cathode so that ps electron pulses are produced, and optimize TEM imaging condition at this pulse duration using a test sample (e.g. Fe_3O_4 magnetite). In terms of sample preparation, transfer the $Co_8Zn_{10}Mn_2$ lamella to the CPW microchip where the region with skyrmion lattice sits at the gap between the signal line and ground lines; then mount the CPW microchip to the PCB and carefully wire bond the PCB to the CPW electrode pads. To obtain metastable skyrmion lattice ex-situ, firstly heat the sample to 420 K in an oven; gradually cool down to 350 K and apply an external magnetic field of 75 mT by an electromagnet which is out-of-plane with respect to the sample; release the magnetic field and naturally let the sample cool down to room temperature [indicated by arrows in Fig. 4.16 (d)]. Next, mount the PCB to the RF sample holder, and insert the sample holder to the TEM; choose an integer number that is the rounded quotient between the resonant frequency of the breathing mode in $Co_8Zn_{10}Mn_2$ and 40 MHz, while the resonant frequency can be measured by microwave absorption spectroscopy or Brillouin light scattering. Lastly, input this integer number to the phase locking loop and turn on the synthesizer so that RF signal synchronized to electron pulses is applied, allowing clocked pump-probe imaging; scan the mechanical stage and repeat imaging at different phase shift with respect to sinusoidal RF signal, and by covering one full period the entire breathing mode dynamics can be constructed.

(a)   (b)
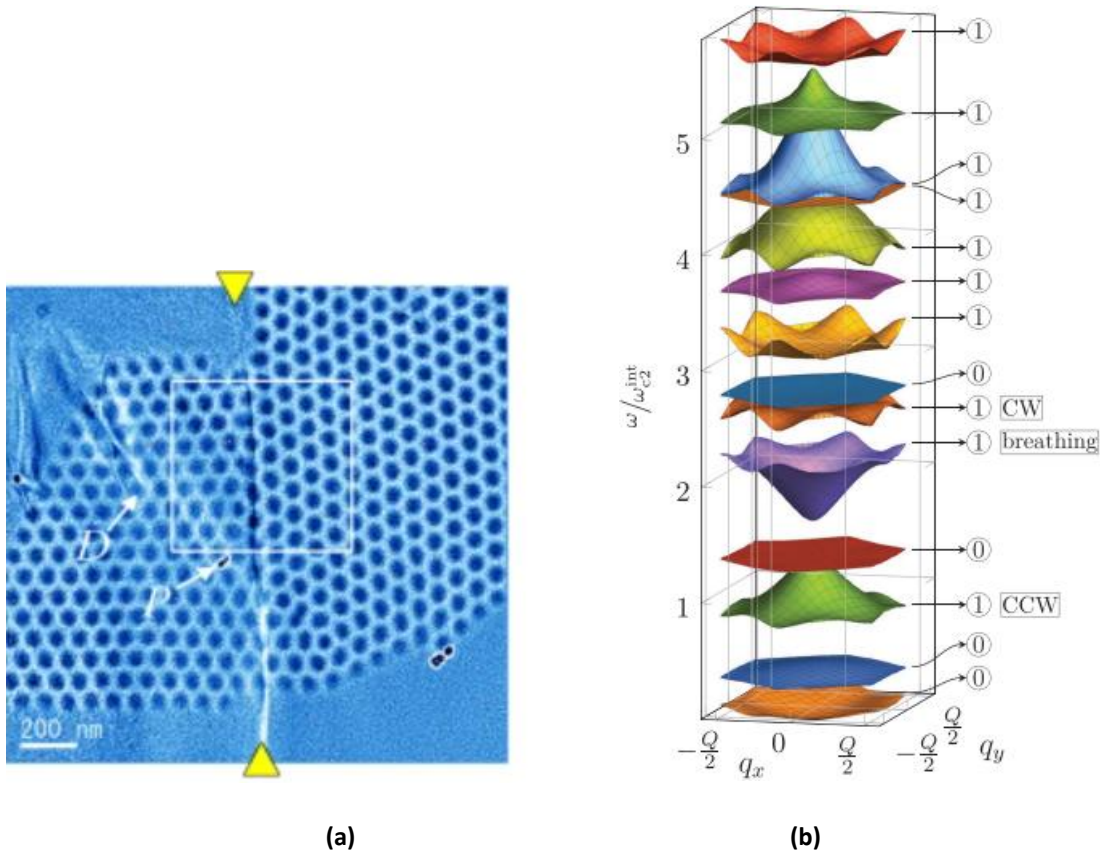
Fig. 4.17: (a) STEM image of skyrmion lattice in a thin film of $FeGe_{1-x}Si_x$ with a grain boundary indicated by yellow arrows; image reproduced from Ref. [89]; (b) full magnon spectrum in MnSi by calculation; image reproduced from Ref. [6].

In practical applications, it is crucial to understand how structure and magnetic defects affect the stability and dynamics of skyrmion lattice, while these questions remain to be elucidated. One commonly observed example is the grain boundary, where skyrmion lattice has a small-angle rotation on one side of the boundary

with respect to the other side, as shown in Fig. 4.17 (a) which is obtained by scanning transmission electron microscope (STEM). With the microwave-based pump-probe technique developed in this thesis, one can in real space directly observe how grain boundary affects the resonant frequency and amplitude of collective modes in skyrmion lattice. By varying the output frequency of the synthesizer, we are even allowed to investigate higher-energy collective modes that were proposed by calculation [6], but not yet detected by previous microwave absorption spectroscopy or optical experiments. The full magnon spectrum of skyrmion lattice in MnSi by calculation is shown in Fig. 4.17 (b). Further, it is interesting to study spin wave dynamics and propagation in linear spin-wave regime and non-linear spin wave regime by slowly ramping up the RF power. Therefore, the eventual realization of this novel technique has significant impact towards the design of spin-wave spintronic devices employing controllable GHz skyrmion lattice dynamics.

4.5 Summary, limitations and outlook

In summary, within the time frame of this thesis, we have achieved a coherent RF pumping system operating at GHz frequency range and room temperature, and integrated it into an ultrafast TEM. A unique design that makes use of a PCB and a CPW fabricated on a microchip was proposed. Compared with similar RF holders manufactured previously, the novelty of the development in this thesis is that it allows for studying the dynamics triggered by a magnetic field instead of an electric current. In contrast, previous RF holders [90, 91] were mainly employed to study current-driven dynamics where the electric current flows through the sample by two electrodes. The design chosen in this thesis is in line with the long-term scientific goals of this project, namely, directly investigating the collective magnon dynamics of skyrmion lattice and their relevant spin wave propagation properties in real space. To meet these goals, we also implemented a phase-locking loop that realizes a novel "clocked" pump-probe technique and further considered candidate skyrmion lattice hosting materials suitable for these experiments.

Despite significant progress made by this thesis work towards the eventual goals, technical challenges remain unresolved. Firstly, further work is required to determine the optimal imaging condition with ps electron pulses. In the meantime, LTEM imaging with around 100 fs electron pulses on the magnetic vortex in a Fe_3O_4 magnetite lamella was achieved, and one image is provided in Fig. 4.18 (b). Compared with images obtained by thermal electrons [Fig. 4.18 (a)], the magnetic contrast is still clearly visible in photoelectron mode. However, ps imaging is a new regime where the electron coherence, space charge effect [92], and electron number per pulse drastically vary. Further optimization of microscope settings involves using new cathodes with larger, flat surfaces and adjusting the Wehnelt gap and bias. The realization of ps temporal resolution imaging is another impactful benchmark for using TEM to study GHz dynamics.
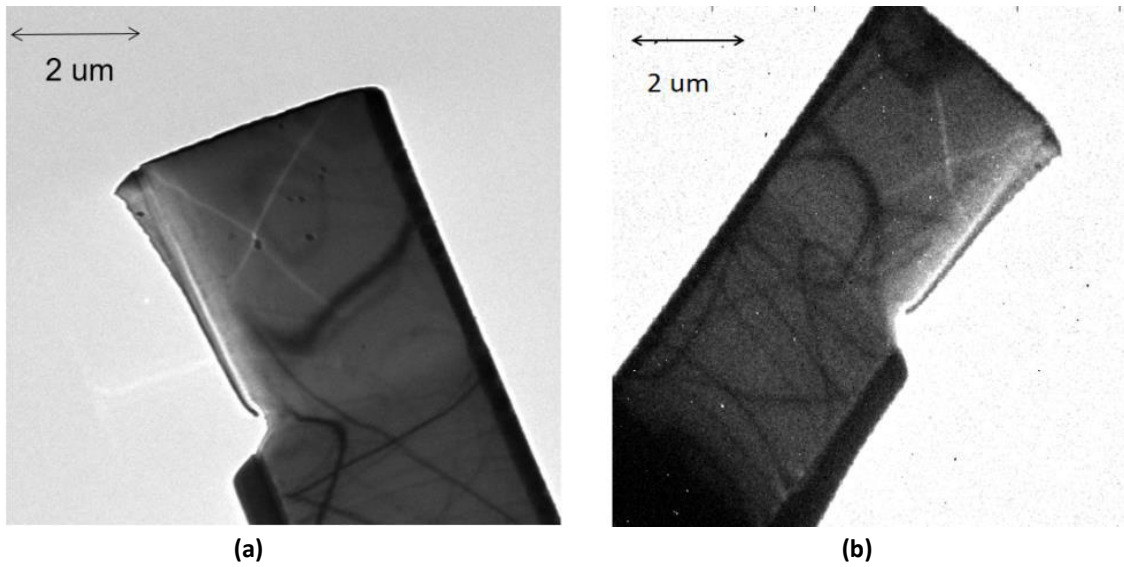
Fig. 4.18: LTEM images of a magnetite lamella using (a) continuous thermal electrons and (b) photoelectron pulses. The acquisition time is 10 seconds and 8 minutes, respectively. Magnetic contrast is formed by a magnetic vortex.

Secondly, the transfer of the $Co_8Zn_{10}Mn_2$ lamella to the CPW microchip in a FIB instrument is challenging because it is not a standard procedure. Before transferring, we propose to stress relieve the SiRN membrane by cutting rectangular holes near one of the transmission lines where the lamella is placed. These holes are also needed to reduce background intensity in TEM images, improving the image quality obtained by ps electron pulses. Last but not least, a strategy to determine the exact phase shift between ps electron pulses and RF pumping signal is highly desired, similar to the laser-based pump-probe technique where photon-induced near-field electron microscopy (PINEM) effect [93] is commonly adopted to determine time-zero when the dynamics begins. Though in principle, the dynamics coherently driven by a sinusoidal microwave can be constructed by starting at a random phase and scanning the phase shift by one cycle, considering practical difficulties, it would still help to track the dynamics at the early stages of this technical development.

It is also worth pointing out the limitations of the CPW design adopted in this thesis work. TEM investigations of the microchip revealed that while AC magnetic field was indeed produced, the electron beam experienced a severe charging effect, that is, electrons accumulate in the insulating substrate of the microchip and then push away the incoming electrons. Further, the strong electric field component from the CPW interacted strongly with the electron beam, masking the effects of smaller magnetic fields and thus creating conditions that are not ideal for probing dynamics of skyrmion lattice purely driven by AC magnetic field. For suppressing charging effects, one method is to metalize the rest of the microchip on both front and back surfaces by gold evaporation during photolithography procedures. The issue caused by the strong electric field component can be improved by making the SiRN window on the substrate off-center [close to the right end in Fig. 4.9 (a)], so that the electric field amplitude decays in the CPW due to voltage drop before reaching the membrane. To further optimize the performance of this system so that it can eventually be capable of resolving the breathing mode dynamics in $Co_8Zn_{10}Mn_2$, a global simulation taking into account microwave propagation, electron beam, heating effect and field distributions etc. is needed.

Chapter Five: Conclusion and perspectives

In conclusion, through this thesis work we have demonstrated the feasibility of using the novel quantum chemistry calculation to quantitatively characterize magnetic interactions in complex magnetic materials; we also demonstrate the feasibility of adopting a CPW microchip to implement a coherent pumping system in an ultrafast TEM and perform clocked pump-probe experiment. These are achieved by inelastic neutron scattering experiments in reciprocal space, and real space imaging by time-resolved TEM in real space, respectively. The novelty and practical impact of reciprocal studies is that quantum chemistry calculation may eventually become a tool for the community to predict new skyrmion hosting systems, especially Néel-type skyrmion lattice and open new possibilities to tailor skyrmion-based spintronic devices; while for the technical development in real space, it may bring a novel pump-probe technique based on microwave to study coherent spin wave dynamical properties of skyrmions. Despite the progress achieved in this thesis, there still remains several challenges, both theoretical and practical, to be addressed in future work so that these novelties can be reliably applied in research and industry.

First of all, more dedicated work is required to describe the microscopic properties of V^{4+} ions in $VOSe_2O_5$. The magnon spectrum of $VOSe_2O_5$ exhibits unique features that are not found in the other Néel-type skyrmion lattice hosting bulk material GaV_4S_8, as well as the typical Bloch-type skyrmion lattice hosting system Cu_2OSeO_3. The spectrum of GaV_4S_8 measured at SEQUOIA beamline, Oak Ridge National Laboratory, USA, together with SpinW simulation [94], shows that there is no energy gap in the lowest band, as displayed in Fig. 5.1. This experiment was performed at base temperature 1.7 K with a ferromagnetic ground state. Also, its lowest band is much more dispersive than that of $VOSe_2O_5$ measured in this thesis, and the energy range can reach up to 6 meV. Here, an effective molecular V_4 cluster model is employed to simulate the dispersion due to the hybridization of V 3d bands. While we have identified that the exchange anisotropy is the origin of the energy gap in the magnon spectrum of $VOSe_2O_5$, a microscopic picture that explains the presence of exchange anisotropy in this system is still lacking.

We propose that spin-orbit coupling of the Se_2O_5 groups in the a-b plane connecting three vanadium chains is most likely to be responsible for the generation of exchange anisotropy in $VOSe_2O_5$. Here, Se is the heaviest atom in this compound, and its role has not been explicitly taken into account by quantum chemistry calculations. Further, the strong oxygen K-edge in XMCD signal revealed by elastic resonant x-ray scattering [Fig. 3.5 (b)] indicates strong hybridization effect is also present in $VOSe_2O_5$. The spin distribution over V_4 molecular clusters in GaV_4S_8 is proven to be uniform [94], hence isotropic exchange interaction is expected. The hypothetically present spin-orbit interaction in $VOSe_2O_5$ can cause non-uniform spin distribution. To support this argument, an ab-initio calculation of electronic properties and spin-orbit couplings in this system is desired in the future.
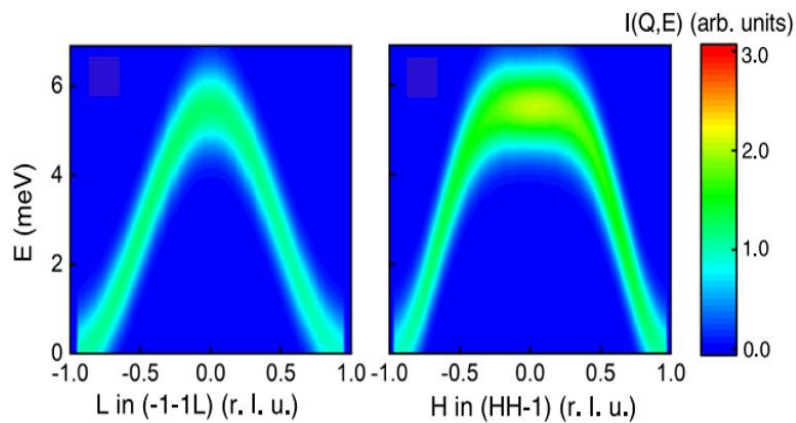
Fig. 5.1: SpinW simulation of the magnon dispersion along (-1 -1 L) and (H H -1) directions in GaV_4S_8 at base temperature 1.7 K; image reproduced from Ref. [94].

Understanding the interplay of spin, charge and orbital degrees of freedom in $VOSe_2O_5$ at a microscopic level is another important benchmark towards understanding its complicated magnetic phase diagram and the stabilization mechanism of Néel-type skyrmion lattice. At this level, we can even give answers to various mysteries in this system. For example, recently, an inelastic neutron scattering experiment performed at CAMEA beamline, PSI with an external magnetic field applied along the a-axis revealed double amount of Zeeman shift compared with that expected from a spin ½ system (data not shown). It is likely that the hybridization effect groups V^{4+} ions with spin ½ into clusters with an effective spin 1, though the details of hybridization in $VOSe_2O_5$ remains to be elucidated.

Moreover, the role of DMI in the magnon spectrum of Néel-type skyrmion lattice remains to be explored. This thesis work did not indicate effect from DMI on the $VOSe_2O_5$ spectrum, neither did Ref. [95] indicate any DMI effect on the GaV_4S_8 spectrum. This is possibly due to the fact that at base temperature, the magnetic phases for $VOSe_2O_5$ and GaV_4S_8 are ferrimagnetic and ferromagnetic states, respectively, which are both commensurate. In contrast, for Bloch-type skyrmion lattice, at base temperature the magnetic phase is an incommensurate helical state. In the magnon spectrum of Cu_2OSeO_3 measured by ToF neutron spectroscopy shown in Fig. 5.2, DMI has been proved to induce a tiny gap of 12 µeV at the lowest band; at higher energy band near 30 meV, DMI is argued to be associated with the band splitting [95]. To investigate the role of DMI in $VOSe_2O_5$ in the future, we propose to measure its magnon spectrum at the IC-1 phase (near 6 K) where the magnetic phase is an incommensurate cycloidal state. Since DMI is critical in the formation of skyrmion lattice, studying the role of DMI is crucial towards the eventual goal of understanding the stabilization mechanism of Néel-type skyrmion lattice.
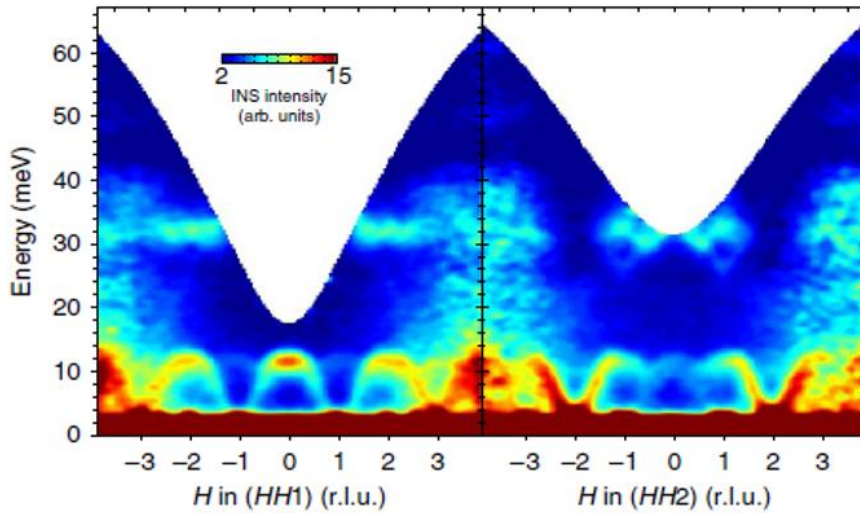
Fig. 5.2: Magnon dispersion along (H H 1) and (H H 2) directions in Cu_2OSeO_3 at 4.5 K; image reproduced from Ref. [95].

As a final remark, this thesis work supports that quantum chemistry calculation is reasonably reliable in computing exchange interactions at base temperature, whereas there is still no direct evidence to support the accuracy of the predicted DMI (labelled as DM_3 in Table 1). Since it is non-trivial to directly link the spin Hamiltonian obtained at base temperature to the spin Hamiltonian in the more complex cycloidal phase or skyrmion lattice phase, from a theoretical perspective, the next step is to compute exchange interactions and DMI at the IC-1 phase. By comparing with the values obtained from inelastic neutron scattering experiments also performed at the IC-1 phase, we hope to better examine the validity of quantum chemistry calculation in computing both exchange interaction and DMI for incommensurate magnetic phase. This way, the spin Hamiltonian is more relevant to the skyrmion lattice phase, and the calculation will eventually become a routine recipe for the community to search new skyrmion lattice hosting systems.

Appendix One: SpinW script for plotting and fitting the magnon dispersion in VOSe$_2$O$_5$

```
% create lattice
clear chains;
chains = spinw;
chains.genlattice('lat_const', [11.22 11.22 7.86], 'angled', [90 90 90], 'sym',103)
chains.addatom('r',[0.00000 0.00000 0.122323],'S',0.5,'label',{'MV4'},'color',{'blue'});
chains.addatom('r',[0.00000 0.50000 0.058713987],'S',0.5,'label',{'MV4'},'color',{'blue'});
chains.addatom('r',[0.50000 0.50000 0.3683237],'S',0.5,'label',{'MV4'},'color',{'blue'});
chains.addmatrix('label','g_1','value',diag([1.955 1.955 2]));
chains.gencoupling;
chains.addg('g_1');
chains.plot('ionMode','g');

% set external magnetic field, magnitude and direction
B = 10; % [T]
n = [0 0 1];
chains.field(n/norm(n)*B);

% create bonds
chains.gencoupling('maxDistance',8)
chains.table('bond',[])
display('Rows: dlx, dly, dlz, at1, at2, idx, ma1, ma2, ma3')
nBond = size(chains.couplingtable([1 2]).table,2);
fprintf(['' repmat('%4d ',1,nBond) '\n'],chains.couplingtable([1 2]).table');
display('Bond vectors (first three rows) and bond distances')
chains.couplingtable([1 2]).bondv
chains.table('matom')
plot(chains,'range',[1 1 1])
chains.table('bond',[])

% magnetic interaction parameters with exchange anisotropy
J1a = -0.01;
J1b = -0.07;
J1c = -0.18;
J2 = -0.22;
J3 = diag([2.18 2.18 2.7]);

% generate coupling
chains.gencoupling('maxDistance',8);
chains.table('bond',[]);
chains.addmatrix('label','J1a','value',J1a,'color','green');
chains.addmatrix('label','J1b','value',J1b,'color','yellow');
chains.addmatrix('label','J1c','value',J1c,'color','orange');
chains.addmatrix('label','J2','value',J2,'color','red');
chains.addmatrix('label','J3','value',J3,'color','cyan');

chains.addcoupling('mat','J1a','bond',1);
chains.addcoupling('mat','J1b','bond',2);
chains.addcoupling('mat','J1c','bond',3);
chains.addcoupling('mat','J2','bond',4);
chains.addcoupling('mat','J3','bond',5);

% insert magnetic ground state obtained from neutron diffraction experiment
chains.table('mat')
plot(chains, 'range',  [1 1 1])
optStruct = true;
qab = 0;
```

```matlab
chains.genmagstr('mode','direct', 'k',[0 0 0],'n',[0 0 1],'S',[0 0 0 0 0 0 0 0; 0 0 0 0 0 0 0 0; 1 1 1 1 1 1 -1 -1], 'nExt', [1 1 1]);
magRes = chains.optmagsteep('nRun', 1e4);
opt_moments = optmagsteep(chains, 'nRun', 1000, 'nExt', [1 1 1]);

% Fit experimental spin wave dispersion
perf = swpref;
pref.tid = 0;
par_fit        = struct;
par_fit.datapath = 'VOSe2O5_fitted_modes_ALL3.txt';
par_fit.Evect   = linspace(0,10,147);
par_fit.func    = @(obj,p)matparser(obj,'param',p,...
                    'mat',{'J1a' 'J1b' 'J1c' 'J2' 'J3 (1,1)' 'J3 (2,2)' 'J3 (3,3)'}'},'init',true);
par_fit.xmin    = [-0.4  -0.4  -1     -1    1  1  1];
par_fit.xmax    = [0      0    -0.1  -0.1  4  4  4 ];
par_fit.x0      = [ -8 ];
par_fit.plot    = true;
par_fit.hermit  = false;
par_fit.optimizer = 'pso';
par_fit.maxiter = 100;
par_fit.optmem  = 1;
par_fit.nrun    = 10;
fitStr = chains.fitspec(par_fit);
```

Appendix Two: Fitted spin wave modes from inelastic neutron scattering experiments

In this section, we provide a list of all magnon modes measured at TASP, IN12 and CAMEA beamlines for the plot in Fig 3.21. The fitted energy or *q* by Gaussian functions at each scan or cut, the error bar which is the width of the Gaussian function, are included.

q	Energy (meV)	beamline	method	band
(1.25 0 0)	0.375 ± 0.146	IN12	Energy scan	Lowest band
(1.375 0 0)	0.588 ± 0.038	IN12	Energy scan	Lowest band
(1.5 0 0)	0.615 ± 0.029	IN12	Energy scan	Lowest band
(1.625 0 0)	0.585 ± 0.035	IN12	Energy scan	Lowest band
(1.75 0 0)	0.481 ± 0.058	IN12	Energy scan	Lowest band
(1.875 0 0)	0.478 ± 0.058	IN12	Energy scan	Lowest band
(2.125 0 0)	0.520 ± 0.110	IN12	Energy scan	Lowest band
(2.25 0 0)	0.467 ± 0.060	IN12	Energy scan	Lowest band
(2.375 0 0)	0.576 ± 0.047	IN12	Energy scan	Lowest band
(2.5 0 0)	0.615 ± 0.032	IN12	Energy scan	Lowest band
(2.625 0 0)	0.585 ± 0.033	IN12	Energy scan	Lowest band
(2.75 0 0)	0.475 ± 0.065	IN12	Energy scan	Lowest band
(2.033 ± 0.130 0 0)	1.4	CAMEA	Constant energy cut	Second band
(2.205 ± 0.096 0 0)	1.6	CAMEA	Constant energy cut	Second band
(1.868 ± 0.098 0 0)	1.6	CAMEA	Constant energy cut	Second band
(2.285 ± 0.099 0 0)	1.8	CAMEA	Constant energy cut	Second band
(1.756 ± 0.089 0 0)	1.8	CAMEA	Constant energy cut	Second band
(2.328 ± 0.110 0 0)	2.0	CAMEA	Constant energy cut	Second band
(1.700 ± 0.108 0 0)	2.0	CAMEA	Constant energy cut	Second band
(2.361 ± 0.114 0 0)	2.2	CAMEA	Constant energy cut	Second band
(1.579 ± 0.114 0 0)	2.2	CAMEA	Constant energy cut	Second band
(1 0 0)	2.837 ± 0.231	TASP	Energy scan	Third band
(1.125 0 0)	2.927 ± 0.248	TASP	Energy scan	Third band
(1.25 0 0)	2.873 ± 0.149	TASP	Energy scan	Third band
(1.375 0 0)	2.831 ± 0.102	TASP	Energy scan	Third band
(1.066 ± 0.131 0 0)	4.1	CAMEA	Constant energy cut	Highest band
(0.893 ± 0.067 0 0)	4.3	CAMEA	Constant energy cut	Highest band

q	Energy (meV)	beamline	method	band
(1.155 ± 0.127 0 0)	4.3	CAMEA	Constant energy cut	Highest band
(0.868 ± 0.089 0 0)	4.5	CAMEA	Constant energy cut	Highest band
(1.224 ± 0.101 0 0)	4.5	CAMEA	Constant energy cut	Highest band
(0.793 ± 0.080 0 0)	4.7	CAMEA	Constant energy cut	Highest band
(1.227 ± 0.102 0 0)	4.7	CAMEA	Constant energy cut	Highest band

Table 3: List of all fitted magnon modes along the (H 0 0) direction for VOSe$_2$O$_5$ measured by inelastic neutron scattering experiments.

q	Energy (meV)	beamline	method	band
(1 0 1)	0.527 ± 0.012	CAMEA	Constant q cut	Lowest band
(1.25 0 1)	0.523 ± 0.021	CAMEA	Constant q cut	Lowest band
(1.5 0 1)	0.523 ± 0.024	CAMEA	Constant q cut	Lowest band
(1.75 0 1)	0.513 ± 0.020	CAMEA	Constant q cut	Lowest band
(2 0 1)	0.520 ± 0.021	CAMEA	Constant q cut	Lowest band
(2.25 0 1)	0.524 ± 0.026	CAMEA	Constant q cut	Lowest band
(2.5 0 1)	0.529 ± 0.028	CAMEA	Constant q cut	Lowest band
(2.75 0 1)	0.530 ± 0.014	CAMEA	Constant q cut	Lowest band
(3 0 1)	0.532 ± 0.016	CAMEA	Constant q cut	Lowest band
(2.036 ± 0.110 0 1)	1.4	CAMEA	Constant energy cut	Second band
(2.160 ± 0.071 0 1)	1.6	CAMEA	Constant energy cut	Second band
(1.947 ± 0.073 0 1)	1.6	CAMEA	Constant energy cut	Second band
(2.202 ± 0.075 0 1)	1.8	CAMEA	Constant energy cut	Second band
(1.795 ± 0.083 0 1)	1.8	CAMEA	Constant energy cut	Second band
(2.349 ± 0.122 0 1)	2.0	CAMEA	Constant energy cut	Second band
(1.711 ± 0.077 0 1)	2.0	CAMEA	Constant energy cut	Second band
(2.416 ± 0.086 0 1)	2.2	CAMEA	Constant energy cut	Second band
(1.675 ± 0.090 0 1)	2.2	CAMEA	Constant energy cut	Second band
(1 0 1)	3.133 ± 0.065	IN12	Energy scan	Third band
(1.25 0 1)	3.147 ± 0.066	IN12	Energy scan	Third band
(1.5 0 1)	3.163 ± 0.065	IN12	Energy scan	Third band
(2.5 0 1)	3.172 ± 0.046	IN12	Energy scan	Third band
(2.75 0 1)	3.145 ± 0.075	IN12	Energy scan	Third band
(1.031 ± 0.075 0 1)	4.1	CAMEA	Constant energy cut	Highest band

(0.923 ± 0.051 0 1)	4.3	CAMEA	Constant energy cut	Highest band
(1.102 ± 0.091 0 1)	4.3	CAMEA	Constant energy cut	Highest band
(0.872 ± 0.064 0 1)	4.5	CAMEA	Constant energy cut	Highest band
(1.188 ± 0.086 0 1)	4.5	CAMEA	Constant energy cut	Highest band
(0.797 ± 0.072 0 1)	4.7	CAMEA	Constant energy cut	Highest band
(1.216 ± 0.060 0 1)	4.7	CAMEA	Constant energy cut	Highest band
(0.740 ± 0.060 0 1)	4.9	CAMEA	Constant energy cut	Highest band
(1.282 ± 0.079 0 1)	4.9	CAMEA	Constant energy cut	Highest band

Table 4: List of all fitted magnon modes along the (H 0 1) direction for $VOSe_2O_5$ measured by inelastic neutron scattering experiments.

q = (H H 1.5)	Energy (meV)	beamline	method	band
H = 0.988 ± 0.101	1.6	CAMEA	Constant energy cut	Second band
H = 0.884 ± 0.069	1.8	CAMEA	Constant energy cut	Second band
H = 1.097 ± 0.063	1.8	CAMEA	Constant energy cut	Second band
H = 0.806 ± 0.073	2.0	CAMEA	Constant energy cut	Second band
H = 1.173 ± 0.068	2.0	CAMEA	Constant energy cut	Second band
H = 0.758 ± 0.052	2.2	CAMEA	Constant energy cut	Second band
H = 1.217 ± 0.041	2.2	CAMEA	Constant energy cut	Second band
H = 0.694 ± 0.065	2.4	CAMEA	Constant energy cut	Second band
H = 1.284 ± 0.058	2.4	CAMEA	Constant energy cut	Second band
H = 0.636 ± 0.068	2.6	CAMEA	Constant energy cut	Second band
H = 1.320 ± 0.027	2.6	CAMEA	Constant energy cut	Second band
H = 0.538 ± 0.118	2.8	CAMEA	Constant energy cut	Second band
H = 1.373 ± 0.064	2.8	CAMEA	Constant energy cut	Second band
H = 0.502 ± 0.100	3.0	CAMEA	Constant energy cut	Second band
H = 1.480 ± 0.093	3.0	CAMEA	Constant energy cut	Second band
H = 0.982 ± 0.105	4.1	CAMEA	Constant energy cut	Highest band
H = 0.893 ± 0.099	4.3	CAMEA	Constant energy cut	Highest band
H = 1.082 ± 0.058	4.3	CAMEA	Constant energy cut	Highest band
H = 0.856 ± 0.083	4.5	CAMEA	Constant energy cut	Highest band
H = 1.104 ± 0.058	4.5	CAMEA	Constant energy cut	Highest band
H = 0.836 ± 0.080	4.7	CAMEA	Constant energy cut	Highest band

H = 1.139 ± 0.051	4.7	CAMEA	Constant energy cut	Highest band
H = 0.804 ± 0.065	4.9	CAMEA	Constant energy cut	Highest band
H = 1.165 ± 0.069	4.9	CAMEA	Constant energy cut	Highest band
H = 0.751 ± 0.066	5.1	CAMEA	Constant energy cut	Highest band
H = 1.225 ± 0.053	5.1	CAMEA	Constant energy cut	Highest band
H = 0.706 ± 0.088	5.3	CAMEA	Constant energy cut	Highest band
H = 1.259 ± 0.053	5.3	CAMEA	Constant energy cut	Highest band
H = 1.355 ± 0.140	5.5	CAMEA	Constant energy cut	Highest band
H = 0.524 ± 0.228	5.7	CAMEA	Constant energy cut	Highest band
H = 1.392 ± 0.137	5.7	CAMEA	Constant energy cut	Highest band
H = 0.503 ± 0.158	5.9	CAMEA	Constant energy cut	Highest band
H = 1.435 ± 0.158	5.9	CAMEA	Constant energy cut	Highest band

Table 5: List of all fitted magnon modes along the (H H 1.5) direction for $VOSe_2O_5$ measured by inelastic neutron scattering experiments.

q	Energy (meV)	beamline	method	band
(1 0 0)	0.531 ± 0.012	CAMEA	Constant **q** cut	Lowest band
(1 0 0.25)	0.529 ± 0.023	CAMEA	Constant **q** cut	Lowest band
(1 0 0.5)	0.526 ± 0.021	CAMEA	Constant **q** cut	Lowest band
(1 0 0.75)	0.527 ± 0.018	CAMEA	Constant **q** cut	Lowest band
(1 0 1)	0.520 ± 0.018	CAMEA	Constant **q** cut	Lowest band
(1 0 1.25)	0.516 ± 0.018	CAMEA	Constant **q** cut	Lowest band
(1 0 1.5)	0.525 ± 0.018	CAMEA	Constant **q** cut	Lowest band
(1 0 1.75)	0.523 ± 0.019	CAMEA	Constant **q** cut	Lowest band
(1 0 2)	0.526 ± 0.019	CAMEA	Constant **q** cut	Lowest band
(1 0 1.25)	1.618 ± 0.070	IN12	Energy scan	Second band
(1 0 1.5)	1.513 ± 0.101	IN12	Energy scan	Second band
(1 0 1.75)	1.365 ± 0.104	IN12	Energy scan	Second band
(1 0 2)	1.313 ± 0.112	IN12	Energy scan	Second band
(1 0 2.25)	1.402 ± 0.084	IN12	Energy scan	Second band
(1 0 2.5)	1.490 ± 0.101	IN12	Energy scan	Second band
(1 0 2.75)	1.650 ± 0.122	IN12	Energy scan	Second band
(1 0 3)	1.692 ± 0.086	IN12	Energy scan	Second band

(1 0 0)	2.837 ± 0.231	TASP	Energy scan	Third band
(1 0 0.125)	2.907 ± 0.261	TASP	Energy scan	Third band
(1 0 0.25)	2.834 ± 0.099	TASP	Energy scan	Third band
(1 0 0.375)	2.892 ± 0.135	TASP	Energy scan	Third band
(1 0 0.5)	2.958 ± 0.109	TASP	Energy scan	Third band
(1 0 0.625)	2.998 ± 0.133	TASP	Energy scan	Third band
(1 0 0.75)	3.061 ± 0.158	TASP	Energy scan	Third band
(1 0 0.875)	3.103 ± 0.140	TASP	Energy scan	Third band
(1 0 1)	3.053 ± 0.145	TASP	Energy scan	Third band

Table 6: List of all fitted magnon modes along the (1 0 L) direction for $VOSe_2O_5$ measured by inelastic neutron scattering experiments.

q	Energy (meV)	beamline	method	band
(1.5 0 0)	0.615 ± 0.029	IN12	Energy scan	Lowest band
(1.5 0 0.25)	0.604 ± 0.030	IN12	Energy scan	Lowest band
(1.5 0 0.5)	0.594 ± 0.024	IN12	Energy scan	Lowest band
(1.5 0 0.75)	0.590 ± 0.035	IN12	Energy scan	Lowest band
(1.5 0 1)	0.581 ± 0.030	IN12	Energy scan	Lowest band
(1.5 0 1.25)	0.589 ± 0.030	IN12	Energy scan	Lowest band
(1.5 0 1.5)	0.603 ± 0.030	IN12	Energy scan	Lowest band
(1.5 0 1.75)	0.609 ± 0.040	IN12	Energy scan	Lowest band
(1.5 0 2)	0.623 ± 0.035	IN12	Energy scan	Lowest band
(1.5 0 2.5)	2.331 ± 0.019	CAMEA	Constant q cut	Second band
(1.5 0 2.25)	2.327 ± 0.019	CAMEA	Constant q cut	Second band
(1.5 0 2)	2.334 ± 0.018	CAMEA	Constant q cut	Second band
(1.5 0 1.75)	2.341 ± 0.017	CAMEA	Constant q cut	Second band
(1.5 0 1.5)	2.336 ± 0.025	CAMEA	Constant q cut	Second band
(1.5 0 1.25)	2.323 ± 0.029	CAMEA	Constant q cut	Second band
(1.5 0 1)	2.324 ± 0.014	CAMEA	Constant q cut	Second band
(1.5 0 2.5)	2.884 ± 0.049	CAMEA	Constant q cut	Third band
(1.5 0 2.25)	2.867 ± 0.050	CAMEA	Constant q cut	Third band
(1.5 0 2)	2.851 ± 0.062	CAMEA	Constant q cut	Third band
(1.5 0 1.75)	2.866 ± 0.053	CAMEA	Constant q cut	Third band

(1.5 0 1.5)	2.945 ± 0.112	CAMEA	Constant **q** cut	Third band
(1.5 0 1.25)	3.035 ± 0.103	CAMEA	Constant **q** cut	Third band
(1.5 0 1)	3.099 ± 0.051	CAMEA	Constant **q** cut	Third band

Table 7: List of all fitted magnon modes along the (1.5 0 L) direction for $VOSe_2O_5$ measured by inelastic neutron scattering experiments.

Bibliography

[1] T. H. R. Skyrme. A unified field theory of mesons and baryons. Science Direct, Nuclear Physics, Volume 31, Pages 556-569 (1962).

[2] N. R. Cooper. Skyrmions in Quantum Hall Systems with Realistic Force-Laws. Phys. Rev. B 55, R1934 (1997).

[3] Bobeck, A. H., & Scovil, H. E. D. MAGNETIC BUBBLES. Scientific American, 224(6), 78–91 (1971).

[4] A. Neubauer, C. Pfleiderer, B. Binz, A. Rosch, R. Ritz, P. G. Niklowitz, and P. Böni. Topological Hall Effect in the A Phase of MnSi. Phys. Rev. Lett. 102, 186602 (2009).

[5] Liang, D., DeGrave, J., Stolt, M. et al. Current-driven dynamics of skyrmions stabilized in MnSi nanowires revealed by topological Hall effect. Nat Commun 6, 8217 (2015).

[6] Markus Garst et al. Collective spin excitations of helices and magnetic skyrmions: review and perspectives of magnonics in non-centrosymmetric magnets. J. Phys. D: Appl. Phys. 50 293002 (2017).

[7] Lara, A., Robledo Moreno, J., Guslienko, K.Y. et al. Information processing in patterned magnetic nano-structures with edge spin waves. Sci Rep 7, 5597 (2017).

[8] Kézsmárki, I., Bordács, S., Milde, P. et al. Néel-type skyrmion lattice with confined orientation in the polar magnetic semiconductor GaV_4S_8. Nature Mater 14, 1116–1122 (2015).

[9] Pfleiderer, C. Surfaces get hairy. Nature Phys 7, 673–674 (2011).

[10] Alexey A. Kovalev and Shane Sandhoefner. Skyrmions and Antiskyrmions in Quasi-Two-Dimensional Magnets. Front. Phys. Volume 6, Article 98 (2018).

[11] Nayak AK, Kumar V, Ma T, Werner P, Pippel E, Sahoo R, et al. Magnetic antiskyrmions above room temperature in tetragonal Heusler materials. Nature 548:561–6 (2017).

[12] Birch, M.T., et al. Real-space imaging of confined magnetic skyrmion tubes. Nature Communications., 11: 1726 (2020).

[13] Schulz, T., Ritz, R., Bauer, A. et al. Emergent electrodynamics of skyrmions in a chiral magnet. Nature Phys 8, 301–304 (2012).

[14] Jonietz, F. et al. Spin transfer torques in MnSi at ultralow current densities. Science 330, 1648–1651 (2010).

[15] Christian Pfleiderer and Achim Rosch. Condensed-matter physics: Single skyrmions spotted. Nature, 465 (7300): 880–881 (2010).

[16] Naoto Nagaosa and Yoshinori Tokura. Topological properties and dynamics of magnetic skyrmions. Nature Nanotechnology, 8(12):899–911 (2013).

[17] I. Dzyaloshinsky. A thermodynamic theory of "weak" ferromagnetism of antiferromagnetics. Journal of Physics and Chemistry of Solids. Volume 4, Issue 4, Pages 241-255 (1958).

[18] Tôru Moriya. Anisotropic Superexchange Interaction and Weak Ferromagnetism. Rev. 120, 91 (1960).

[19] Jadaun, P., Register, L.F. & Banerjee, S.K. The microscopic origin of DMI in magnetic bilayers and prediction of giant DMI in new bilayers. npj Comput Mater 6, 88 (2020).

[20] Tilley, Richard. Crystals and Crystal Structures. John Wiley (2006). pp. 80–83.

[21] Albert Fert, Vincent Cros, and João Sampaio. Skyrmions on the track. Nature Nanotechnology, 8(3):152–156 (2013).

[22] S. Seki, J.-H. Kim, D. S. Inosov, R. Georgii, B. Keimer, S. Ishiwata, and Y. Tokura. Formation and rotation of skyrmion crystal in the chiral-lattice insulator Cu_2OSeO_3. Phys. Rev. B 85, 220406(R) (2012).

[23] Sang-Hwan Kim, et al. Experimental and Computational Investigation of the Polar Ferrimagnet $VOSe_2O_5$. Chem. Mater. 22, 17, 5074–5083 (2010).

[24] Janson, O., Rousochatzakis, I., Tsirlin, A. et al. The quantum nature of skyrmions and half-skyrmions in Cu2OSeO3. Nat Commun 5, 5376 (2014).

[25] Oleksandr KRIUCHKOV. Theories of topologically-induced phenomena in skyrmion-hosting magneto-electric insulators. EPFL thesis no. 8163 (2017).

[26] Takashi Kurumaji, Taro Nakajima, Victor Ukleev, Artem Feoktystov, Taka-hisa Arima, Kazuhisa Kakurai, and Yoshinori Tokura. Néel-Type Skyrmion Lattice in the Tetragonal Polar Magnet $VOSe_2O_5$. Phys. Rev. Lett. 119, 237201 (2017).

[27] Takashi Kurumaji et al. Direct Observation of Cycloidal Spin Modulation and Field-induced Transition in Néel-type Skyrmion-hosting $VOSe_2O_5$. Journal of the Physical Society of Japan 90, 024705 (2021).

[28] Ogawa, N., Seki, S. & Tokura, Y. Ultrafast optical excitation of magnetic skyrmions. Sci Rep 5, 9552 (2015).

[29] S. Mühlbauer, B. Binz, F. Jonietz, C. Pfleiderer, A. Rosch, A. Neubauer, R. Georgii, and P. Böni. Skyrmion Lattice in a Chiral Magnet. Science, 323(5916): 915–919 (2009).

[30] Yu, X., Onose, Y., Kanazawa, N. et al. Real-space observation of a two-dimensional skyrmion crystal. Nature 465, 901–904 (2010).

[31] Tokunaga, Y., Yu, X., White, J. et al. A new class of chiral materials hosting magnetic skyrmions beyond room temperature. Nat Commun 6, 7638 (2015).

[32] Masahito Mochizuki. Spin-Wave Modes and Their Intense Excitation Effects in Skyrmion Crystals. Phys. Rev. Lett. 108, 017601 (2012).

[33] Y. Onose, et al. Observation of Magnetic Excitations of Skyrmion Crystal in a Helimagnetic Insulator Cu_2OSeO_3. Phys. Rev. Lett. 109, 037603 (2012).

[34] Y. Okamura, et al. Microwave magnetoelectric effect via skyrmion resonance modes in a helimagnetic multiferroic. Nature Communications 4, 2391 (2013).

[35] T. Schwarze, et al. Universal helimagnon and skyrmion excitations in metallic, semiconducting and insulating chiral magnets. Nature Materials 14, 478 - 483 (2015).

[36] A. V. Kimel, et al. Ultrafast non-thermal control of magnetization by instantaneous photomagnetic pulses. Nature 435, 655-657 (2005).

[37] F. Carbone, P. Tengdin, private commnunication of internal results at the Laboratory of Ultrafast Microscopy and Electron Scattering (LUMES), unpublished.

[38] Kim Lefmann. Neutron Scattering: Theory, Instrumentation, and Simulation. Lecture Notes (2021).

[39] F. Mezei. Novel approach to polarized neutron scattering. Physica B+C, Volumes 86–88, Part 3, Pages 1049-1052, ISSN 0378-4363 (1977).

[40] Michael Kotlarchyk, in Encyclopedia of Spectroscopy and Spectrometry (1999).

[41] Maria Monica Castellanos, Arnold McAuley, Joseph E. Curtis. Investigating Structure and Dynamics of Proteins in Amorphous Phases Using Neutron Scattering. Computational and Structural Biotechnology Journal, Volume 15, Pages 117-130, ISSN 2001-0370 (2017).

[42] Elbio Calzada et al. Construction and assembly of the neutron radiography and tomography facility ANTARES at FRM II. Nuclear Instruments and Methods in Physics Research Section A: Accelerators, Spectrometers, Detectors and Associated Equipment. 542: 38–44 (2005).

[43] Ian S. Anderson, Alan J. Hurd and Robert L. McGreevy. Neutron Scattering Applications and Techniques. Springer, ISSN1868-0380 (2015).

[44] The official website of SANS-I beamline, PSI. https://www.psi.ch/en/sinq/sansi/components

[45] Fullprof program official homepage. https://www.ill.eu/sites/fullprof/

[46] The official website of Zebra beamline, PSI. https://www.psi.ch/en/sinq/zebra/description

[47] The official website of TASP beamline, PSI. https://www.psi.ch/en/sinq/tasp/description

[48] The official website of CAMEA beamline, PSI. https://www.psi.ch/en/sinq/camea/description

[49] Ketty Beauvois and Milan Klicpera. Watching the ballet of atoms and magnetic moments. HERCULES School lecture notes, ILL (2021).

[50] Eimüller, T., Fischer, P., Köhler, M. et al. Transmission X-ray microscopy using X-ray magnetic circular dichroism. Appl Phys A 73, 697–701 (2001).

[51] M. Cheng and D. J. Keavney. Studies of nanomagnetism using synchrotron-based x-ray photoemission electron microscopy (X-PEEM). Rep. Prog. Phys. 75 026501 (2012).

[52] Jikang Fan, Yong Peng, Junqiang Xu, Haiying Xu, Dongqing Yang, Xiaopeng Li, Qi Zhou. Numerical simulation of beam current control mechanism in the thermionic electron gun. Vacuum, Volume 164, Pages 278-285, ISSN 0042-207X (2019).

[53] Ganesh KJ, Kawasaki M, Zhou JP, Ferreira PJ. D-stem: a parallel electron diffraction technique applied to nanomaterials. Microscopy and Microanalysis 16(5):614-21 (2010).

[54] Luis Alfredo Rodríguez González. In situ Lorentz microscopy and electron holography in magnetic nanostructures. Thesis, Université Toulouse III Paul Sabatier; Universidad de Zaragoza (2014).

[55] Official website of SpinW package. https://spinw.org/

[56] Hitoshi Yamazaki, Michinobu Mino. Chaos in Spin-Wave Instabilities: Theory and Experiments. Progress of Theoretical Physics Supplement, Volume 98, Pages 400–419 (1989).

[57] Official website of OOMMF package. https://nanohub.org/resources/oommf

[58] Official website of Mumax package. https://mumax.github.io/

[59] Chao Zuo, Jiaji Li, Jiasong Sun, Yao Fan, Jialin Zhang, Linpeng Lu, Runnan Zhang, Bowen Wang, Lei Huang, Qian Chen. Transport of intensity equation: a tutorial. Optics and Lasers in Engineering, Volume 135, 106187, ISSN 0143-8166 (2020).

[60] Yu, X., Kanazawa, N., Onose, Y. et al. Near room-temperature formation of a skyrmion crystal in thin-films of the helimagnet FeGe. Nature Mater 10, 106–109 (2011).

[61] Seki et al. Observation of Skyrmions in a Multiferroic Material. SCIENCE, Vol 336, Issue 6078 pp. 198-201 (2012).

[62] Y. Fujima, N. Abe, Y. Tokunaga, and T. Arima. Thermodynamically stable skyrmion lattice at low temperatures in a bulk crystal of lacunar spinel GaV_4Se_8. PHYSICAL REVIEW B 95, 180410(R) (2017).

[63] M. Wu, J. C. Zheng, and H. Q. Wang. Investigation of the vanadium L_{23} edge x-ray absorption spectrum of $SrVO_3$ using configuration interaction calculations: Multiplet, valence, and crystal-field effects. Phys. Rev. B 97, 245138 (2018).

[64] Yejin Kim et al. Phase identification of vanadium oxide thin films prepared by atomic layer deposition using X-ray absorption spectroscopy. RSC Adv., 10, 26588 (2020).

[65] Kruchkov, A. J., White, J. S., Bartkowiak, M. et al. Direct electric field control of the skyrmion phase in a magnetoelectric insulator. Sci Rep 8, 10466 (2018).

[66] Tobias Weber et al. Takin: An Open-Source Software for Experiment Planning, Visualisation, and Data Analysis. arXiv (2021) https://arxiv.org/pdf/1903.02632.pdf

[67] M. Klintenberg, S. E. Derenzo, M. J. Weber. Accurate crystal fields for embedded cluster calculations. Computer Physics Communications, Volume 131, Issues 1–2, Pages 120-128, ISSN 0010-4655 (2000).

[68] T. Helgaker, P. Jørgensen, and J. Olsen. Molecular Electronic-Structure Theory, Wiley, Chichester (2000).

[69] I. de P. R. Moreira and F. Illas. A unified view of the theoretical description of magnetic coupling in molecular chemistry and solid state physics. Physical Chemistry Chemical Physics 8, 1645 (2006).

[70] J. P. Malrieu, R. Caballol, C. J. Calzado, C. de Graaf, and N. Guihéry. Magnetic Interactions in Molecules and Highly Correlated Materials: Physical Content, Analytical Derivation, and Rigorous Extraction of Magnetic Hamiltonians. Chemical Reviews 114, 429 (2014).

[71] N. A. Bogdanov, J. van den Brink, and L. Hozoi. Ab initio computation of d-d excitation energies in low-dimensional Ti and V oxychlorides. Physical Review B 84, 235146 (2011).

[72] V. M. Katukuri, H. Stoll, J. van den Brink, and L. Hozoi. Ab initio determination of excitation energies and magnetic couplings in correlated quasi-two-dimensional iridates. Physical Review B 85, 220402 (2012).

[73] I. d. P. R. Moreira, F. Illas, C. J. Calzado, J. F. Sanz, J.-P. Malrieu, N. B. Amor, and D. Maynau. Local character of magnetic coupling in ionic solids. Physical Review B 59, R6593 (1999).

[74] N. A. Bogdanov, R. Maurice, I. Rousochatzakis, J. van den Brink, and L. Hozoi. Magnetic State of Pyrochlore $Cd_2Os_2O_7$ Emerging from Strong Competition of Ligand Distortions and Longer-Range Crystalline Anisotropy. Physical Review Letters 110, 127206 (2013).

[75] T. A. W. Beale et al., Antiferromagnetically Spin Polarized Oxygen Observed in Magnetoelectric TbMn2O5. Phys. Rev. Lett. 105, 087203 (2010).

[76] Jean Alexandre, John Ellis, Peter Millington, and Dries Seynaeve. Spontaneous symmetry breaking and the Goldstone theorem in non-Hermitian field theories. Phys. Rev. D 98, 045001 (2018).

[77] G. S. Tucker et al. Spin excitations in the skyrmion host Cu_2OSeO_3. PHYSICAL REVIEW B 93, 054401 (2016).

[78] Marc De Graef. Introduction to Conventional Transmission Electron Microscopy. Springer, Cambridge University Press (2009).

[79] H. Dömer and O. Bostanjoglo. High-speed transmission electron microscope. Review of Scientific Instruments 74, 4369 (2003).

[80] Vladimir A. Lobastov, Ramesh Srinivasan, and Ahmed H. Zewail. Four-dimensional ultrafast electron microscopy. PNAS 102 (20) 7069-7073 (2005).

[81] Armin Feist et al. Ultrafast transmission electron microscopy using a laser-driven field emitter: Femtosecond resolution with a high coherence electron beam. Ultramicroscopy Volume 176, Pages 63-73 (2017).

[82] Wang, P., Liang, J. & Wang, L. Single-shot ultrafast imaging attaining 70 trillion frames per second. Nat Commun 11, 2091 (2020).

[83] Priebe, K. E., Rathje, C., Yalunin, S. V. et al. Attosecond electron pulse trains and quantum state reconstruction in ultrafast transmission electron microscopy. Nature Photon 11, 793–797 (2017).

[84] P. Maine, D. Strickland, P. Bado, M. Pessot and G. Mourou, Generation of ultrahigh peak power pulses by chirped pulse amplification, IEEE Journal of Quantum Electronics, vol. 24, no. 2, pp. 398-403 (1988).

[85] Spencer A. Reisbick et al. Stroboscopic ultrafast imaging using RF strip-lines in a commercial transmission electron microscope. Ultramicroscopy 235, 113497 (2022).

[86] R. Simons. Coplanar Waveguide Circuits, Components, and Systems, Wiley, pp. 15-21 (2001).

[87] Scott B. Jones, Jon M. Wraith, Dani Or. Time domain reflectometry measurement principles and applications. Hydrological Processes Volume 16, Issue 1 p. 141-153 (2002).

[88] Ioannis Stasinopoulos. Low damping and linearly polarized GHz magnetization dynamics in the chiral magnet Cu2OSeO3 hosting spin helices and skyrmions. Thesis, Technische Universität München (2017).

[89] Matsumoto, T., So, YG., Kohno, Y. *et al.* Jointed magnetic skyrmion lattices at a small-angle grain boundary directly visualized by advanced electron microscopy. *Sci Rep* **6**, 35880 (2016).

[90] Pollard, S., Huang, L., Buchanan, K., Arena, D. & Zhu, Y. Direct dynamic imaging of non-adiabatic spin torque effects. Nat. Commun. 3, 1028 (2012).

[91] Möller, M., Gaida, J. H., Schäfer, S. et al. Few-nm tracking of current-driven magnetic vortex orbits using ultrafast Lorentz microscopy. Commun Phys 3, 36 (2020).

[92] Daniel Wilson et al. On space charge effects in laboratory-based photoemission electron microscopy using compact gas discharge extreme ultraviolet sources. New J. Phys. 22 103019 (2020).

[93] Sang Tae Park, Milo Lin and Ahmed H Zewail. Photon-induced near-field electron microscopy (PINEM): theoretical and experimental. New J. Phys. 12 123028 (2010).

[94] G. Pokharel et al., Spin dynamics in the skyrmion-host lacunar spinel GaV4S8. Physics Review B 104, 224425 (2021).

[95] Portnichenko, P., Romhányi, J., Onykiienko, Y. et al. Magnon spectrum of the helimagnetic insulator Cu2OSeO3. Nat Commun 7, 10725 (2016).

LE YU

Nationality: Chinese   Email: 396691370qq@gmail.com   Mobile: +41 (0)77493 3159

Address: Route Cantonale 35-304, St-Sulpice, 1025, Switzerland.

Education

Oct.2018 – Sep.2022   **Ph.D. Material Science and Engineering**

Paul Scherrer Institute - École Polytechnique Fédérale de Lausanne, Switzerland
- Developed ultrafast Lorentz transmission electron microscopy using microwave excitation and novel microwave based pump-probe technique;
- Applied cutting-edge neutron and x-ray scattering techniques to investigate skyrmion lattice and its hosting materials.

Mar.2018 – Sep.2018   **Exchange program**   **The University of Tokyo, Japan**
- Master thesis: Monte-Carlo simulations of non-collinear and non-coplanar magnetic orderings in itinerant magnets.

Sep.2016 – Mar.2018   **M.Sc. Physics**   **ETH Zurich, Switzerland**
- Core courses: solid state theory, introduction to magnetism, symmetries in physics, quantum field theory, quantum optics;
- Semester project: simulation of electronic transport in bilayer graphene quantum dot.

Sep.2012 – June.2016   **B.Sc. physics**   **The University of Sheffield, UK**
- Degree obtained: 1st class (second place within the year);
- Bachelor thesis: optical vortex beam carrying non-zero orbital angular momentum;
- Bachelor projects: single photon generation, photon statistics and photon coherence.

Internship and Summer/Winter School Experiences

Mar.2021 – Apr.2021: "*Neutrons & synchrotron radiation for science*". HERCULES European School, Institute Laue-Langevin, Grenoble, France.
- Five-week intensive training in the field of neutrons, x-ray synchrotron radiation, and free electron laser for condensed matter physics.
- Practicals, tutorials, and visits of large-scale facilities: ALBA in Barcelona, KIT in Karlsruhe, DESY and European XFEL in Hamburg, Elettra and FERMI in Trieste, ESRF and ILL in Grenoble, SOLEIL in Paris.

Jan.2019: "*Symmetry and topology: New twists in condensed matter*". MaNEP winter school, Saas-Fee, Switzerland.
- Broad introduction to contemporary frontier topics in condensed matter physics, focusing on superconductivity, quantum criticality, and various aspects of topology in condensed matter.

Sep.2017: "*Introducing photons, neutrons and muons for materials characterization*". Summer school held by Paul Scherrer Institute (PSI)
- Experienced large facilities such as synchrotron beam source, neutron spallation source and muon source, free electron laser;
- Performed neutron and X-Ray scattering experiments to study magnetic materials.

Aug.2014: "*Optics of two-dimensional materials beyond graphene*". Department of Physics, Low Dimensional Structures & Devices research group, the University of Sheffield. Funded by EPSRC Vacation Bursary.
- Worked with optical spectroscopy measurement using cryogenic equipment, lasers and sensitive light detectors; designed a control-measure program using LabVIEW.

Workshops and Conferences

- 2019, July. Gordon Research Conference. Poster presentation "Development of microwave-based pumping system in an ultrafast Lorentz transmission electron microscope".
- 2019, September. SPS (Swiss Physics society) conference. Poster presentation "Real space studies on the Skyrmion lattice and its dynamics in chiral magnets".
- 2020, December. HZB user annual conference, invited presenter. Presentation "Signature of anisotropic exchange interaction revealed by vector-field control of the helical order in a FeGe thin plate".
- 2021, August. SPS conference. Poster presentation "Inelastic neutron studies of the magnon spectrum in polar magnet VOSe2O5 and SpinW simulation".

Language and Programming Skills

- Chinese (native), English (fluent), Japanese (JLPT-N2), German (CEFR-B2), French (CEFR-A2)
- Familiar with C and C++, Python, LabVIEW, origin, Matlab.

Scholarships and Awards

- **Sep/2012 - Jun/2016:** The University of Sheffield SIC Progression Scholarship.
- **Sep/2013 - Jun/2016:** Faculty Undergraduate Scholarship for Academic Achievement.
- **Sep/2014 - Jun/2015:** Award for Most Effective Graphical Presentation of Information.
- **Sep/2013 - Jun/2014:** Fiddes Prize for Best Overall Academic Achievement in First Year.

Publications

- Ph.D. thesis: Real space and reciprocal space investigations of the spin dynamics in skyrmion-hosting materials (2022).
- Inelastic neutron scattering studies of the skyrmion hosting polar magnet $VOSe_2O_5$ – in preparation.
- Rina Takagi, et al. Square and rhombic lattices of magnetic skyrmions in a centrosymmetric binary compound. Nature Communications volume 13, Article number: 1472 (2022).
- Victor Ukleev, et al. Frustration-driven magnetic fluctuations as the origin of the low-temperature skyrmion phase in Co7Zn7Mn6. npj Quantum Mater. 6, 40 (2021).
- Victor Ukleev, et al. Signature of anisotropic exchange interaction revealed by vector-field control of the helical order in a FeGe thin plate. Phys. Rev. Research 3, 013094 (2021).